TÉCNICO
LISBOA

ERASMUS MUNDUS
FUSION

Universidad
Carlos III de Madrid

Università degli Studi di Padova

Centro Ricerche Fusione **(CRF)**

Universidade de Lisboa

Instituto Superior Tcnico **(IST)**

Universidad Carlos III de Madrid

JOINT RESEARCH DOCTORATE IN FUSION SCIENCE AND ENGINEERING
Cycle XXIX
and
ERASMUS MUNDUS International Doctoral College in Fusion Science and Engineering

Three Dimensional Physics in Reversed Field Pinch and Stellarator

Coordinator:	Prof. Paolo Bettini
Supervisor:	Dr. David Terranova
Co-Promoter:	Prof. Raul Sanchez
Co-Supervisor:	Dr. Daniel López-Bruna

Ph.D. student: Yangyang Zhang

Yangyang Zhang

Padova, February 2017

UNIVERSITÀ DEGLI STUDI DI PADOVA

LMU LUDWIG-MAXIMILIANS-UNIVERSITÄT MÜNCHEN

TÉCNICO LISBOA

JOINT Doctorate and NETWORK in Fusion Science and Engineering

Network Partners:

1. Instituto Superior Técnico (IST) Lisboa, Portugal;
2. Universitá degli studi di Padova, Italy;
3. Ludwig Maximilians University Munich, Germany.

In collaboration with:

1. Consorzio RFX, Italy;
2. IPP Garching, Germany.

Stay Hungry, Stay Foolish.

Abstract

This dissertation is dedicated to the study of three dimensional transport in toroidal magnetic configurations induced by the presence of the magnetic islands, which break the nested flux surfaces and make the magnetic field intrinsically three dimensional. The methodology applied is based on defining a certain symmetry so that the transport study could be performed in the approximation of 1.5 dimensions. The work has been carried out on both RFX-mod Reversed Field Pinch (RFP) and the TJ-II stellarator.

RFX-mod is the largest RFP in the world. The RFP configuration is sustained by the so-called dynamo mechanism, which is related to the non-linear interactions among many resonating MHD tearing modes. The transport study on RFX-mod has been performed on the three sub-states identified in the Quasi-Single Helicity regime, that features one single mode (dominant mode) dominating the mode spectrum, while the rest of the modes (secondary modes) remain at low amplitudes. In this regime proper flux coordinates can be identified considering an equilibrium built on the underlying axi-symmetric magnetic field plus the contribution from the dominant mode. In this way, a 1.5 dimensional approximation transport study is possible by averaging different physical quantities over the flux surfaces. The transport study is focused on the bean-shaped region where nearly conserved flux surfaces have been identified, on which the formation of steep thermal gradients is observed, interpreted as electron Internal Transport Barrier (eITB). Starting from experimental measurements, both the thermal gradients and the thermal diffusivity have been calculated and their behaviors have been discussed within the framework of stochastic transport. Finally, the energy confinement time has also been evaluated, adopting an improved method with respect to past studies, and the results show a significant improvement.

The transport study on TJ-II stellarator focuses on the calculation of the enhanced non-ambipolar radial electric field due to the presence of the magnetic islands. The main idea of the study is that the magnetic islands could modify the toroidal plasma viscosity, giving rise to an enhancement on the non-ambipolar particle fluxes. This work started with the study of the Neoclassical Toroidal Viscosity developed by K. C. Shaing for tokamak configurations, which ideally has a toroidal symmetry. Applying this theory, the particle flux can be expressed as a function of a monotonic radial coordinate and thus the transport study could be performed with a 1.5-dimensional approach. A moderate modification on the original theory has been made and the corresponding justification is presented, together with the detailed study in both tokamak and TJ-II configurations. The results show that an 'extra' local radial electric field is indeed induced by the magnetic islands in TJ-II plasmas, which could play

a positive role in the plasma confinement properties by affecting the L-H transition, which is believed to be strongly linked to the shear of $\boldsymbol{E} \times \boldsymbol{B}$ flow.

Sommario

Questo lavoro di tesi è dedicato allo studio degli effetti tridimensionali sul trasporto indotti dalla presenza di isole magnetiche in configurazioni toroidali per il confinamento magnetico. Le isole magnetiche producono la rottura delle superfici magnetiche annidate dando al campo magnetico caratteristiche intrinsecamente tridimensionali. La metodologia pplicata si base sulla possibilità di definire un certo livello di simmetria in maniera tale da poter studiare il trasporto nell'approssimazione di 1.5 dimensioni. Lo studio è stato fatto sul Reversed Field Pinch (RFP) RFX-mod e sullo stellarator TJ-II.
RFX-mod è il più grande RFP al mondo. La configurazione RFP è sostenuta dal meccanismo della dinamo, che è legato all'interazione non-lineare dei molti modi tearing risonanti. Lo studio del trasporto in RFX-mod è stato eseguito sui tre sotto-stati identificati nel regime a Quasi singola Elicità, il quale è caratterizzato da un singolo modo (modo dominante) che risulta dominante nello spettro dei modi, mentre gli altri modi (modi secondari) mantengono un' ampiezza ridotta. In questo regime, sono identificabile delle coordinate di flusso magnetico basate sulla combinazione dell'equilibrio assial-simmetrico sottostante con il contributo del modo dominante. In questa modo un approccio 1.5 dimensionale allo studio del trasporto è possibile considerando la media sulle superfici di flusso delle varie quantità fisiche. Lo studio del trasporto è riferito alla regione a forma di fagiolo dove è possibile identificare delle superfici di flusso quasi conservate dove si osserva la formazione di ripidi gradienti termici, interpretabili come barriere interne di trasporto elettronico (eITB). A partire dalle misure sperimentali, sono stati calcolati sia i gradienti termici che il coefficiente di diffusione termica e il loro andamento è stato discusso nell'ambito del trasporto stocastico. Alla fine è stato anche calcolato il tempo di confinamento dell'energia, utilizzando un metodo migliorato rispetto a quanto fatto in passato, dimostrando un significativo miglioramento delle prestazioni del plasma.
Lo studio del trasporto nello stellarator TJ-II si è concentrato nel calcolo dell'aumento del campo elettrico non-ambipolare dovuto alla presenza di isole magnetiche. L'idea alla base dello studio si basa sul fatto che un'isola magnetica potrebbe modificare la viscosità toroidale del plasma, aumentando in questo modo il flusso non-ambipolare delle particelle. Lo studio è partito dall' analisi del modello neoclassico di viscosità toroidale sviluppato da K. C. Shaing per la configurazione tokamak, che idealmente possiede una simmetria toroidale. Applicando questa teoria, il flusso di particelle può essere descritto in funzione di una coordinata radiale monotona e quindi lo studio del trasporto può essere affrontato nell'approssimazione 1.5 dimensionale. E' stato necessario considerare una parziale modifica della teoria originale la cui giustificazione

viene presentata assieme allo studio dettagliato sia nella configurazione tokamak che nello stellarator TJ-II. I risultati mostrano che un campo elettrico radiale 'aggiuntivo' è effettivamente indotto da un' isola magnetica nei plasmi di TJ-II. Questo potrebbe giocare un ruolo positivo nelle proprietà di confinamento del plasma, influenzando la transizione L-H, che si ritiene sia fortemente legata allo shear del moto $\boldsymbol{E} \times \boldsymbol{B}$.

Contents

Part I

Introduction

1 Toroidal Magnetic Confinement

The human civilization tends to grow exponentially within the past several decades, at the same pace of energy usage efficiency and information transportation speed. This brings us the dilemma between the dramatically increased energy demand and the limited energy storage. Hence, efforts have been made to find new energy sources, among which, the thermal nuclear fusion is considered to be most promising. For the past 60 years, great knowledge on fusion plasmas has been gained, both in plasma physics and fusion technologies. This chapter describes the current energy issue as well as a brief introduction on the toroidal magnetic configurations. Also briefly, both ideal and resistive MHD theories are presented to describe the equilibrium conditions. The dynamo mechanism in reversed field pinches is discussed and finally, descriptions on both RFX-mod and TJ-II stellarator are presented.

1.1 Energy Issue and Thermal Nuclear Fusion

Looking back to the history of human civilization, it is obvious that it is the efficiency of energy consumption and the efficiency of information transportation that determine the level of our civilizations. With fast development of our society, the usage of energy increases dramatically, as one could see from Figure 1.1, in which the time trace of energy consumption is listed from year 1965 to year 2015. The total energy consumption over this period increased up to 3.5 times and it is going to increase more in the following decades. The total energy we could use, however, is finite. Nowadays, we are strongly relying on the so-called traditional energy sources like oil, gas and coal, which are, unfortunately nonrenewable meaning that once they are consumed, there will be no more left (or it will take too long to recover). The increasing needs for energy are conflicting with the fact of finite energy storage and this brings us a very urgent issue: finding a sustainable way for our civilization. Among countless solutions proposed, the most reasonable one is to find new energy sources and this has been put into practice, as one could see in Figure 1.1. There are many new energy sources being explored and used currently but the percentage still remains low compared with the traditional ones.
Among those new energy sources, the thermal nuclear fusion is considered to be most promising in long time term. There are several 'obvious' advantages of nuclear

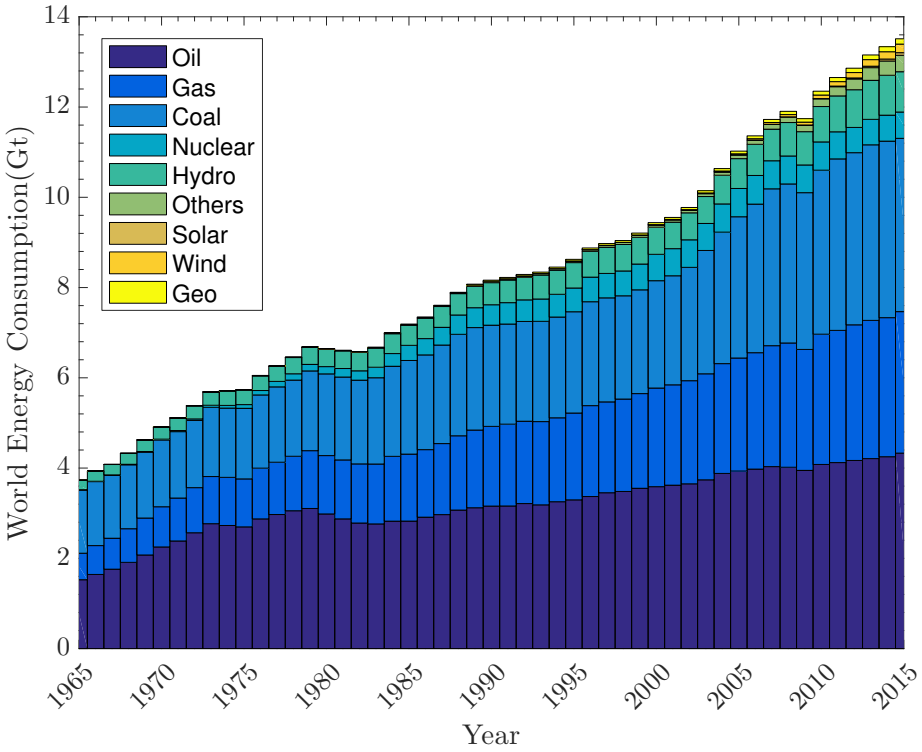

Figure 1.1: World wide energy use between year 1965 and 2015. The data is from British Petroleum.

fusion compared with other energy sources, given the fact that the fuels for fusion is hydrogen and its isotopes. First of all, the fuels for nuclear fusion are nearly 'beyond limit' in the foreseen future. There is a huge amount of deuterium (D), one of the isotopes of element hydrogen (H), in sea water and tritium (T), another isotope of H, is believed that it can be self-sustained during nuclear fusion reactions. Secondly, nuclear fusion brings no CO_2 emission, which is considered to be the main reason responsible for green house effect. Thirdly, there is hardly any danger compared with nuclear fission.

The main principle of energy production from nuclear fusion is to find a way to "fuse" two nuclei into one and during this process, there should be a mass change Δm with $\Delta m > 0$. Through this process, certain amount of energy will be released according to Einstein's equation: $E = \Delta m c^2$ with E the released energy and c the speed of light. This huge amount of energy per unit of fuel weight, compared with other energy sources, can be afterwards transformed into electricity for further use. In order

to achieve nuclear fusion, particles must overcome the repelling Coulomb force [1] which raises the requirement of seeking a way to heat particles up to a sufficiently high energy within sufficiently long time to compensate the energy dispassion. With such high energy, particles like hydrogen, deuterium, etc. will stay in excited state in which the electrons are no longer bounded to the nucleus. This new state of matter is named plasma, the fourth state of matter after solid, liquid and gas.
Fusion is one of the most efficient "power plant" in our universe. Our energy source, the sun, is working as a nuclear fusion power plant. The nuclei are pulled together by the huge gravitational force due to the huge mass the sun has. This naturally happened fusion reaction, unfortunately cannot be adopted on earth because there is no way to create such huge amount of mass and control its behavior. There are several alternative ways under consideration for the purpose of nuclear fusion energy production. The first one, inertial fusion, is the one adopted by National Ignition Facility (NIF) [2], located in the USA. It is designed to achieves nuclear fusion by means of giving particles enough energy within very short time, thanks to the 192 high power lasers. The simultaneous high power lasers arriving at the fuel target, which is a near perfect sphere, can generate high pressure and push the fuel sphere inwards. During this process, the fuel particles reach fusion condition within a time so short that they can not be repelled from each other and thus fusion reaction takes place. The disadvantage of such fusion method is that it is difficult to keep a long-time steady state operation, which is required by commercial use.
A more intuitive way, given that the fuels are made of charged particles, is to use magnetic field to confine the plasmas. The concept of magnetic confinement for fusion research is the first fusion idea proposed by Russian scientists and now it is the most popular way of fusion research worldwide. The condition of achieving fusion is believed to be related to three plasma parameters: plasma density $n(m^{-3})$, plasma temperature $T_e(KeV)$ and energy confinement time $\tau_E(s)$:

$$nT_e\tau_E > 5 \times 10^{21} \quad m^{-3} \cdot KeV \cdot s \tag{1.1}$$

This condition combines three plasma parameters and it was firstly derived by John D. Lawson [3]. The energy confinement time is defined as the ratio between internal energy (U) and input power (P):

$$\tau_E = U/P \tag{1.2}$$

From Equation 1.1 it is clear to see that the requirement of nuclear fusion is to sustain sufficiently large plasma density at high temperature within sufficiently long time.

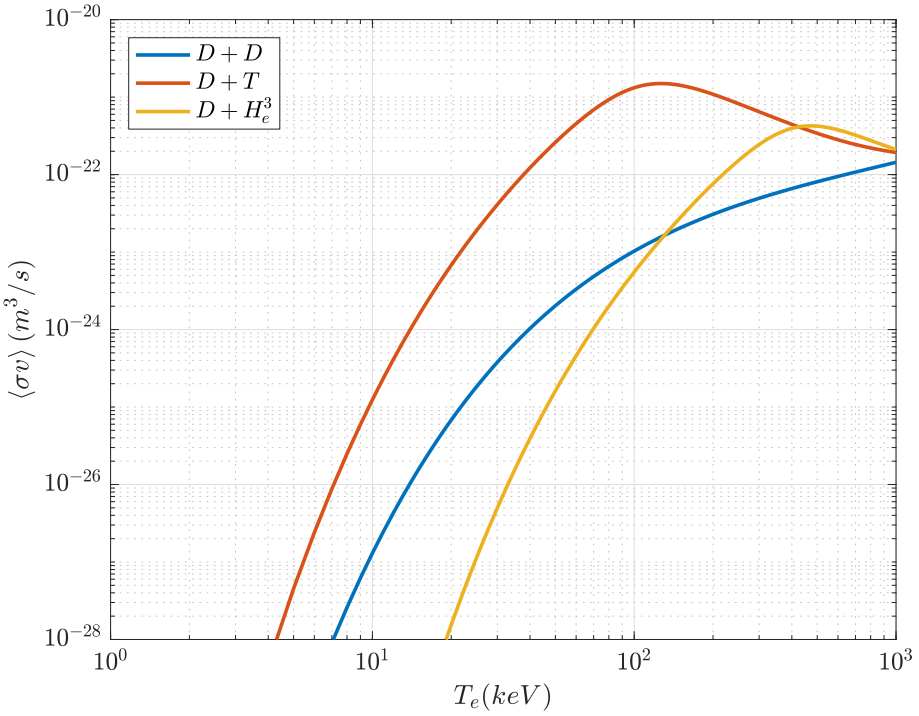

Figure 1.2: Reaction cross section of three typical fusion reactions: D-D, D-T and D-H_e^3. This figure is generated using the formulas presented in Reference [4].

In principle, any two elements before Fe could have fusion reaction under proper conditions [5]. However, the energy needed to heat particles to reach fusion conditions is quite different. Hence, it is reasonable to start with the easiest one, i.e. the one with the biggest reaction cross-section. Figure 1.2 shows the cross section of three different fusion reactions [6]:

$$
\begin{aligned}
D + D &\rightarrow H_e^3(0.82MeV) + n(2.45MeV) \\
D + T &\rightarrow H_e^4(3.5MeV) + n(14.1MeV) \\
D + H_e^3 &\rightarrow H_e^4(3.6MeV) + p(14.7MeV)
\end{aligned}
$$

And it is clear that the $D-T$ reaction has the biggest reaction cross-section at a relatively low temperature ($\sim 50keV$). Moreover, one of the products from $D-T$ reaction is helium (H_e) with 3.5 MeV energy, which is considered to be the critical heating source for self-sustained fusion reaction through the so-called α (H_e^4) heating process [7].

1.2 Toroidal Magnetic Configurations

There have been several magnetic configurations proposed and studied for the research of nuclear fusion with the help of magnetic confinement. They are, depending on the configurations, linear devices and toroidal devices. Linear devices are not suitable for fusion due to end loss issue [8]. By intuition, a toroidal devices without open ends could solve this problem. However, a toroidal device with only toroidal magnetic field still suffers bad plasma confinement due to the particle drifts induced by the curvature and gradient of the magnetic field [6, 8]. In order to overcome this issue, a rotational transform ι is introduced to the design of toroidal configurations and thus the magnetic field becomes helical windings. The rotational transform measures the winding properties of the field lines.
There are mainly two types of toroidal magnetic configurations categorized by how the magnetic field is generated. Tokamaks [6] and Reversed Field Pinches (RFPs) [9], as the magnetic field is generated by both external coils and the plasma current, belong to the so-called pinch family. The toroidal field in tokamaks is generated by external coils and the poloidal component is generated by the plasma current, which is induced by the primary transformer [10]. In advanced tokamak scenario, however, most of the poloidal field component is generated by the so-called 'bootstrap' current which is induced by the density gradient [11, 12]. This concept has been realized in JT-60U tokamak, showing that the bootstrap current fraction is up to 80% [13]. Nevertheless, the disadvantage for tokamak configuration is that it suffers a limitation of plasma current due to plasma instabilities [14]. Consequently, extra heating methods besides Ohmic heating are needed for plasma fusion in tokamaks. RFPs, however, can sustain very high plasma currents and this makes it to be considered a potential fusion device with only Ohmic heating. On the other hand, the generation of plasma current needs a time variation of magnetic field which is sustained by the primary transformer. This time variation makes both tokamaks and RFPs, on some level, not in steady states. To overcome this problem, a toroidal configuration which all the field components are generated by external coils is introduced. This device is the so-called stellarator [15]. Figure 1.3 shows a sketch of these two families. The left graph is a sketch of stellarator and the right one is a sketch of pinch. In the left graph, the red coils aligned toroidally are the toroidal field coils and the green helical ones are helical field coils. In the right graph, the red cylinder in the device center is the primary transformer, responsible for the production of the plasma current. The red coils aligned toroidally are the toroidal field coils and the two green ones on the top and bottom of the device are the vertical stabilization coils. The stabilization coils are introduced because, due to the existence of Shafranov shift [16] in toroidal

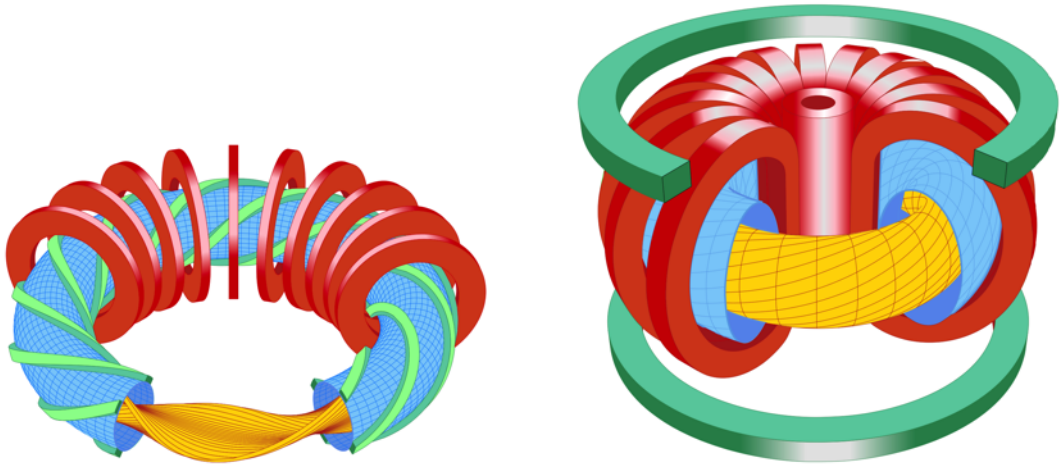

Figure 1.3: Sketch of two types of toroidal magnetic configurations. The left figure represents stellarator family and the right one represents pinch family. The stellarators have complicated coil designs while coils used in pinch family have simpler shape.

devices, the plasma position needs to be optimized in order to prevent the plasma from touching the first wall. The stellarator shows a much more complicated magnetic coil design than one in pinch family. Consequently, the manufacture process for magnetic coils is more complex for stellarators than for pinches. On the other hand, due to lack of plasma current in stellarators, it is almost free of disruptions [17].

The magnetic field designed to confine plasmas in a toroidal configuration contains two components: the poloidal component and the toroidal component. The corresponding coordinate system to describe this toroidal system is the so-called toroidal coordinate system (r,θ,ϕ), defined in Figure 1.4: r is the radial coordinate, θ and ϕ are the poloidal and toroidal angles, respectively. The two components of the magnetic field are linked by the so-called safety factor q. In cylindrical approximation, it is defined as:

$$q(r) = -\frac{r}{R_0}\frac{B_\phi(r)}{B_\theta(r)} \tag{1.3}$$

The safety factor is introduced to describe the winding of magnetic field lines: how many poloidal turns a field line completes before it completes one toroidal circle. Its inverse quantity is the rotational transform: $\iota/2\pi = 1/q$.

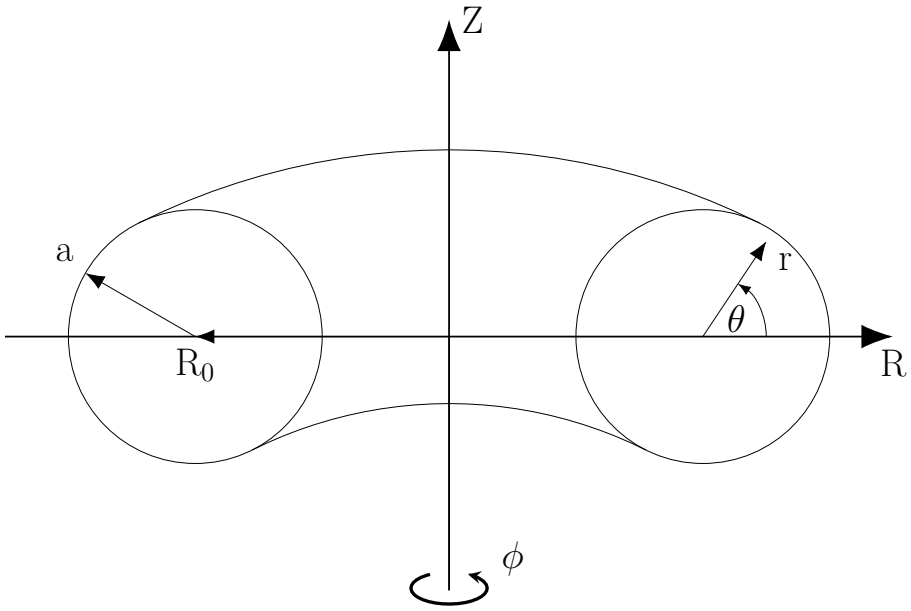

Figure 1.4: A sketch of magnetic coordinate. R_0 is the major radius, a is the minor radius, r is the radial coordinate, θ is the poloidal angle and ϕ is the toroidal angle. The magnetic surfaces share one axis at which $r = 0$.

1.3 Ideal MHD

The goal for energy production from fusion reactions is to keep the plasmas in fusion reaction state for a long time, i.e., the system should be in steady state. On the purpose of understanding the physics of fusion plasmas, one need to study the equilibrium state of fusion plasmas. A large variety of plasma properties, such as the magnetic equilibria or several instabilities can be described by a fluid model called Magnetohydrodynamics (MHD) [18]. It contains the fluid equations as well as Maxwell equations. The fluid equations can be derived from Maxwell-Vlasov equation, which is kinetic description of plasmas, by taking different order of velocity moments for distribution functions. The *ideal* MHD equations, with the main assumption that plasmas have zero resistivity, are:

Fluid Equations:

$$\begin{cases} \text{Mass} & \partial\rho/\partial t + \nabla\cdot(\rho\boldsymbol{u}) = 0 \\ \text{Momentum} & \rho(\partial\boldsymbol{u}/\partial t + \boldsymbol{u}\cdot\nabla\boldsymbol{u}) = -\nabla P + \boldsymbol{J}\times\boldsymbol{B} \\ \text{Energy} & \dfrac{d}{dt}\left(p/\rho^{\gamma}\right) = 0 \end{cases}$$

$$\textbf{Maxwell Equations:} \begin{cases} \text{Gauss}'\text{s} \quad \text{Law} & \nabla \cdot \boldsymbol{B} = 0 \\ \text{Gauss}'\text{s} \quad \text{Law} & \nabla \cdot \boldsymbol{E} = q/\epsilon_0 \\ \text{Ampere}'\text{s} \quad \text{Law} & \nabla \times \boldsymbol{B} = \mu_0 \boldsymbol{J} \\ \text{Faraday}'\text{s} \quad \text{Law} & \partial \boldsymbol{B}/\partial t = -\nabla \times \boldsymbol{E} \\ \text{Ohm}'\text{s} \quad \text{Law} & \boldsymbol{E} + \boldsymbol{u} \times \boldsymbol{B} = 0 \end{cases}$$

Where ρ is the mass density, $\boldsymbol{u}$ is the flow velocity, P is the pressure, $\boldsymbol{J}$ is the current density, $\boldsymbol{B}$ is the magnetic field, $\boldsymbol{E}$ is the electric field, q is the charge of charged particles, ϵ_0 is the vacuum permittivity and μ_0 is the vacuum permeability. The basic assumptions used in ideal MHD equations are:

- Quasi-neutrality, electron and ion density $n_e \cong n_i$.
- Plasma scale length $\gg$ Larmor radius. This condition indicates that plasmas contain large amount of charged particles.
- Typical frequency $\ll$ Cyclotron frequency. This condition indicates the characteristic time of the plasma system is much longer than the characteristic time of one charged particle.
- Zero plasma resistivity and viscosity
- No trapped particles (no neoclassical effects)

Here the Larmor radius is the gyration radius of charged particles along a field line and it is given as $\rho = mv_\perp/q|B|$ with m the particle mass, $v_\perp$ the velocity component perpendicular to the field line, q is the charge of particles and B is the modulus of the magnetic field. In equilibrium state, which is required by steadily operated fusion devices, we have: $\partial/\partial t = 0$ and $\boldsymbol{u} = 0$. Thus the equilibrium condition could be easily obtained from the 8 equations mentioned above:

$$\boldsymbol{J} \times \boldsymbol{B} = \nabla P \tag{1.4}$$

Equation 1.4 shows that a plasma equilibrium is sustained by the force balance between $\boldsymbol{J} \times \boldsymbol{B}$ and the pressure gradient ∇P. Moreover, it also shows that both plasma current and the magnetic field lies on a surface defined by constant pressure:

$$\boldsymbol{J} \cdot \nabla P = 0 \qquad \boldsymbol{B} \cdot \nabla P = 0 \tag{1.5}$$

This can be easily proved by applying dot product of vector $\boldsymbol{J}$ and $\boldsymbol{B}$ on Equation 1.4 respectively. These surfaces with constant pressure are the so-called flux surfaces.

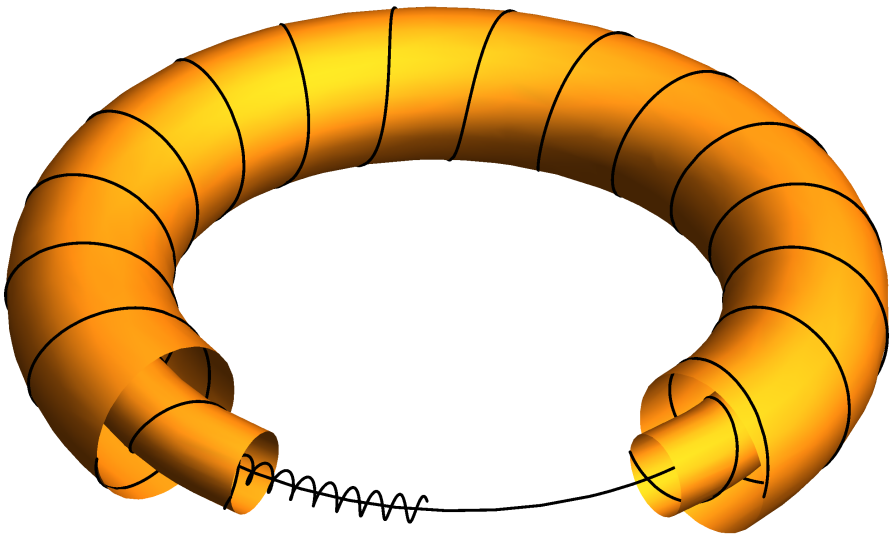

Figure 1.5: A sketch of flux surfaces, field lines (black helical) and the gyration of a charged particle along one magnetic field line (the black half spring in the center, not in scale with the torus) is presented.

Charged particles which follow the field lines are thus bonded on the surfaces and the radial energy or particle loss are significantly reduced and the only loss is due to the collisions among charged particles. The field lines are winding on the flux surfaces in the helical direction. A sketch of flux surfaces, helical field line as well as the gyration of a charged particle along one magnetic field line is shown in Figure 1.5. The yellow torus represents the flux surfaces and the black helical lines represent the magnetic field lines which lie on the surfaces. The small winding along the center field line represents the gyration motion of a charged particle. Note that the gyration is not in the correct scale.

The shape of the magnetic surfaces varies with the magnetic field conditions and it always has the Shafranov shift due to the toroidicity of the configurations. The Shafranov shift is induced by the toroidicity in the sense that on one flux surface, the area in high field side S_H is smaller than in low field side S_L and thus a net force towards low field side is generated: $P(S_L - S_H)$. Figure 1.6 shows a sketch of the Shafranov shift in circular plasmas. The black circle is the vacuum chamber and the red circle represents the equilibrium plasma cross-section. The shift between the vacuum chamber center and the plasma equilibrium center $\Delta(r)$ is the Shafranov shift. This simplified model shows that all the flux surfaces are shifted towards low

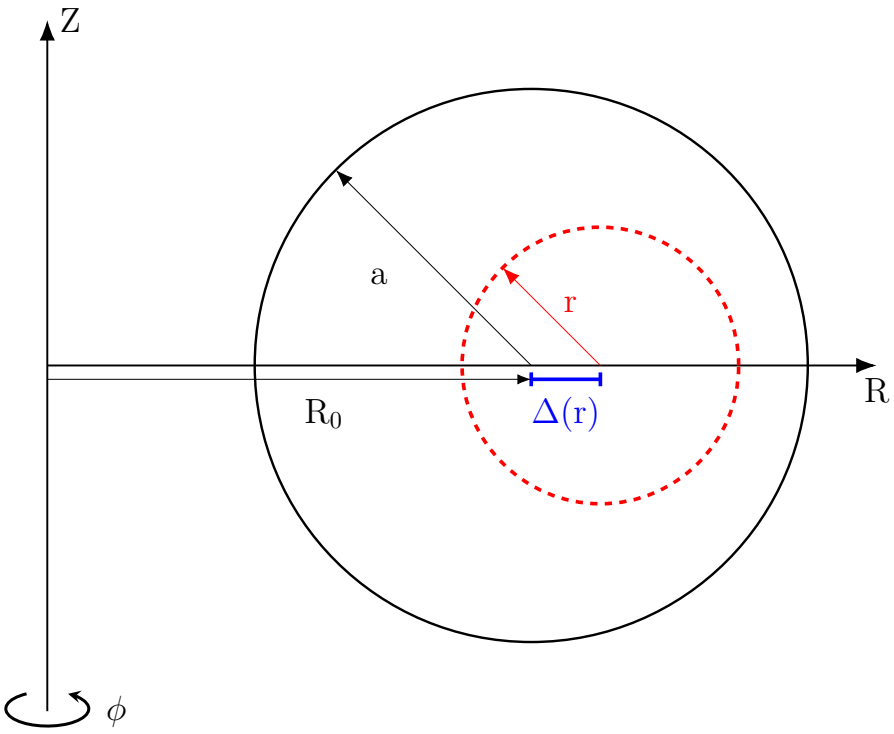

Figure 1.6: A sketch of Shafranov shift in a circular plasma with R_0 the major radius, a the minor radius and ϕ the toroidal direction. The black circle is the vacuum vessel and the red dashed circle indicates a flux surface shifted outwards. The quantity Δr is the Shafranov shift and it usually is a function of r.

field side and since in general the Shafranov shift is a function of r, the shift value is different for each flux surfaces.

The existence of Shafranov shift leads to different metrics compared to the concentric circle configuration and this brings complexity in transforming between Cartesian coordinate and the flux coordinate. From Equation 1.4 we know that the plasma pressure, which is the product of both plasma density n and plasma temperature T, $P = knT$, is a function of flux surfaces with k the Boltzmann constant. In principle the plasma density and temperature are not necessarily functions of flux surfaces. Nevertheless, experimental observations have shown that the plasma density and temperature can be considered as functions of flux surfaces. Thus, the use of flux coordinates allows one write simpler equations (1.5 dimensional, meaning quantities averaged over the poloidal angle) to study various phenomena such as plasma stability

and transport process. Moreover, things could get more complicated if the topology of the magnetic field is modified further by other phenomena.

1.4 Resistive MHD

In the framework of ideal MHD, the main assumption is that the plasma resistivity is zero and the following consequence is that the plasma topology remains unchanged. However, even a small, non-zero plasma resistivity could change the field topology and this introduces further complexity into the metrics. The theory considering a finite plasma resistivity is called *resistive* MHD [19, 20]. Here we consider the plasma with a non-zero resistivity η. The corresponding Ohm's law is:

$$\boldsymbol{E} + \boldsymbol{v} \times \boldsymbol{B} = \eta \boldsymbol{J} \tag{1.6}$$

Together with Faraday's Law and $\nabla \times \boldsymbol{B} = \mu_0 \boldsymbol{J}$, using the vector relation $\nabla \times \nabla \times \mathcal{A} = \nabla(\nabla \cdot \mathcal{A}) - \nabla^2 \mathcal{A}$, the induction equation is obtained:

$$\partial \boldsymbol{B}/\partial t = (\eta/\mu_0)\nabla^2 \boldsymbol{B} + \nabla \times (\boldsymbol{v} \times \boldsymbol{B}) \tag{1.7}$$

The dimensionless form of induction equation is thus:

$$\partial \boldsymbol{B}/\partial \hat{t} = (1/R_m)\hat{\nabla}^2 \boldsymbol{B} + \hat{\nabla} \times (\hat{\boldsymbol{v}} \times \boldsymbol{B}) \tag{1.8}$$

Where $\hat{t} = tV_A/L$, $\hat{\nabla} = L\nabla$, $\hat{\boldsymbol{v}} = \boldsymbol{v}/V_A$, L is the typical plasma length and V_A is the Alfvén wave velocity [21]. $R_m = \mu L V_A/\eta$ is the so-called Reynolds number and it is also referred to as the Lundquist number $S = \tau_R/\tau_A$ where $\tau_R \sim \mu_0 L^2/\eta$ is the characteristics resistive diffusion time and $\tau_A \sim L/V_A$ is the Alfvén time. The Lundquist number is a quantity indicating how far the plasma is from the ideal MHD, i.e., when $S \to \infty$, the plasma is close to ideal MHD. On the right side of induction equation, there are two parts. When the resistivity $\eta \to 0$, the induction equation becomes to the form of ideal MHD. In such condition, there is no relative movements between the plasma and the magnetic field and the plasma is 'frozen' in the magnetic field. On the other hand, when $(1/R_m)\hat{\nabla}^2 \boldsymbol{B} > \hat{\nabla} \times (\hat{\boldsymbol{v}} \times \boldsymbol{B})$, the induction equation becomes a diffusion equation of the field lines.
One of the most important result from resistive MHD is the so-called tearing mode. The magnetic perturbations, in general tend to bend the magnetic field lines. This bending effect increases the magnetic field energy. This is true as long as the wave vector of the perturbation $\boldsymbol{k}$ is not perpendicular to the field lines: $\boldsymbol{k} \cdot \boldsymbol{B} \neq 0$. In such conditions, the magnetic perturbations are damped and the equilibrium of the

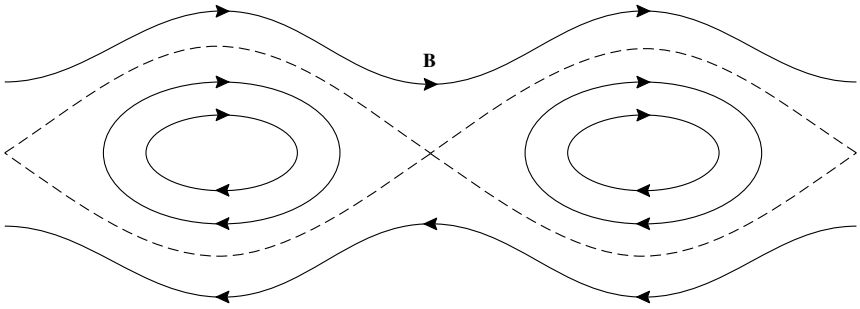

Figure 1.7: A typical magnetic island is presented. The field lines reconnect and the topology of magnetic field changes. This figure is from Reference [22].

plasma is thus stable against such perturbations. However, this stabilization effect vanishes when $\boldsymbol{k} \cdot \boldsymbol{B} = 0$. In cylindrical approximation, $\boldsymbol{k} \equiv \boldsymbol{k}(r) = (k_r, k_\theta, k_\phi)$. With the wave length in poloidal direction $\lambda_\theta = 2\pi r/m$ and in toroidal direction $\lambda_\phi = 2\pi R/n$, the wave vector in these two directions are: $k_\theta = m/r$ and $k_\phi = n/R$. Hence, the unstable condition is:

$$\boldsymbol{k} \cdot \boldsymbol{B} = \frac{m}{r} B_\theta + \frac{n}{R} B_\phi = 0 \tag{1.9}$$

Recall the definition of safety factor q, Equation 1.9 can be written as:

$$q(r) = -\frac{r}{R}\frac{B_\phi}{B_\theta} = -\frac{m}{n} \tag{1.10}$$

Now we arrive at a critical point that the unstable positions are those where the mode number m and n are rational numbers and these unstable modes are the so-called tearing modes. The result of tearing mode is that it modifies the magnetic topology through reconnection process of magnetic field lines. Figure 1.7 shows a typical magnetic island after reconnection of field lines. The reconnection of field lines occurs in the resonant position and the topology of magnetic field thus changed. The existence of magnetic islands distorts the nested flux surfaces and gives rise to the three dimensional properties of the transport process in fusion plasmas.

1.5 Equilibrium in RFPs: the Dynamo Mechanism

In a typical RFP discharge, the poloidal component of the magnetic field (B_θ) is comparable with the toroidal component (B_ϕ) in their amplitudes and the poloidal component B_θ dominates in the outer region where B_ϕ reaches zero value and changes sign. This magnetic configuration is quite different from the tokamak where the toroidal component B_ϕ is much larger than poloidal component B_θ. Moreover, the safety factor profile in RFPs features $q < 1$ and its sign changes in the edge. A typical magnetic field profile with the poloidal and toroidal components is shown in Figure 1.8a, plotted as a function of the radius r normalized by the minor radius a of the poloidal cross-section. The corresponding q profile in RFX-mod is shown in Figure 1.8b. This q profile leads to the possibility of many MHD tearing modes, which are represented by the black dots shown in Figure 1.8b. In the plasma center, many tearing modes resonant and the magnetic islands overlap with each other, breaking the nested flux surfaces, leading to a degradation of plasma confinement with increased transport properties.

The edge reversal of toroidal magnetic field is a self-organized behavior, by means of the so-called dynamo mechanism which is related to the non-linear interactions of many MHD tearing modes [23]. To be more specific, the non-linear interactions among resonant modes generate a non-zero part between velocity and magnetic perturbations: $\left\langle \tilde{\boldsymbol{v}} \times \tilde{\boldsymbol{b}} \right\rangle$ in Ohm's law with symbol $\langle \cdots \rangle$ meaning averaged value, playing a role of effective electric field. The non-zero $\left\langle \tilde{\boldsymbol{v}} \times \tilde{\boldsymbol{b}} \right\rangle$ connects the toroidal and poloidal plasma current and as a consequence, the toroidal energy is converted into poloidal energy through the dynamo mechanism and part of the toroidal magnetic field is thus generated by the toroidal current.

A physical picture of the dynamo mechanism is presented in order to get a better understanding. A RFP discharge is presented in Figure 1.9, with the magnetic (upper graph) and plasma current (lower graph) profiles along the normalized minor radius r/a. The vertical dashed line represents the radial location of the reversal point, where the toroidal field B_ϕ reaches zero. It is clear to see that at the reversal point, the value of the poloidal current $\boldsymbol{J}_\theta$ is not zero. By checking the induction equation and Ohm's law in the reversal location:

$$\partial \boldsymbol{B}/\partial t = -\nabla \times \boldsymbol{E} \qquad \boldsymbol{E} + \boldsymbol{v} \times \boldsymbol{B} = \eta \boldsymbol{J} \tag{1.11}$$

Where η is the plasma resistivity. One obtains $\boldsymbol{E}_\theta = 0$ and $\boldsymbol{E}_\theta = \boldsymbol{\eta} \boldsymbol{J}_\theta$. The following result $\boldsymbol{J}_\theta = 0$ disagrees with the discharge profile. In fact, the poloidal current at

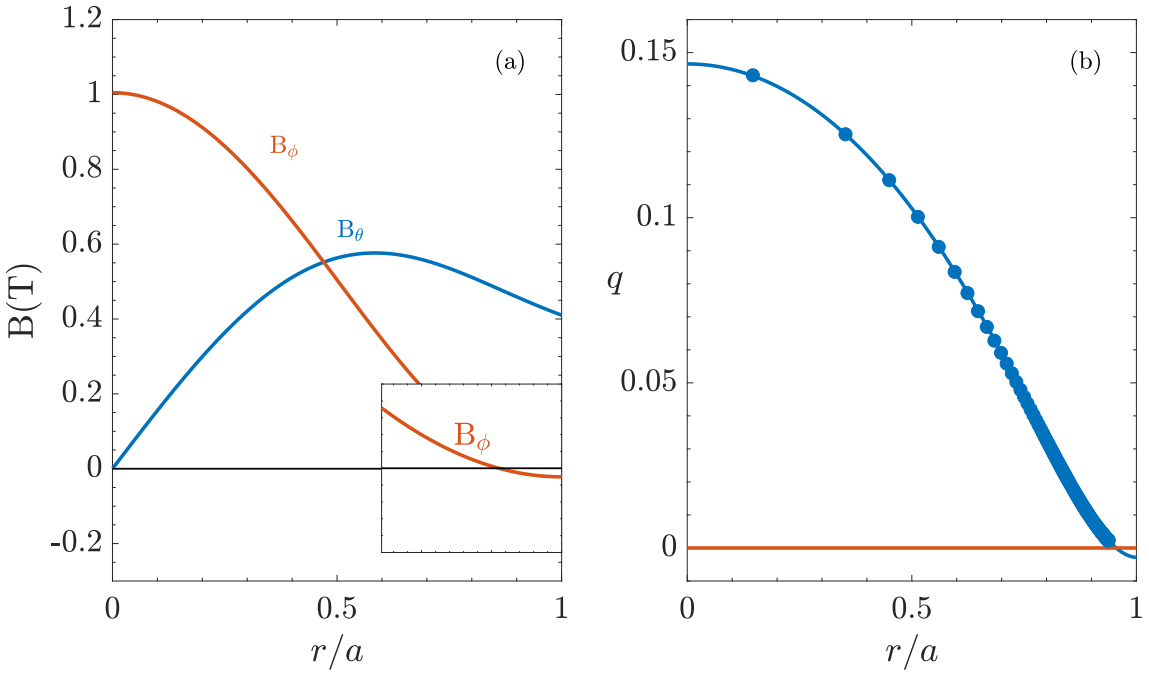

Figure 1.8: (a). A typical magnetic field profile in a RFX discharge is presented with both poloidal (in blue) and toroidal (in red) components, with the black horizontal line representing $\boldsymbol{B} = 0$. The amplitude of poloidal field dominants in the edge and the toroidal field changes sign near the edge. (b). The corresponding safety factor q profile is presented as a function of the radius r normalized by the minor radius a. The circle markers on the curve are the corresponding resonant MHD modes with the horizontal line indicating $q = 0$.

the reversal location is not generated by $\partial \boldsymbol{B}_\phi / \partial t$. Instead, it is generated through the dynamo mechanism mentioned above.

Taylor Relaxation Theory

The first explanation of the RFP configuration was proposed by J. Brian Taylor [24]. The main principle of his theory is that the RFP plasmas try to seek the minimum energy. In his theory, the plasma pressure and velocity are neglected. The total magnetic energy is defined as:

$$W = \int_V \frac{B^2}{2\mu_0} dV \tag{1.12}$$

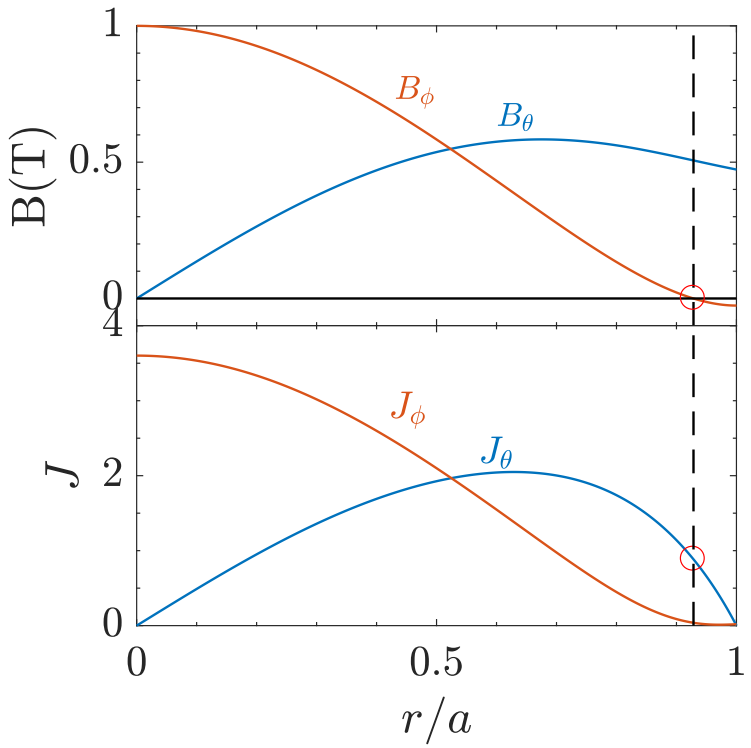

Figure 1.9: A model for one RFP plasma discharge. The profiles of two magnetic field components B_ϕ and B_θ are presented in the upper graph, plotted as a function of the normalized minor radius. The two corresponding current density profiles $\boldsymbol{J}_\phi$ and $\boldsymbol{J}_\theta$ are presented in the lower graph.

The constrain proposed by Taylor is that the system has constant magnetic helicity:

$$K = \int_V \boldsymbol{A} \cdot \boldsymbol{B} dV \tag{1.13}$$

Where $\boldsymbol{A}$ is the vector potential defined as $\boldsymbol{B} = \nabla \times \boldsymbol{A}$. It is true that the magnetic helicity is conserved in non-resistive plasmas. When it comes to resistive plasmas, the magnetic helicity K is considered to be approximately constant if the variation of K is much slower than the magnetic energy variation [25].
By checking the force balance equation and neglecting the plasma pressure: $\boldsymbol{J} \times \boldsymbol{B} = \nabla P = 0$, one obtains a force free system with $J = \mu B$, where μ is constant. In cylindrical configurations, the solutions are the first and second kind of Bessel

functions (J_0 and J_1) [23]:

$$\begin{cases} B_r(r) = 0 \\ B_\theta(r) = B_0 J_1(\mu r) \\ B_z(r) = B_0 J_0(\mu r) \end{cases}$$

The above mentioned theory developed by Taylor shows that the plasma behavior is mainly affected by the global plasma parameters. Hence, before further discussion, we define two global plasma parameters:

$$\text{Reversal parameter:} \qquad F = B_\phi(a)/\langle B_\phi \rangle \tag{1.14}$$

$$\text{Pinch parameter:} \qquad \Theta = B_\theta(a)/\langle B_\phi \rangle \tag{1.15}$$

Where $B_\theta(a)$ and $B_\phi(a)$ are the poloidal and toroidal magnetic field in the edge, respectively. The symbol $\langle \cdots \rangle$ indicates the volume average. The comparison between Taylor's theory and the experimental data shows a disagreement, especially in the plasma edge. A modified theory known as $\alpha - \Theta_0$ model [26], adopting a non-constant μ along the normalized minor radius r/a as well as considering a non-zero pressure, shows a good agreement with experimental data [23].
The two global parameters defined above allow us to go back to the dynamo mechanism for further discussions. The dynamo mechanism is a global RFP plasma behavior. This self-organized plasma behavior allows the plasma current which flows in the toroidal direction, flows in the poloidal direction and part of the toroidal field is thus generated by the toroidal plasma current through this process. The contribution of the toroidal magnetic field via dynamo mechanism can be expressed as:

$$\langle B_\phi \rangle = \langle B_{\phi,dynamo} \rangle + B_\phi(a) \tag{1.16}$$

Where $\langle B_{\phi,dynamo} \rangle$ is the average paramagnetic toroidal field self-generated through dynamo mechanism and $B_\phi(a)$ is the toroidal field in the plasma edge. Hence, $\langle B_{\phi,dynamo} \rangle$ is an indicator for the dynamo mechanism. One can easily get:

$$(1 - F)/\Theta = \langle B_{\phi,dynamo} \rangle / B_\phi(a) \tag{1.17}$$

So the quantity $(1 - F)/\Theta$ is the dynamo parameter for RFP plasmas.

1.6 Experimental Devices

This dissertation work has been carried out on two machines: the RFX-mod [27] reversed field pinch and the TJ-II stellarator [28]. Here brief descriptions together with main diagnostics of these two toroidal configurations are presented.

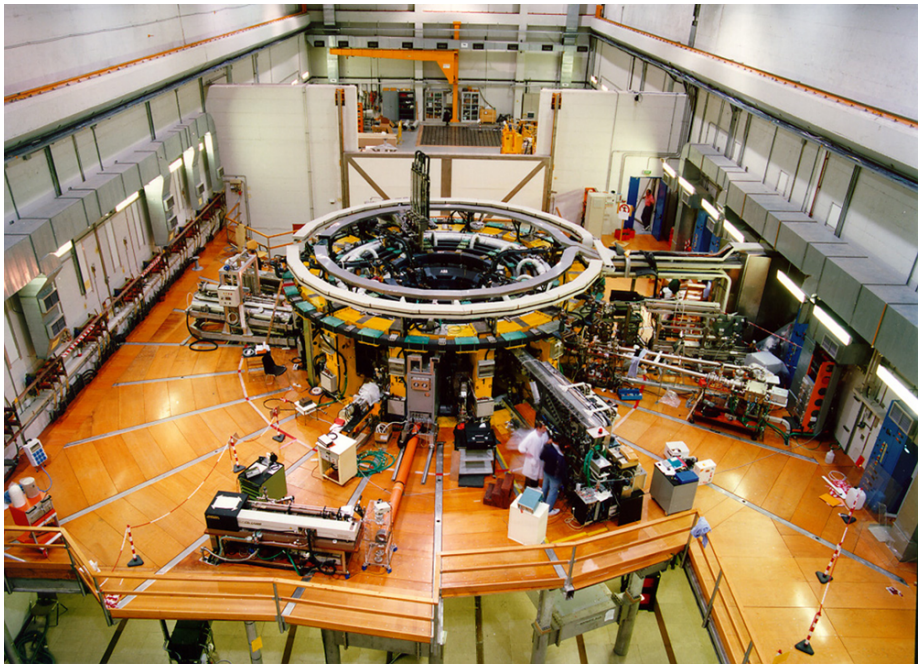

Figure 1.10: A birdview of the RFX-mod device, located in Padova, Italy.

Revered Field eXperiment

The Reversed Field eXperiment modified (RFX-mod) [27] is currently the largest RFP in the world, located in Padova, Italy. It has a major radius of $R_0 = 2m$ and a minor radius of $a = 0.459m$. It is capable to reach plasma current up to 2 MA. Figure 1.10 shows the bird view of the device. One of the most important innovations in RFX-mod is the feedback control system based on 192 active saddle coils covering the whole plasma volume (4 poloidally and 48 toroidally). This feedback system functions to suppress the radial magnetic perturbations. Here a brief description of diagnostics on RFX-mod is present.

- Magnetic diagnostics. Four Rogowski coils between the vacuum vessel and the shell for measurement of toroidal magnetic flux as well as plasma current. (10 toroidal and 8 poloidal voltage loops for measurements of flux variations.) 192 pick-up coils, distributed along 48 toroidal directions and 4 poloidal directions, measure toroidal and poloidal components of magnetic fields. 192 saddle probes distributed the same as the pick-up coils, measuring the radial component of the field, coupled to the active control coils.

- Tomographic reconstruction [29]. It is meant for the reconstruction of the poloidal emissivity map. The diagnostic is composed by 3 vertical fans each with 19 lines of sight and 1 horizontal fan with 21 lines of sight. The total 78 lines of measurements almost entirely cover the plasma cross section.

- Thomson scattering diagnostic [30]. It features spacial resolution of 84 points along the diameter of the vacuum chamber. The laser path lays on the mid-plane (poloidal angle $\theta = 0(\pi)$) at the toroidal angle $\phi = 82.5°$. The maximum capacity per discharge is around 20:25 pulses.

- A multi-chord interferometer [31, 32]. It measures the electron density averaged along 14 lines of sight. The measurement is performed measuring the phase variation induced in a CO_2 laser beam ($\lambda = 5.4\mu m$) that passes through the plasma.

- Spectroscopic diagnostics [33]. It measures line intensities of radiation emitted by main gas and by impurities, in order to calculate their influxes at the edge, the toroidal flow of the plasma and the effective charge.

- Soft-X Rays multi-filter diagnostic [34]. It is used for measuring electron temperature at the center of the plasma by means of comparing SXR emissions measured by differently filtered silicon detectors. It allows a higher time resolution with respect to the Thomson scattering, but with a lower spatial resolution; 16 chords with different filter thicknesses (40 μm, 75 μm, 100 μm, 150 μm) are used in order to measure temperature in a wider range of emission levels.

- An integrated system of internal sensors (ISIS) [35], which includes poloidal and toroidal arrays of 139 magnetic pick-up coils and 97 electrostatic (Langmuir) probes (used to measure and correlate fluctuations of electric and magnetic fields), and 8 calorimetric sensors.

TJ-II Stellarator

TJ-II flexible Heliac [28] is a mid-size stellarator with fourfold periodicity under operation in CIEMAT, Madrid, Spain. It has a major radius $R_0 = 1.5m$ and minor radius $a = 0.22m$. The magnetic field on axis is up to 1.2T. Figure 1.11 shows a CAD view of TJ-II. In TJ-II, the magnetic trap is obtained by means of various sets of coils that completely determine the magnetic surfaces before plasma initiation. The toroidal field is created by 32 coils. The three-dimensional twist of the central

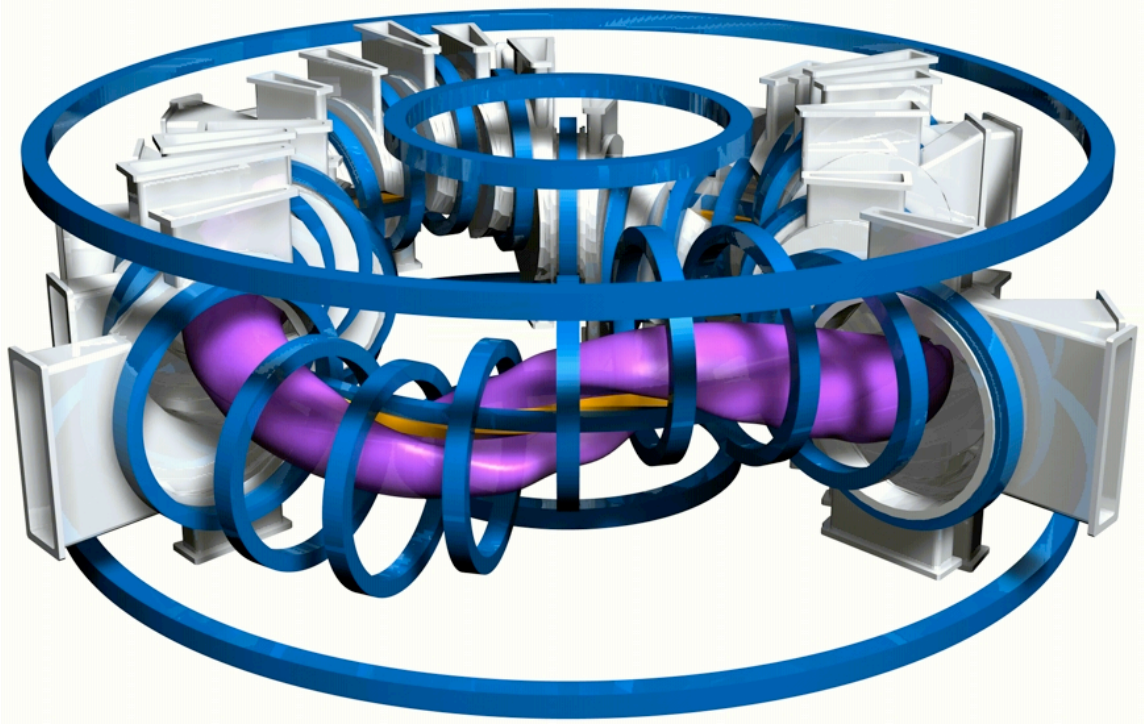

Figure 1.11: A CAD view of TJ-II stellarator is presented The blue parts are magnetic field coils. The gray parts are the structure of the machine and the ports for diagnostic usage. The purple helical part represents the plasmas.

axis of the configuration is generated by means of two central coils: one circular and one helical. The horizontal position of the plasma is controlled by the vertical field coils. The combined action of these magnetic fields generate bean-shaped magnetic surfaces. The heating systems are: Electron Cyclotron Resonant Heating, Neutral Beam Injection (NBI), Electron Bernstein Wave Heating. The fueling systems are gas puff, NBI and pellet injector.
The main diagnostic systems installed on TJ-II are:

- A set of magnetic field diagnostic. There are two straight arrays of Mirnov coils [36, 37] and one poloidal array with 15 coils. The Mirnov coils are with cylindrical shape and they measure the position of plasmas. Besides, there are two sets of Rogowski coils installed to measure the poloidal magnetic flux. Also two internal diamagnetic loops are installed to provide the toroidal loop voltage.

- Electron Cyclotron Emission [38]. Electron temperature profiles are measured at TJ-II by means of a 16 channel heterodyne radiometer, covering the frequency range 50-60 GHz, corresponding to the second harmonic of electron cyclotron emission (ECE) in X-mode polarization at a magnetic field of 0.95 T on the plasma axis.

- Soft X-rays. The TJ-II multichannel soft X-ray system consists of 5 cameras with 16 channels each, allowing tomographic reconstruction of the plasma emissions [39, 40, 41].

- Bolometry. TJ-II has several bolometry systems [42, 43]. Three 20-channel pinhole cameras, monitoring the same poloidal section and used for tomographic reconstructions [44] of the total plasma emissivity [45].

- Four spectroscopy system: 1. Multichannel system with nine-channel, high-resolution, spectroscopic diagnostic system for measurements of ion impurity temperature and poloidal rotation via passive emission spectroscopy. 2. Toroidal rotation measurement. 3. Vacuum ultraviolet spectrometer (VUV) spectroscopy, covers wavelength from 20 to 300 nm on the purpose of obtaining the impurity ion temperature as well as its time evolution. 4. Charge exchange recombination spectroscopy.

- Charge Exchange Spectroscopy. It is used to obtain the ion temperature profile, assuming a Maxwellian energy distribution function.

- Fast Camera is installed for various studies like turbulence, dust, 2-dimensional electron and ion temperature imaging.

- Interferometry [46] contains two parts: the microwave interferometer located at $\phi = 264.4°$. The probing beam has an inclination of 18.7° with respect to the vertical and a frequency of 140 GHz, corresponding to a wavelength of $\lambda = 2.14$ mm. There is also a two-color interferometry (CO_2 with 10.6 μm and NdYAG with 1.064 μm) provides the line integrated density.

- The reflectometry contains three parts: an amplitude modulation reflectometry system [47]; a fast frequency hopping reflectometer [48] and a doppler reflectometer [49]. The amplitude modulation reflectometry is used for density profile measurement with a temporal resolution of 2 ms. The fluctuation reflectometer works in the frequency range between 33-50 GHZ and it was used to study the velocity shear layer and the radial position of its origin. Doppler reflectometer, located at $\phi = 337°$ measures plasma density fluctuation velocities

and their wave number spectra. The spacial resolution of doppler reflectometer is about $r/a = 0.6 : 0.9$ with a the minor radius. The perpendicular wavenumber can be selected between $k_\perp = 3$ and $15cm^{-1}$.

- Heavy ion beam probe [50] has been installed for measurements of plasma electric potential, electron density and poloidal magnetic field component. These quantities are measured at one plasma location and it can scan through the plasma cross-section.
- Two Langmuir probe system [51] installed at position $\phi = 38.2°, R = 134cm$ and position $\phi = 195°$ for plasma potential and plasma density measurements. Also it can provides turbulence information. Several designs of the probe can be mounted into the system like a rake probe, a multi-pin probe and a biasing probe.
- Thomson scattering diagnostic [52] located at $\phi = 14.5°$. It provides electron temperature, density and pressure profiles in a single discharge.

1.7 Summary

This chapter states out the importance of the realization of magnetic confined fusion. Three main types of toroidal configurations are presented and the ideal and resistive MHD are also briefly discussed, together with a short discussion on magnetic equilibrium. Afterwards, the dynamo mechanism which is the key physics sustaining the equilibrium in RFP configurations is presented and finally, two toroidal configurations related to this dissertation work are briefly described.
One of the main issues for realization of fusion is that the plasmas suffer bad confinement properties, which are caused by high transport processes both in energy and particles. Intensive work has already been carried out on the topic of 1.5 dimensional transport, considering the plasmas possess toroidal or helical symmetry, as well as nested flux surfaces. In the next chapter, the *three dimensional* effect on transport properties, induced by the presence of *magnetic islands* is discussed, together with a brief discription of neoclassical transport and stochastic transport. These two different transport theories are relevant for the transport study in TJ-II stellarator and RFX-mod, respectively.

2

Three Dimensional Transport Induced by the Presence of Magnetic Islands

Transport is a common phenomenon in fusion plasmas. The transport phenomenon is induced by the Coulomb collisions between charged particles and through which, mass, momentum and energy are transferred. Consequently, the transport phenomenon strongly affects the plasma confinement properties. In tokamak and stellarator configurations where the flux surfaces are conserved, one of the possible transport theory, named neoclassical transport, can be used to well described the transport phenomenon, especially in low collisionality regime. However, the existence of the magnetic islands in above mentioned devices breaks the symmetry as well as nested flux surfaces and the transport process is intrinsically three dimensional. In RFPs, similar situation where many tearing modes resonate also brings up three dimensional transport problems and the transport process is dominated by stochastic transport. This chapter describes the three dimensional transport induced by the presence of magnetic islands. General descriptions on both neoclassical transport and stochastic transport theory are also presented.

The ultimate goal for fusion research is to realize a magnetic configuration sustaining a continuous energy production state. This requires good plasma confinement properties and consequently, the study of transport phenomena gains great importance. Transport phenomenon is caused by the Coulomb collisions between charged particles, whose velocity $\boldsymbol{v}$ could be expressed into two parts: parallel $\boldsymbol{v}_{\parallel}$ and perpendicular $\boldsymbol{v}_{\perp}$ components, with respect to the direction of the magnetic field lines. The parallel component usually dominates the motion of charged particles. In toroidal configurations with nested flux surfaces like tokamaks and stellarators, particles and energy are strongly constrained on the flux surfaces and the main losses from the system are through transport process across the flux surfaces. This transport mechanism could be explained by the so-called neoclassical transport theory. On the other hand, in toroidal configurations without preserved flux surfaces like RFPs, the particle and energy losses are induced by the parallel transport process along the field lines. In such configurations, it is the so-called stochastic transport that dominates the transport process. This chapter presents descriptions of these two theories, to-

gether with a brief description of the three dimensional transport issue rising from the presence of the magnetic islands.

2.1 Neoclassical Transport

The transport in magnetized plasmas is essentially induced by the Coulomb collisions between charged particles. The Coulomb collisions, unlike the conventional collisions between neutral particles, are long-range, elastic collisions induced by the electric field generated by each charged particle. In a uniform magnetic field, charged particles are bonded along the the field lines by the Lorentz force. This is the so-called classical transport theory [53]. The transport losses in tokamaks were expected to follow the predictions of classical transport theory, considering the nested flux surface, on which the particles are bonded. However, the experimental results disagreed with this prediction and people came to realize that the orbits in toroidal configurations are much bigger than classical gyro-orbits [54, 55, 56, 57]. The so-called neoclassical transport theory, considering the toroidicity of the configuration thus was developed.
Neoclassical transport is a theory describing the transport process due to Coulomb collisions in quiescent state, considering the field inhomogeneity of field lines induced by the toroidicity of the configuration. Compared with classical transport theory, it considers the complex geometry of the magnetic field, which gives rise to more complex particle orbits and drifts than the gyration motion of charged particles. Here we introduce the main particle drifts induced by the toroidicity in toroidal magnetic configurations developed within the framework of neoclassical transport theory. First of all, applying Ampère's law:

$$\nabla \times \boldsymbol{B} = \mu_0 \boldsymbol{J} \tag{2.1}$$

We have the toroidal magnetic field:

$$B_\phi = \mu_0 I/(2\pi R) \tag{2.2}$$

Where $\boldsymbol{J}$ is the current density, I is the total current in the toroidal magnetic coils and R is the radial coordinate originated in the toroidal center. The toroidal component of the magnetic field is the dominant one in tokamaks and it is inversely proportional to the radius R. This $1/R$ dependence leads to a particle drift induced by the gradient of the magnetic field:

$$\boldsymbol{v}_g = \frac{\mu}{q}\frac{\boldsymbol{B} \times \nabla \boldsymbol{B}}{\boldsymbol{B}^2} \tag{2.3}$$

Besides the gradient drift, there is another particle drift caused by the curvature of field lines and it is named curvature drift. When a particle moves along a curved path, there is a centrifugal force, which in turn generates this particle drift in a magnetic field. The curvature drift velocity is defined as:

$$\boldsymbol{v}_c = m\boldsymbol{v}_{\parallel}^2(\boldsymbol{B} \times (\boldsymbol{B} \times \nabla)\boldsymbol{B})/qB^4 \tag{2.4}$$

The two mentioned particle drifts depend on the sign of the charge q that particles carry. Consequently, it leads to a charge separation and a local vertical electric field thus appears. With the presence of the local electric field, another particle drift motion, deducted from momentum equation easily, will occur:

$$\boldsymbol{v}_E = (\boldsymbol{E} \times \boldsymbol{B})\,/B^2 \tag{2.5}$$

This drift motion is directed outwards, and it could lead to serious degradation of plasma confinement. This is the reason for introducing the rotational transform into toroidal configurations. With the rotational transform, the $\boldsymbol{E} \times \boldsymbol{B}$ drifts, being the consequence of the ∇B drifts, can be compensated. However, the particle motion still suffers the ∇B drift, which leads to a change of the particle trajectory.
The $1/R$ dependence of the magnetic field also leads to the effect called "magnetic mirror". The moduli of the perpendicular and parallel velocity vary as the change of magnetic field:

$$v_\perp = (2B\mu/m)^{1/2} \qquad v_\parallel = \left[(2W - mv_\perp^2)/m\right]^{1/2} \tag{2.6}$$

Where W is the total energy and the electric field is neglected. Thus the kinetic energy and the magnetic momentum are conserved. This variation of the two velocity components is due to the energy exchange between the parallel and perpendicular kinetic energy of a charge particle and consequently, certain particles could reach a point where the parallel velocity vanishes at high field side and 'bounce' back to the low field side. Now let us consider a charged particle origins in point 1 and it's guiding center trajectory is moving to high field side, as shown in Figure 2.1 which is a poloidal cross-section of a tokamak configuration. The flux surfaces are the dashed concentric circles. The ∇B drift is upwards with such magnetic configurations. Thus, the particles drifts off the original flux surfaces (1→2→3). At point 3, the whole parallel kinetic energy is converted to the perpendicular kinetic energy, considering the conservation of both the magnetic momentum and the kinetic energy (neglect the electric field). So the particle is 'reflected' by the so-called magnetic mirror effect. It starts to move back, but is still pushed towards exterior surfaces by the ∇B drifts (3→4→5). As it arrives as point 5, it is displaced outward by a certain amount,

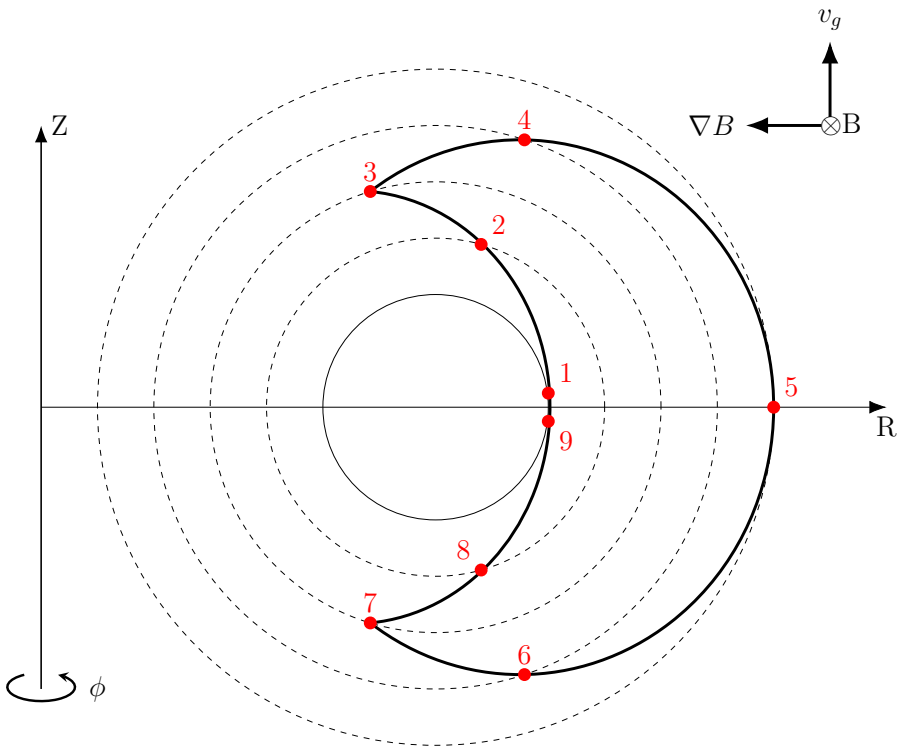

Figure 2.1: A sketch of banana orbit on the poloidal projection in a tokamak configuration. The concentric circles indicates the flux surfaces neglecting the Shafranov shift. The ∇B drift is upwards in such a configuration. For simplicity reason, the flux surfaces are drawn as concentric circles, without including the Shafranov shift.

compared to its initial position. As it goes on moving in the lower section of the torus, the vertical drift brings it to more and more interior surfaces (5→6→7). At point 7, the particle suffers again a reflection and starts moving back, passing again through more and more interior surfaces (7→8→9) until the curve closes on itself. Such a particle is trapped: it never enters the central region of strong magnetic field. Because of its shape, the orbit of a trapped particle in a tokamak is called "banana orbit". Particles with trajectories within this banana orbit are called trapped particles and particles who can explore the whole plasma volume, i.e., the poloidal cross-section of their trajectories are complete circles are named passing particles. The frequency for trapped particles to complete the banana orbit is called bounce frequency and it is defined as:

$$\omega_b = v/(Rq) \tag{2.7}$$

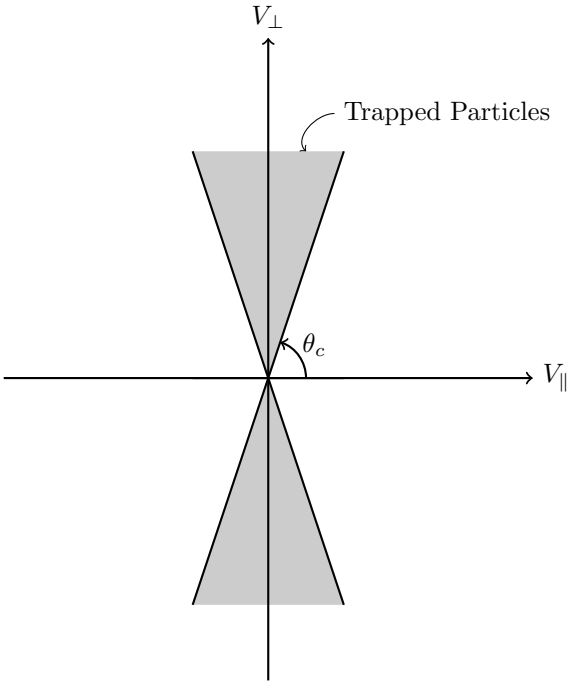

Figure 2.2: Velocity space showing the trapped-passing boundary. The critical angle θ_c defines the so-called loss cone which is the white space.

The boundary between trapped and passing particles is shown in velocity phase space in Figure 2.2. The gray shadow is the trapped region and the white region is the passing region. The boundary between trapped particles and passing particles is characterized by the angle θ_c. The fraction f of the trapped particles is $f = \cos\theta_c \approx a/R_0 = \epsilon$. Here ϵ is the inverse aspect ratio defined as the ratio between minor radius a and major radius R_0. There is another parameter, namely '*pitch parameter*' (k^2) which also defines the trapped and passing particle regions:

$$k^2 = v_\perp^2/v_\parallel^2 \tag{2.8}$$

Clearly, $k^2 < 1$ defines trapped region and $k^2 > 1$ defines the passing region. In particular, $k^2 \sim 1$ defines the region around trapping-detrapping region where trapped particles and passing particles are exchanged due to collision.
The banana orbit described above is caused by the poloidal non-uniformity of magnetic field in toroidal configurations due to toroidal symmetry. Note that the Figure

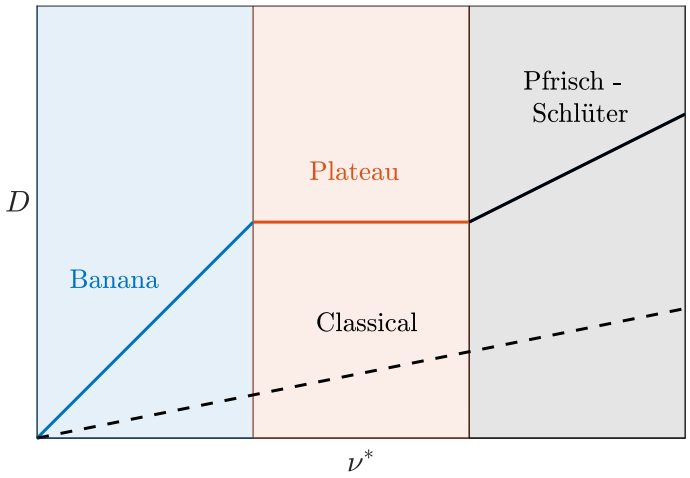

Figure 2.3: Diffusion coefficient D is plotted in log-log scale, as a function of collisionality ν^*. The solid line represents the neoclassical transport and the dashed line represents the classical transport. This plot is valid in magnetic configurations with toroidal symmetry. It starts with banana region, in which the collision frequency is lower than bounce frequency. Particles within this region are trapped inside of the banana orbit. The plateau regime is a constant line which does not depend on the collisionality and finally the Pfrisch-Schlüter regime is the high collisionality regime.

2.2 shows a situation with no density gradient, i.e., the trapped particles between two neighboring banana orbits are equal. However, in magnetically confined configurations, there exists the density gradient, which leads to the unbalance of trapped particles between adjacent banana orbits. This will lead to momentum transfer between trapped particles and passing particles and consequently a net toroidal current is formed and this is the so-called bootstrap current. In advanced tokamak scenario, the bootstrap current could take a significantly part of the whole toroidal plasma current.
Until now we defined three single particle drifts and its guiding center trajectory. The total drift velocity can be written as:

$$\boldsymbol{v}_d = \boldsymbol{v}_E + \boldsymbol{v}_g + \boldsymbol{v}_c \tag{2.9}$$

In fusion plasmas, the collective behavior of many charged particles must be taken into account. Transport processes are the macroscopic result of the interactions among charged particles in an electromagnetic field. The macroscopic thermodynamic quantities like density, temperature, etc. can be deduced from the particle

distribution function $f(\boldsymbol{r}, \boldsymbol{v}, t)$, by taking different velocity moments. Consequently the particle drifts enter into the flux function by definition: $\Gamma_p = \int d\boldsymbol{v} f(\boldsymbol{r}, \boldsymbol{v}, t)\boldsymbol{v}_d n$ with Γ_p the particle flux and n the density. The time evolution of flux function (particle or energy flux) is:

$$\partial \mathcal{A}/\partial t = -\nabla \cdot (\Gamma) + \mathcal{S} \tag{2.10}$$

Where $\mathcal{A}$ is particle density (particle transport) or energy density (energy transport), $\Gamma = -D\nabla\mathcal{A}$ is the particle or energy flux with D the diffusion coefficient, and $\mathcal{S}$ is the source or sink. Note here the non compressive assumption as well as stationary condition are taken ($\nabla \cdot (\boldsymbol{v}\mathcal{A}) = 0$). For a tokamak case, a sketch of diffusion coefficient D versus the normalized collision frequency $\nu^* = \nu/\omega_b$ with ω_b the bounce frequency, is presented in Figure 2.3. There are three separated regions depending on different collision frequency regimes, being banana region (blue line), plateau region (red line) and Pfirsch-Schlüter region (black line). The classical transport diffusivity, which is much lower than one from neoclassical transport theory, is also plotted (dashed black line) for comparison. Trapped particles (banana orbits in tokamaks) dominate the transport process at low collisionality regimes, where $\nu^* \leqslant 1$ and this region is called *low collisionality* region. Particles in this region complete many banana orbits before they collide with each other. The high collisionality regime is called Pfirsch-Schlüter regime. This regime is connected to the banana regime by the so-called *plateau* regime in which there is no dependence on the collision frequency. For the neoclassical transport in stellarator configurations, things are more complex because there is no toroidal symmetry in stellarators and thus there is no banana orbits in such configurations. Indeed, the guiding center trajectories of particles are non-closed 'banana orbits' and this leads to a much higher transport coefficient in stellarators than ones in tokamaks. Moreover, there are many local magnetic wells in stellarators, in which particles are trapped either in the high or low field side. These particles cannot 'feel' the compensation effect from the rotational transform introduced to compensate the $\boldsymbol{E} \times \boldsymbol{B}$ drifts. Hence, these particles are lost from the plasma.

2.2 Stochastic Transport

In RFP plasmas, many MHD tearing modes resonating at the same time, nested flux surfaces no longer exist due to overlapping of many magnetic islands. Thus, the transport in RFPs is dominated by stochastic transport. Here a brief description of the stochastic transport theory, considering *collisionless* plasmas, developed by

Rechester and Rosembluth [58] is presented. The model describes the parallel transport in plasmas with destroyed magnetic surfaces due to many resonating modes. First of all, in cylindrical geometry, the magnetic field can be written as $\boldsymbol{B} = \boldsymbol{B}_z + \boldsymbol{B}_\theta + \delta\boldsymbol{B}$, with the perturbation part:

$$\delta\boldsymbol{B} = \sum_{m,n} \boldsymbol{b}_{m,n}(r) \exp[i(m\theta - nz/R)] \tag{2.11}$$

m and n are the wave numbers in poloidal and toroidal direction, respectively. Each harmonic defines the resonance surface, which is the possible location for tearing modes to develop. When many modes resonate at the same time, magnetic surfaces conserve if the Poincaré plot on a poloidal cross-section shows smooth curves. Consider a small area with radius of r_0 in a plane z = const and map it by solving the two equations $dr/dz = B_r/B_z$, $rd\theta/dz = B_\theta/B_z$. This magnetic mapping is area preserving, as a consequence of $\nabla \cdot \boldsymbol{B} = 0$. There are two possible evolutions of this process. The first one is that the circle will move as a whole and the second one is that it will deform its shape stretching in one direction and contracting in the other. An analytical expression for continuous mapping is:

$$l(z) = l_0 \exp(z/L_c) \tag{2.12}$$

Where L_c is the correlation length with its one possible expression $L_c = \pi R/\ln(\pi s/2)$. This solution is obtained when the poloidal mode number m is fixed. in the case with many m and n modes, this value is expected to be smaller [58]. Here s is the so-called stochasticity parameter defined as:

$$s = \frac{1}{2}\left(\Delta_{m,n} + \Delta_{m',n'}\right)/|r_{m,n} - r_{m',n'}| \tag{2.13}$$

Where m, n and m', n' represent any two harmonics which have neighboring rational surfaces, $\Delta_{m,n}$ and $\Delta_{m',n'}$ represent the separatrix width of the corresponding magnetic islands and $r_{m,n} - r_{m',n'}$ represents the distance between these two magnetic islands. It is clear to see that the overlapping of neighboring magnetic islands occurs when $s > 1$. Such behavior mentioned above is called stochastic instability of trajectories. The width of the area δ will exponentially decrease in order to conserve the total area: $\delta(z) = r_0 \exp(-z/L_c)$. This evolution process is shown in Figure 2.4. It is clear to see that in a configuration with many tearing modes resonating at the same time, the simply area (one circle) will evolve into a very complex shape. Note that this process is strictly area preserving. The average squared radial displacement of the ares can be described as:

$$\left\langle (\delta r)^2 \right\rangle = 2LD_{st} \tag{2.14}$$

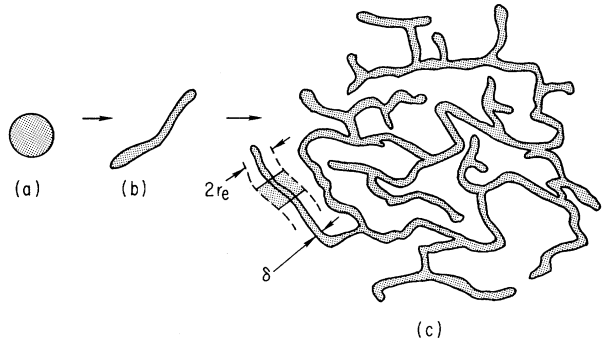

Figure 2.4: A sketch of area mapping in multiple modes resonating magnetic field.

L is the distance in the z direction with $L \gg L_{c0} = L_c \ln(rmr_0)$. D_{st} is given:

$$D_{st}(r) = \pi R \sum_{m,n} \frac{|b_{m,n}(r)|^2}{B_z^2} \delta \left(\frac{m}{q(r)} - n \right) \tag{2.15}$$

Where $b_{m,n}(r)$ is the mode amplitude. The function $q(r)$ is the safety factor which is defined in Equation 1.10.
Now consider the time evolution of electrons in a small region. Being a Brownian process, the radial spreading process has its thermal conductivity as $\chi_r = \langle (\Delta r)^2 \rangle / 2\tau$ with τ the time interval and Δr the radial displacement within this time interval. This is equivalent to the *collisionless* condition, which brings us the thermal conductivity in radial direction:

$$\chi_r = \left\langle (\Delta r)^2 \right\rangle / 2\tau = 2LD_{st}/2\tau = D_{st} v \tag{2.16}$$

The thermal conductivity in a stochastic field is proportional to the ion thermal velocity $v = (2T_i/m_i)$ instead of the collision frequency. Also it is proportional to the sum of the squared amplitudes of all the modes, which is shown in the expression of $D_{st}(r)$ above. The physics meaning of this definition is that the stochasticity produced in such a configuration has contributions from all the tearing modes. The stochastic transport in RFPs is the dominant transport process due to the overlap of resonant modes. This mechanism will be discussed in the study of thermal properties in Quasi-Single Helicity state on RFX-mod, presented in Chapter 4.

2.3 Three Dimensional Transport due to the Presence of Magnetic Islands

Transport theory deals with the losses of particle and energy in fusion plasmas and it is strongly related to the confinement properties. Field inhomogeneity is the fundamental reason responsible for particle and energy loss in toroidal configurations. The transport study is commonly simplified to 1.5 dimensional to reduce the complexity and time consuming of the numerical simulations. Here 1.5 dimensional means quantities averaged over the magnetic flux surfaces. The particle and energy loss, depending on different toroidal configurations, could be induced by either parallel or perpendicular transport process:

- In tokamaks and stellarators who possess nested flux surfaces, the losses are mainly caused by perpendicular transport process across the flux surfaces. Experimentally the kinetic quantities have been observed that they could be considered as the functions of flux surfaces. Temperature and density on one flux surfaces can be considered constant due to very high parallel velocities. In real magnetic configurations, however, the resonant MHD tearing modes rise intrinsically three dimensional aspect in the transport study. In tokamaks and stellarators, nested flux surfaces are distorted in vicinity of magnetic islands and the toroidal symmetry is thus broken.

- In RFP discharges, it is the dynamo mechanism that sustains the configuration by the non-linear interactions among many resonating tearing modes. This leads to an obvious consequence: the magnetic flux surfaces are broken and reconnected and the transport is intrinsically three dimensional, being dominated by stochastic transport. This is true especially in Multiple Helicity state, where all the modes have comparable amplitudes. In such state, the flux surfaces are believed to be broken and the particle and energy losses are mainly caused by the parallel transport process along the field lines. However, when it comes to Quasi-Single Helicity (QSH) state where one single mode dominates the mode spectrum, a special region, featuring bean-shaped flux surfaces has been identified. In such region, steep thermal gradients develop and the kinetic quantities like temperature, density could be treated as function of the flux surfaces. Consequently, it is believed that in such region, the flux surfaces are nearly conserved [59, 60]. The transport study on RFX-mod in this dissertation focuses on the region with steep thermal gradients, with the assumption that the magnetic field consists the equilibrium magnetic field and *only* the dominant mode. With this assumption, a helical symmetry could be

defined in QSH plasmas and hence the transport study could be performed on 1.5 dimensional level by taking into account the flux surface averaged kinetic quantities.

Facing the three dimensional transport issues rising from the fusion research community, this dissertation is dedicated to the three dimensional transport study induced by the presence of magnetic islands, on 1.5 dimensional level. The main difficulties to perform 1.5 dimensional transport analysis are:

- In RFP plasmas, the dominant mode usually forms into a big island so that in such configurations, multiple magnetic axes exist at the same time. Consequently, no monotonic radial coordinate could be defined to describe the whole plasma volume.
- The distorted flux surfaces break the toroidal symmetry in tokamaks, leading to non-closed banana orbit of trapped particles and thus, particles are lost via drifting outwards. In stellarators, such process is more serious since even without the presence of the magnetic islands, the particle trajectories are not closed banana orbits due to lack of toroidal symmetry. Hence, the magnetic islands will introduce an enhanced particle flux in stellarator configurations compared with tokamak configurations. This effect is essentially induced by the increase of toroidal viscosity and the consequence is that it increases the radial particle drifts.

In this dissertation, possible solutions for these two issues are presented:

- First of all, a solution named Multiple Domain Scheme (MDS) is adopted, which was proposed by F. Porcelli [61] to overcome the the multiple axes issue. A corresponding new transport code, named Multiple Axes Solver (MAxS) has also been developed and benchmarked. This work has been carried out on RFX-mod and detailed *original* work are presented in Chapter 3.
  Besides, the application of MDS and MAxS has been done for the study of three sub-states of Quasi-Single Helicity state, a RFP plasma regime observed in all RFPs all over the world [60, 62]. The comparison on thermal properties among these three sub-states as well as the energy transport study has been firstly completed. The energy confinement time, using an improved method has also been firstly evaluated. The physics behind the observed phenomenon is discussed within the framework of stochastic transport. The detailed *original* work is presented in Chapter 4.
  The work carried in this part has been presented/published in:

  - *Y. Zhang, F. Auriemma, A. Fassina, D. Lopez-Bruna, R. Lorenzini, E. Martines, B. Momo, F. Sattin and D. Terranova, Multiple domain scheme for heat transport analysis in plasmas with magnetic islands: a first study, 42th EPS conference.*
  - *F. Auriemma, D. Lopez-Bruna, R. Lorenzini , B. Momo, Y. Narushima, I. Predebon, F. Sattin , Y. Suzuki, D. Terranova, Y. Zhang, A novel approach to the study of transport properties in plasma with magnetic islands, to be submitted.*
  - *Y. Zhang, F. Auriemma, A. Fassina, R. Lorenzini, D. Terranova, B. Momo, and E. Martines, Thermal Properties of 3 sub-states of Quasi-Single Helicity state on RFX-mod, Physics of Plasmas, under review.*

- As for the second issue, the solution is to study the enhanced toroidal viscosity induced by the presence of magnetic islands in tokamaks. The theory is developed by K. C. Shaing [63], which reveals the appearance of non-ambipolar particle fluxes in vicinity of magnetic islands induced by the enhanced toroidal viscosity. A brief description of this theory is presented in Chapter 5.
  The application of this theory has been performed on TJ-II stellarator where it has been reported that magnetic islands plays a role of transport barrier [64] and also it modifies the local electric field [65]. A moderate modification on the original theory has been made in order to apply it to TJ-II configurations, considering much higher particle fluxes in stellarators compared with ones in tokamaks. The transport simulations have been performed in TJ-II plasmas, adopting the modified equations. The detailed *original* work is presented in Chapter 6.
  The work carried out in this part has been presented in:

  - *B. Momo, D. López-Bruna, Y. Zhang, F. Auriemma, R. Lorenzini, Island-induced electric field modification: the TJ-II case, Theory of fusion plasmas, joint Varenna-Lausanne international workshop.*

Part II

Thermal Properties and Transport Study on Three Sub-states in QSH

3 Quasi-Single Helicity and Multiple Domain Scheme

Quasi-Single Helicity state has been observed on RFX-mod firstly and confirmed by other RFP devices afterwards. It shows better confinement properties compared with Multiple Helicity state. This chapter presents the description of QSH state as well as its three sub-states. Moreover, this chapter reviews the development of a tool for transport study in Multiple magnetic AxeS configurations, named MAxS, based on the concept of Multiple Domain Scheme.

3.1 Multiple Helicity and Quasi-Single Helicity

In RFX-mod discharges, due to unique safety factor profile $q < 1$, many MHD tearing modes saturate intrinsically, producing superposition of many magnetic islands and giving rise to a chaotic magnetic field in the plasma core. When the plasma current is low ($I_p < 1$MA), these MHD modes have comparable amplitudes and this is named Multiple Helicity (MH) state. Such chaotic magnetic field leads to high transport in the center with very limited confinement properties. Indeed, the electron temperature in such states shows a flat, poloidally symmetric profile. On the other hand, it is the nonlinear interactions among these modes that sustains the RFP configurations. This is the dynamo mechanism presented in Chapter 1. Compared with other fusion devices like tokamaks, RPFs in MH states are far behind due to the bad plasma confinement properties.

Nevertheless, it has been theoretically predicated with 3-dimensional MHD simulations [66, 67] that one single helical mode could sustain the dynamo mechanism and this state is named Single Helicity state (SH). SH state shows a promising future for RFPs in fusion research since nested helical flux surfaces are preserved and radial transport could be significantly reduced compared with MH state. Experimentally, however, SH state has never been observed while an intermediate state between MH and SH state, with enhanced plasma confinement properties, has been observed in RFX-mod and has been confirmed on all other RFP devices [62, 68, 69] with different experimental conditions. Besides RFX-mod, there are mainly three RFP devices under operations, being EXTRAP T2R [70], MST [71] and RELAX [72]. Also other experiments can be considered such as TPE-RX [73], which has been shut down since

Devices	R/a(m)	Plasma Current/Designed Plasma Current (kA)
EXTRAP T2P	1.24/0.183	<500/1000
RFX-mod	1.995/0.459	2000/2000
TPE-RX	1.72/0.45	500/1000
RELAX	0.5/0.25	50/100
MST	1.5/0.52	500/600
KTX	1/4/0.4	NULL/1000

Table 3.1: The main characteristics of six RFP devices.

many years and KTX that started operation recently in USTC, Hefei, China [74]. The main characteristics of these six devices are listed in Table 3.1. EXTRAP T2P is a medium RFP device located at the Royal Institute of Technology in Stockholm. The active control of plasma instabilities is applied through the intelligent shell IS operation [75, 76, 77]. The dominant mode in EXTRAP T2R is different from the one in RFX-mod and it could also vary during the discharge [78]. This dynamics can be ascribed to a change in the magnetic equilibrium and hence in the safety factor profile. MST is a large RFP device located in Madison, USA. Both RFX-mod and EXTRAP T2P have active control on radial perturbations while in MST, the suppression of radial perturbations is done by the thick shell. The dominant mode is usually the innermost one, which is strongly affected by the aspect ratio. Nevertheless, the dominant mode can vary depending on different experimental conditions. In RFX-mod, with relatively constant experimental conditions, the dominant mode is the innermost one, being m=1, n=-7. In RELAX, the dominant mode is m=1, n=4 [79] and in MST, the dominant mode is usually m=1, n=5:6 [68, 80]. In EXTRAP T2R, due to large aspect ratio and different experimental conditions, the dominant mode varies among m=1, n=11:13.

The QSH state is an enhanced RFP plasma regime which appears periodically or lasting during the whole discharge in the high plasma current discharges ($I_P > 1MA$ in RFX-mod). In RFX-mod, it is obtained with active control of radial magnetic perturbations [27, 60]. A typical discharge with $I_P > 1MA$ in RFX-mod is shown in Figure 3.1. The upper graph is the time evolution of the plasma density (a), the plasma current (b) and the lower one is the time evolution of the toroidal magnetic tearing mode spectrum in which the red line represents the m=1, n=-7 mode, whose amplitude dominates the spectrum periodically during the discharge and the blue line represents the rest of the modes (secondary modes) defined as their combined

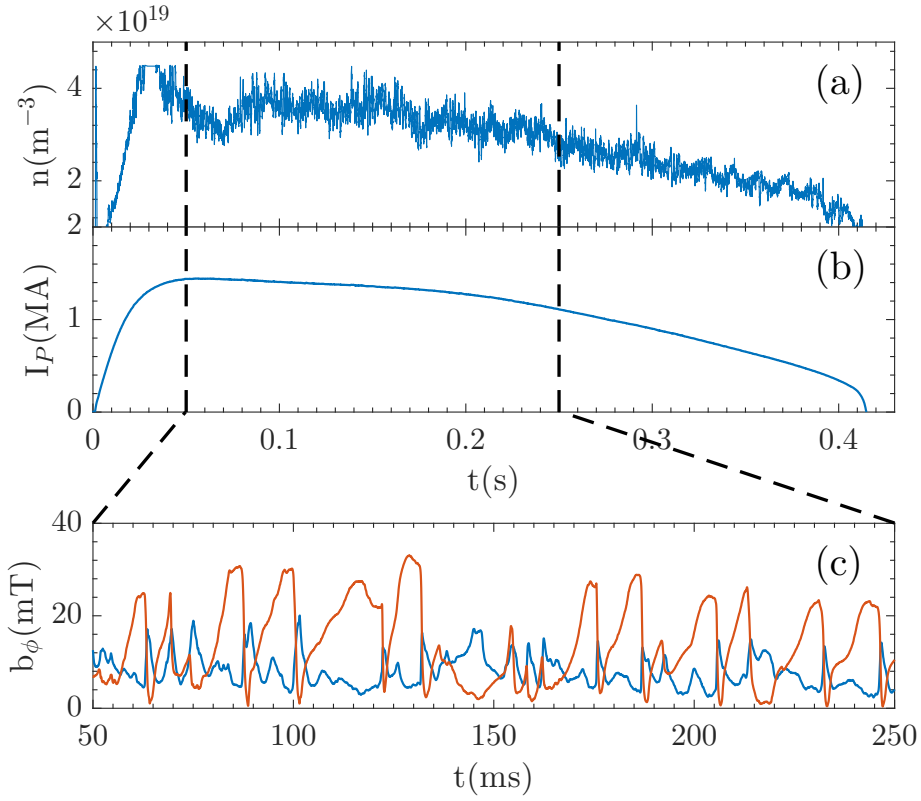

Figure 3.1: A typical discharge in RFX-mod. (a): plasma density n. (b): plasma current I_p. (c): The time evolution of toroidal magnetic component b_ϕ with red line representing the dominant mode (m=1,n=-7) and the blue line representing the secondary modes (m=1, n=-8:-17).

amplitudes:

$$b_{sec} = \left[\sum_{n=-8}^{-17} (b_\phi^{1,n})^2 \right]^{1/2} \tag{3.1}$$

In this dissertation the toroidal mode number n=-8:-17 is adopted to compute the amplitude of the secondary modes. The dominant mode amplitude shows a periodical growth and crash evolution process. When the dominant mode grows to high amplitude, QSH state appears and when its amplitude crashes to the same level as the secondary modes, MH state appears. The QSH is quantitively defined through

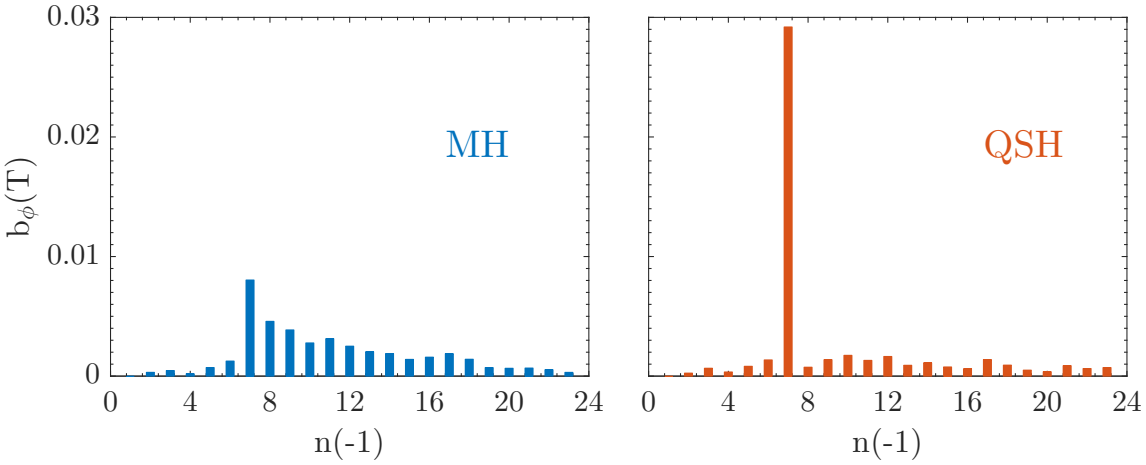

Figure 3.2: Typical toroidal field b_ϕ spectra (2ms averaged value) for m=1 mode against the toroidal mode number n. The blue spectrum is for MH state and the red one is for QSH state.

the so-called Ns spectral index:

$$Ns = \left\{ \sum_{j=n1}^{n2} \left[\left(b_\phi^{m,j}\right)^2 \Big/ \sum_{k=n1}^{n2} \left(b_\phi^{m,n}\right)^2 \right]^2 \right\}^{-1} \tag{3.2}$$

The value of Ns becomes 1 when the pure SH state is realized and increases when other modes grow. The duration time of one cycle has been found to increases with the increase of the plasma current [81]. A typical mode spectrum of both QSH and MH is presented in Figure 3.2. This mode spectrum is obtained by taking the average value of the mode amplitude over a time interval of 2ms. One could see that the modes show a comparable amplitude in MH while in QSH, there is a single mode dominating the spectrum.

Besides the magnetic field features mentioned above, QSH state has also been identified to have thermal structure: a helical thermal structure with high electron temperature is formed in the plasma center. This has been observed with soft X-ray tomographic reconstruction, on RFX-mod [82], EXTRAP T2R [83] and MST [84]. Moreover, on RFX-mod, electron temperature profiles along the equatorial plane has been measured, thanks to the high spacial resolution of the Thomson scattering diagnostic. The measured T_e profile shows that in MH state, the profile is a flat, poloidally symmetric one, indicating high stochastic transport in the whole plasma volume. On the other hand, when it comes to QSH state, a different profile, with

a high electron temperature structure in the center has been identified. The high T_e structure is sustained by steep thermal gradients, which are denoted as electron Internal Thermal Barrier (eITB). What is more, two types of thermal structure profiles in QSH has been also identified: One is with a narrow high T_e thermal structure and the other one with a wide T_e thermal structure. These two thermal structures, together with the different magnetic structures, can be actually further categorized into three sub-states. A detailed description on these three sub-states is presented in the following section.

3.2 Three Sub-States in QSH state

Further study on QSH state shows that there may be up to three sub-states in one cycle of QSH. These three sub-states feature different magnetic topologies as well as different width of thermal structures. Here a description of these three sub-states is presented using the experimental observations obtained in RFX-mod.
One cycle of QSH begins with the innermost mode starting to grow, while the rest of the modes decrease at low amplitudes. The dominant mode forms one big magnetic island with a separatrix. A bean-shaped thermal structure with narrow, off-axis electron temperature structure spontaneously forms inside the island. This is the first stage of QSH and it is named Double Axes state (DAx) since there are two magnetic axes existing at the same time. Afterwards, the dominant mode grows further, reaching the threshold on which a magnetic topological transition takes place: the X point of the dominant mode anneals with the original magnetic axis and the O point of the dominant mode survives as the new magnetic axis. During this process, the bean-shaped thermal structure remains relatively unchanged: narrow and off-axis. This is the second stage and it is named Single Helical Axis state (SHAx_n) with the subscript n indicating narrow thermal structures. When the dominant mode grows up to 4% of the edge magnetic field, the high electron temperature structure usually evolves from off-axis in SHAx_n into a wider profile enclosing the geometrical axis. This is the third stage of QSH and it is named SHAX_w state with the subscript w indicating wide thermal structures. Thus, QSH can manifest itself in these three different sub-states. The three sub-states of QSH are shown in Figure 3.3. The lower three figures d, e, f, are electron temperature profiles measured with an 84-point Thomson scattering diagnostic. The upper three figures a, b, c, are the corresponding T_e contour plots, calculated with the magnetic equilibrium reconstruction produced by the code SHEq [85], thanks to the fact that temperature, in QSH states, is observed to be a helical flux function [60]. Both DAx and SHAx_n feature narrow and off-axis T_e thermal structures. The SHAx_w, on the other hand, has a

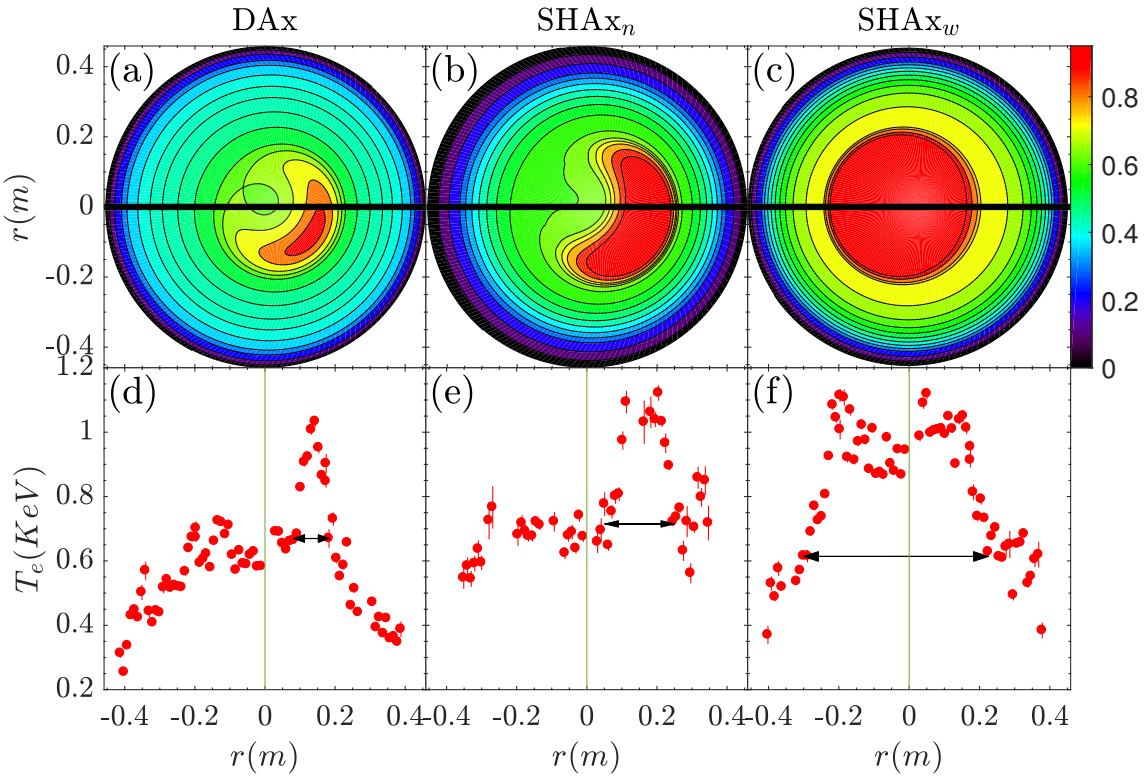

Figure 3.3: Three sub-states: (a) DAx, (b) SHAx$_n$ and (c) SHAX$_w$ are presented. The black horizontal lines in the contour plots represents the Thomson scattering laser path and ones in the lower 3 plots are the width of the thermal structure.

wide thermal structure in the plasma core.

The three sub-states within one cycle of QSH state have different magnetic topologies as well as different thermal structures, leading to an interesting topic on the understanding the evolution of the energy transport properties. Motivated by such observations, the work on RFX-mod has been carried out on the topic of transport study within these three sub-states. The main idea is to assume the magnetic field in QSH is a pure SH state and the physical meaning of this assumption is to neglect all the secondary modes. In such a way, a helical symmetry can be defined in QSH state and also the flux surfaces. However, difficulties appear when it comes to DAx state, which has two magnetic axes. In such magnetic configurations, it is impossible to define a monotonic radial coordinate to perform transport analysis. Facing this problem, a possible solution, named Multiple Domain Scheme, together with a

transport solver have been studied and developed. The detailed work is presented in the following section.

3.3 Multiple Domain Scheme and Multiple Axes Solver

Transport research benefits of the availability of several well-developed 1.5D transport codes, which have been widely used in single axis magnetic configuration for decades. However, it is beyond their capability to treat situations with the presence of magnetic islands due to the fact that it is impossible to find a monotonic radial coordinate that can describe the whole plasma volume. Indeed, in plasma configurations with multiple axes, a monotonic radial coordinate is undefinable in the whole plasma volume, which, together with the correct metrics (the spatial derivative of the volume and the first element of the metric tensor, denoted as V' and G_1, respectively), are essential to solve the energy transport equation, averaged over the magnetic surfaces:

$$\frac{3}{2}n_e\frac{\partial T_e}{\partial t}+\frac{1}{V'}\frac{\partial \Gamma_h}{\partial \rho}=S_e \tag{3.3}$$

Where n_e and T_e are the electron density and temperature, $\Gamma_h=-V'G_1n_e\chi\partial T_e/\partial\rho$ is the energy flux. In this dissertation, Γ_h indicates the heat flux and Γ_p indicates the particle flux. χ is the thermal diffusivity and S_e is the energy source or sink. ρ is the radial coordinate and it could have several different definitions. Here one of the definitions is adopted, which is defined as[1] :

$$\rho=(V_\rho/2\pi^2R_0)^{1/2} \tag{3.4}$$

With V_ρ the helical volume enclosed by each flux surface labeled by ρ and R_0 being the major radius of the device.
Facing this issue, a new scheme, named Multiple Domain Scheme (MDS) has been studied. The idea of MDS has firstly been reported by F. Porcelli in Reference [61]. The main principle is to divide the total plasma volume into three separated regions. Figure 3.4 shows a sketch of a poloidal cross-section of a magnetic field with the presence of a magnetic island. The 3 regions are: Region I, the circular plasma containing the original magnetic axis; Region II, the magnetic island containing its own axis and Region III, the outer region in the plasma edge. The red line represents

[1]This definition is also adopted by code SHEq which produces the surfaces averaged T_e profiles based on this definition of the radial coordinate ρ.

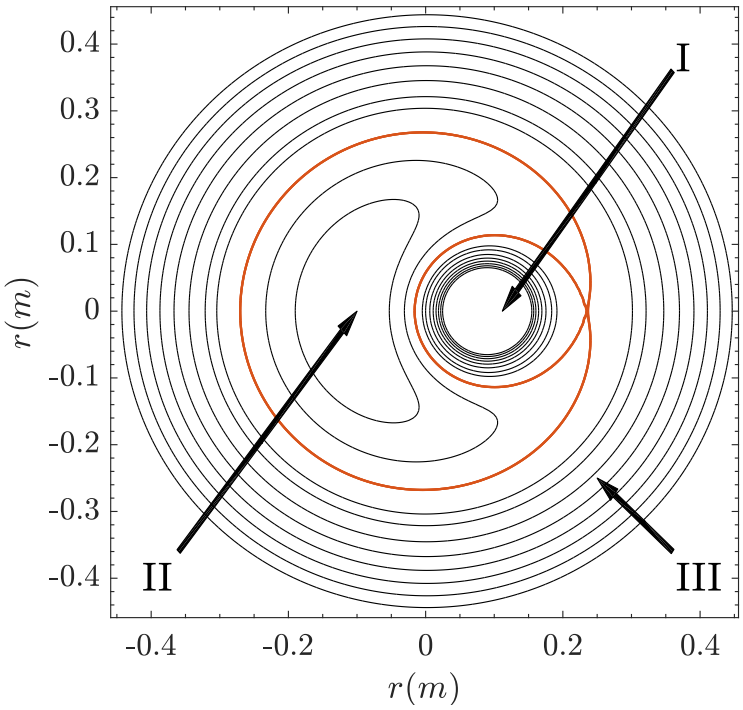

Figure 3.4: A sketch of poloidal cross-section of a magnetic field with the presence of a magnetic island is presented. The total plasma volume is divided into three separated regions: Region I is the circular plasma with the original magnetic axis; Region II is the magnetic island with its own axis and Region III is the outer region. The separatrix is the red line and it is the interface among these three regions.

the separatrix, which is a thin layer around the magnetic island and it features high stochasticity. In each of the 3 zones, a monotonic coordinate ρ could be well defined and the temperature could also be considered as a function of ρ in each zone, which will be demonstrated later. The separatrix region is the interface among these three zones and it has a very small volume compared with the three zones. Hence, in the separatrix region, it is assumed that there is no heat source nor sink. What is more, due to the high parallel transport in the separatrix, the electron temperature is uniform everywhere in the separatrix. The boundary conditions for solving Equation 3.3 is listed as below:

Zone I: On the magnetic axis: $\partial T_e/\partial\rho|_{\rho=0} = 0$; at the separatrix: $T_e|_{\rho=\rho_{sep}} = T_{sep}$.

Zone II: On the island O-point: $\partial T_e/\partial\rho = 0$; at the separatrix: $T_e|_{\rho=\rho_{sep}} = T_{sep}$.

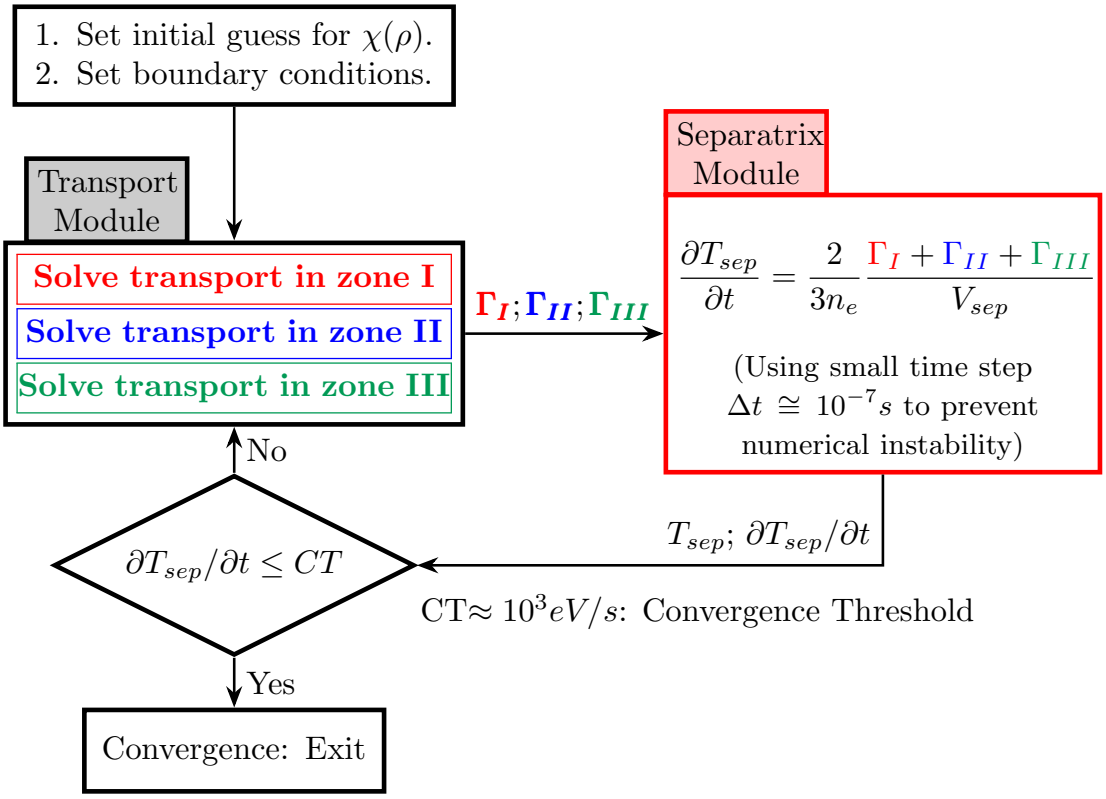

Figure 3.5: Flow chart of code MAxS.

Zone III: At the separatrix: $T_e|_{\rho=\rho_{sep}} = T_{sep}$.; at the plasma edge: $T_e|_{\rho=\rho_a} = T_a$.

Based on the concept of MDS, a corresponding new code, named Multiple Axes Solver (MAxS), able to study the transport process in both single and multiple magnetic axes configurations has been developed and tested on RFX-mod. The flow chart of MAxS code is presented in Figure 3.5 and the main steps are:

- Make initial 'guess' for thermal diffusivity χ in each zone and set the proper boundary conditions.
- Evolve transport equations in three zones until the temperature profiles remain unchanged. Then get the fluxes from the three zones, namely Γ_I, Γ_{II} and Γ_{III}.
- These fluxes enter into the separatrix region whose temperature T_{sep} evolves according to:

$$\partial T_{sep}/\partial t = (2/3n_e)[(\Gamma_I + \Gamma_{II} + \Gamma_{III})/V_{sep}] \tag{3.5}$$

Where V_{sep} is the volume of the separatrix. Note Equation 3.5 is derived from Equation 3.3, using the assumption of small volume. As mentioned before, with such assumption, the source term $S_e = 0$ and $\partial\Gamma/\partial V \approx \Delta\Gamma/\Delta V$.

- If $\partial T_{sep}/\partial t \leq 10^3 eV/s$ then the code stops. The final χ profiles are the ones we are seeking.
- If $\partial T_{sep}/\partial t > 10^3 eV/s$ then go back to step 2, adjusting the χ profile and repeating the following steps.

3.4 Electron Temperature Profile Remapping

To perform 1.5 dimensional transport study in these three sub-states, one needs to define the proper radial coordinate, the correct metrics and the remapped electron temperature over the flux surfaces. The radial coordinate, as well as the correct metrics have been described in the framework of MDS. This section presents the electron temperature remapped along a radial coordinate ρ. In this part, another possible definition of ρ is adopted, which is calculated as the square root of the normalized helical flux:

$$\rho = \sqrt{\Phi/\Phi_0} \tag{3.6}$$

Where Φ is the helical flux defined as $\Phi = m\Psi_0 - nF_0 + m\psi^{m,n} - nf^{m,n}$ with m=1, n=-7 the dominant poloidal and toroidal mode number, Ψ_0, F_0 are the equilibrium poloidal and toroidal magnetic flux [86]. The ψ, f are the poloidal and toroidal magnetic flux of the dominant mode. The definition of the helical flux function is essentially assuming a SH state in RFP plasmas. Φ_0 is the helical flux on the plasma edge [85]. Note that the suitable radial coordinate is arbitrary as long as it is well defined. In this section, the radial coordinate defined in Equation 3.6 is used.
The remapping of electron temperature over the flux surfaces in the poloidal directions is done under the assumption that the kinetic quantity, such as electron temperature, is a function of the helical flux in one axis condition. To illustrate the remapping process, a typical electron temperature profile, measured in SHAx_w state is presented in Figure 3.6(a), as a function of the radius r. There is one nearly flat region with high electron temperature in the core and on both sides of the flat region, there are two temperature gradients, marked as the gray shadow which are electron Internal Transport Barrier (eITB) regions. The T_e profile is split into two parts, marked as blue and red, by a vertical green line which corresponds to the minimum value of ρ. Using ρ as a new radial coordinate, the result of T_e remapping along ρ is shown in Figure 3.6(b) and it indicates the kinetic quantity T_e can be described as a

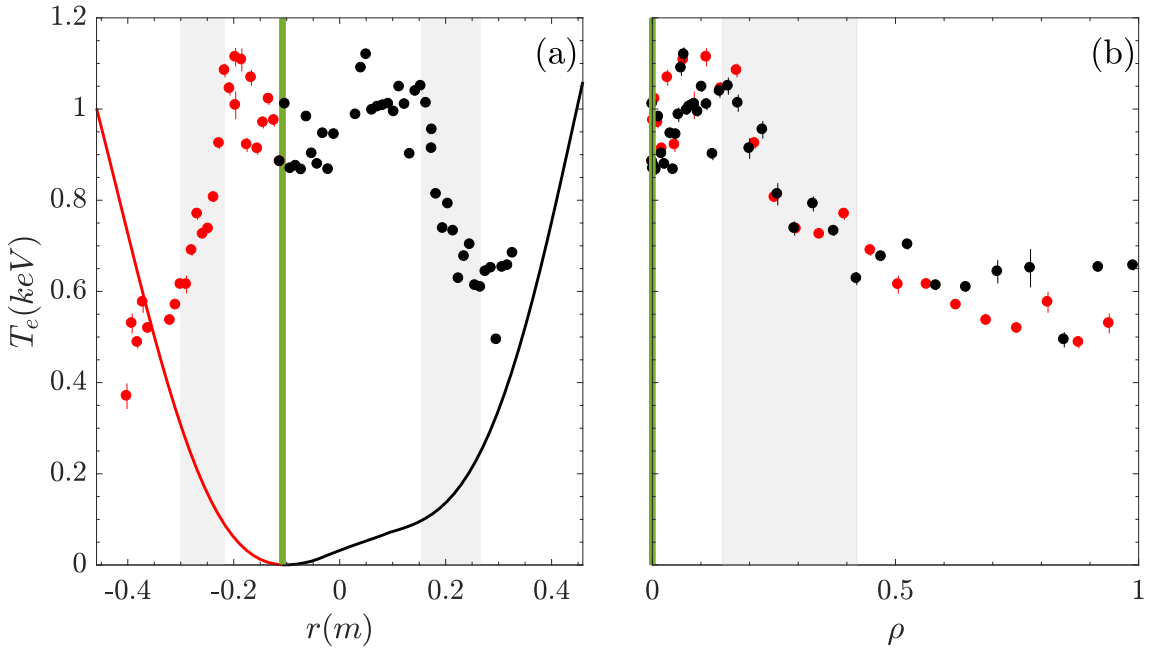

Figure 3.6: (a) Typical electron temperature in a $SHAx_w$ state as a function of the radius (dots). The solid line represents the normalized helical flux function ρ. (b) The same electron temperature profile as in (a), plotted as a function of ρ with the two colors representing the two sides with respect to ρ_{min}.

function of the normalized helical flux. The remapping is easy in single magnetic axis situation while for multiple axes cases, things could get bit complex but the main principle remains the same. Figure 3.7 shows a result of remapping done in a DAx case, in which both the core region and the island region are detected by Thomson scattering diagnostic. The detailed procedure and the panel of the Figure 3.7 of this remapping in DAx case is:

Panel (a) Contour plot of the helical flux at Thomson scattering toroidal angle, with the thick red curve representing the separatrix. There are four intersections between the separatrix and equatorial plane ($\theta = 0$) and their locations are marked with four dashed black vertical lines. The three vertical lines represent the location of maximum or minimum of the helical flux, red for magnetic island region and blue for the core region.

Panel (b) The normalized helical flux ρ is plotted versus the geometrical radius. There are two separated island regions detected by Thomson scattering, shown

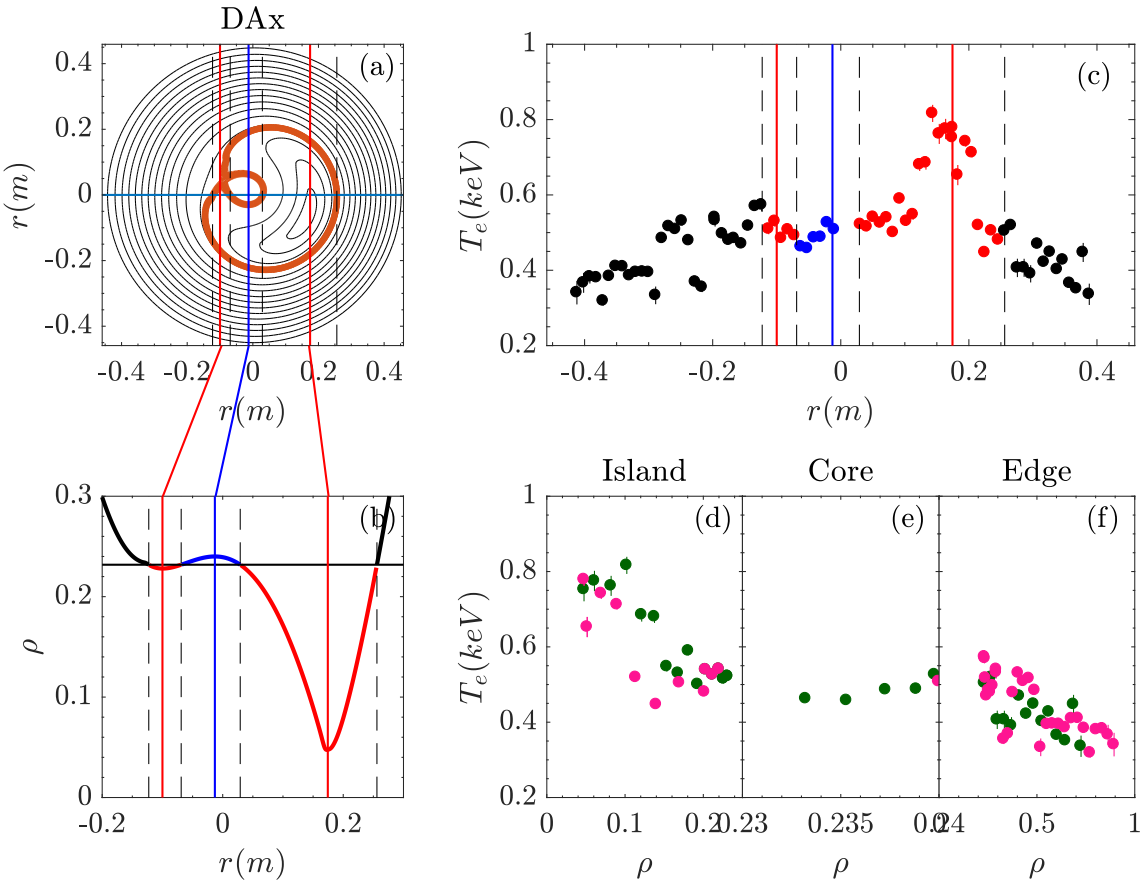

Figure 3.7: Electron temperature remapped on the flux surfaces in a DAx state. Vertical dashed black lines represent the location of separatrix intersected by mid plane at Thomson scattering angle $\phi = 82.5°$. The vertical thin lines represent the local maximum or minimum of the helical flux (red for island region and blue for the core region). (a) Contour plot for the helical flux on the poloidal cross-section at Thomson scattering toroidal angle. The horizontal line represents the Thomson scattering laser path and the thick red curve represents the separatrix. (b) The normalized helical flux plotted versus the geometrical radial, zoomed at the island region. The horizontal line represents the separatrix, intersected with the curve with four intersections, marked with the dashed black line. There are two parts belonging to the magnetic island, marked with red. The blue part is the core region and the two black parts on both sides of the profile represent the outer region. (c) The Thomson scattering profile versus radius of vacuum vessel. The colors represents different regions. (d), (e) ,(f) The results of remapping in the magnetic island (d), core (e) and outer region (f). The color pink represents left side and the color green represents the right side of the local ρ minimum.

as the two red curves, together with one core region, marked as blue. The two black curves are the outer regions. The horizontal black line represents the separatrix. The four vertical dashed black lines are the corresponding intersections shown in graph a.

Panel (c) The electron temperature, measured by Thomson scattering diagnostic, is plotted versus the geometrical radius. The red color indicates the island region, the blue color indicates the core region and the black color indicates the outer region.

Panel (d) Remapped electron temperature in island region is plotted versus ρ. The remapping procedure consists in building the relations between T_e and ρ, through the information of the radial distribution. The pink color represents the right side and the green color represents the left side.

Panel (e) The remapped electron temperature in the core region.

Panel (f) The remapped electron temperature in the outer region.

The minimum helical flux does not reach the value zero in Figure 3.7(b). This is due to the fact that the Thomson scattering laser did not detect, in fact most of the cases it cannot, the island center where the true minimum helical flux lays. This points out the fact that the electron temperature measured with Thomson scattering diagnostic cannot necessarily show the whole thermal structure. Nonetheless, the information of the thermal gradient can be, at least partially reflected via the T_e profiles obtained. Meanwhile, most of the T_e points measured in experiments are in outer region. This leads to the problem that the points in island region sometimes are limited.
Now, with the well defined radial coordinate ρ, the remapped electron temperature, one could perform 1.5 dimensional transport study on both multiple axes configurations and single axis configurations, with the help of code MAxS. However, before putting MAxS into practice, one needs to perform a benchmark study. In the next section, the benchmark work is presented between MAxS and the well-know transport code ASTRA [87].

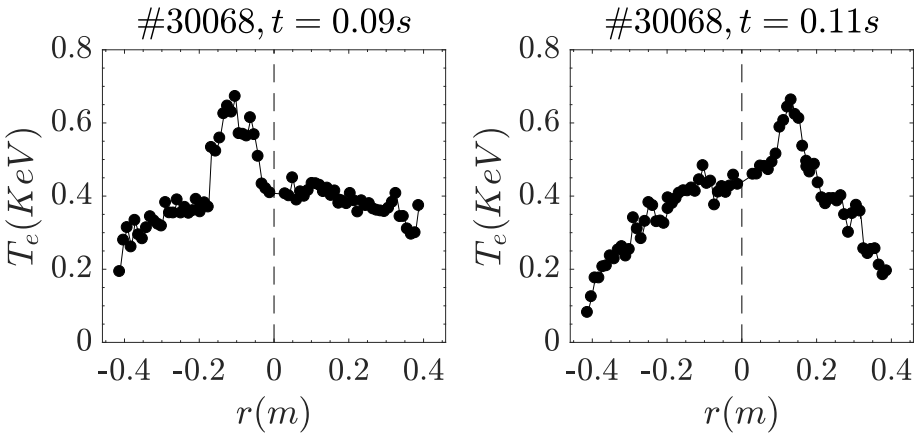

Figure 3.8: Two typical electron temperature profiles is presented as a function of the radius r, obtained both in SHAx$_n$ state. These two cases are used in the benchmark between MAxS and ASTRA.

3.5 Benchmark with ASTRA

MAxS has been developed and benchmarked with the well know 1.5 dimensional transport code ASTRA. The benchmark has been carried out based on two SHAx$_n$ cases obtained in RFX-mod with the corresponding electron temperature profiles shown in Figure 3.8, measured with Thomson Scattering diagnostic. The quantities ρ, $T_e(\rho)$, V' and G_1 are provided by the code SHEq[2] . The benchmark has been carried out on two aspect:

1. Numerical point of view. On this point, the basic idea is that with the 'same' input, being the thermal diffusivity profile, the same metrics and the power deposition profiles, the two outputs, being the simulated electron temperature profiles T_e^{sim}, should show good agreement. The thermal diffusivity profile is simplified to be one with straight line connecting some critical points which are essential to describe the feature of the experimental temperature profile T_e^{exp}. The number of the critical points is a free parameter. In the present test, the number and the position of nodes have been chosen to set the central

[2]Note that in the previous section the T_e remapping is done with a radial coordinate defined with the normalized helical flux (Equation 3.6). This remapping process is presented to show the general technique of how to perform a remapping with a defined radial coordinate. However, this definition is not used by SHEq. Instead, SHEq uses the definition from the volume (Equation 3.4).

diffusivity, the starting and ending points of the eITB, the starting and ending point of the external T_e gradient and the edge diffusivity.

2. 'Physical' point of view[3]. On this point, the basic idea is that the 'best' solution from MAxS code should be in the reasonable physical range[4].

First of all, the benchmark has been carried out on the numerical point of view. The main work is listed as follows:

- Provide MAxS the electron temperature profiles obtained from experiments, being T_e^{exp}, the metrics and the surface averaged power deposition profiles.
- Set the thermal diffusivity profile *manually*. With proper boundary conditions, run MAxS and get the simulated $T_e^{sim,MAxS}$ profile.
- Compare $T_e^{sim,MAxS}$ and T_e^{exp}. If these two profiles show good agreement, then the corresponding χ profile is the one we are seeking for. If the two profiles show bad agreement, go back to step 2 and *manually* change the χ profile until these two profiles show good agreement.
- Apply the χ profile obtained above on ASTRA and get the corresponding $T_e^{sim,ASTRA}$.
- Compare $T_e^{sim,MAxS}$ with $T_e^{sim,ASTRA}$. If these two profiles agree with each other, the benchmark on the numerical point of view is good and otherwise it is bad.

Using the two cases shown in Figure 3.8, the benchmark on the numerical part is presented in Figure 3.9. The upper two graphs are the electron temperature profiles from experiments (black stars) and from simulations (red lines). The lower two graphs are the corresponding thermal diffusivity profiles (red lines) used to perform the simulations. It is obvious to see that the $T_e^{sim,MAxS}$ and $T_e^{sim,ASTRA}$ overlap with each other, actually it is almost impossible to tell the difference between these two red lines. This good agreement shows that MAxS is capable of producing solid simulations with good numerical stability.

[3]Here one needs to be aware that the physical benchmark is not between real experiments and the simulation results. It is just a way to see if the results produced by MAxS is within the reasonable range or not.

[4]The best range is provided by the ASTRA, generated automatically with Genetic Algorithm. A more detailed description is given in the following part about physical benchmark.

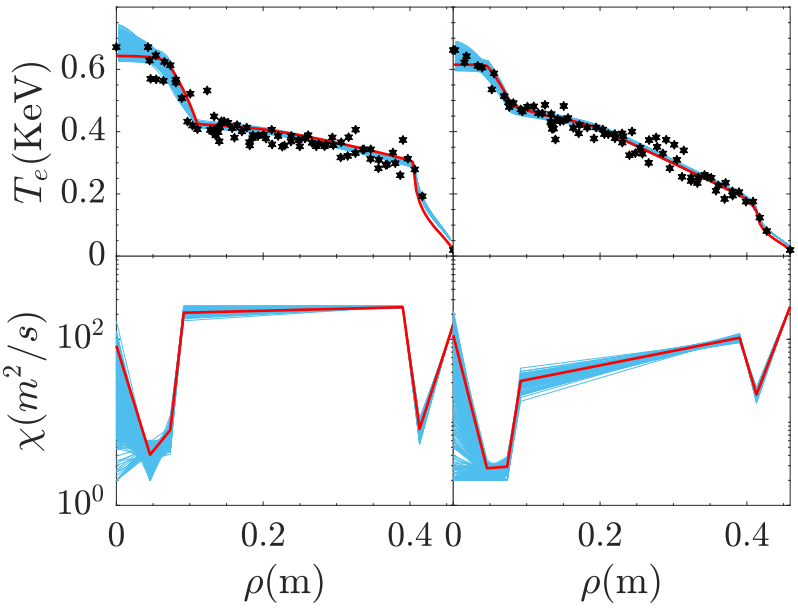

Figure 3.9: Results of benchmark between MAxS and ASTRA, applying two SHAx$_n$ cases in RFX-mod. The lower two graphs are the thermal diffusivity profiles and the upper two graphs are the corresponding electron temperature profiles. For the numerical benchmark, the results are shown with red lines. The thermal diffusivity profiles (two red lines in the lower graphs) are used to perform the simulations, both in MAxS and ASTRA. The corresponding T_e profiles are shown as the red lines in the upper graphs. The two red T_e lines shows good agreement, indicating a reliable numerical stability of MAxS. For the physical benchmark, the results are shown as the blue lines, being the CI's generated by ASTRA via GA. The red lines, both with T_e profiles and the χ profiles are well agreed with CI's, indicating a reliable capability of producing solid physical simulations with MAxS.

With good results on the numerical benchmark, now the physical benchmark is performed. As mentioned above, the χ profile obtained in MAxS manually should be in the reasonable range on the physics point of view. The reasonable range in this work is generated by the Genetic Algorithm (GA) implemented in ASTRA, which could automatically generated a set of 'good quality' χ profiles, named Confidence Intervals (CI's) [88]. The GA is a metaheuristic inspired by the process of natural selection that belongs to the larger class of evolutionary algorithms. It is a numerical search tool aiming at finding the global optimum of a given real objective function of one or more real variables, possibly subjected to various linear or non-linear constraints.

The 'quality' of the provided χ profile is quantified by evaluating the normalized squared distance d^2 between T_e^{exp} and T_e^{sim}:

$$d^2 = \sum \left[(T_e^{exp} - T_e^{sim})^2 / (T_e^{exp})^2 \right] \tag{3.7}$$

The GA could automatically choose a set of χ profiles and afterwards, ASTRA can generate the corresponding T_e^{sim} profiles as well as the values of d^2. The acceptance of χ profiles is based on the criteria that the value of d^2 is no larger than 10% of the minimum d^2, denoted as d_m^2:

$$d^2 < 1.1 d_m^2 \tag{3.8}$$

Through these processes, a set of 'good' χ profiles, together with the corresponding T_e^{sim} profiles are thus obtained. The results are also shown in Figure 3.9, marked as the blue lines. It is clear to see that both the χ profile and T_e^{sim} profiles are well agreed with the CI's generated by ASTRA, showing that the χ profile obtained from MAxS is reasonable from the physics point of view.
The above presented benchmark work shows that MAxS is capable of performing robust transport simulations, both in terms of numerical stability and the physics aspect, which gives confidence in using MAxS to perform further transport study. Here it is worth mentioning that after the benchmark, the Genetic Algorithm has also been implemented into MAxS for further work.

3.6 Summary

This chapter presents firstly a detailed description of QSH state as well as its three sub-states observed in RFX-mod. The three sub-states feature different magnetic topologies as well as different width of thermal structures, which rises the interest of transport physics within these three sub-states. To begin the transport study, the magnetic field is assumed to be a pure SH state by neglecting all the secondary modes. In such a way, a helical symmetry can be defined, as well as the flux surfaces. However, difficulties appear in DAx state which contains multiple magnetic axes and no monotonic coordinate could be defined to describe the whole plasma volume. Facing this issue, a Multiple Domain Scheme is adopted, dividing the whole plasma into three separated regions and monotonic radial coordinate thus could be well defined in each of these three regions. The separatrix plays a role of 'bridge' to connect these three separated regions, with assumptions of small volume and uniform temperature. With the help of MDS, the radial coordinate as well as the correct metrics are defined in each zone and the electron temperature, plasma current profile can thus remapped over the flux surfaces. Finally, applying these ideas mentioned

above, a code named MAxS has been developed and benchmarked in single helical axis state with ASTRA, a well known transport code. The results of benchmark show a good agreement between these two codes and this gives us the confidence to perform energy transport study on these three sub-states of QSH, which will be presented in the next chapter.

4 Thermal Properties of Three sub-states in QSH state

Three sub-states within one cycle of QSH state have been described in the previous chapter. Here the study on thermal properties in eITB region, with the help of a routine named TeGrA, as well as the study on the energy transport, with the help of MAxS, are presented. The behavior of thermal gradients with respect to both dominant and secondary modes is presented and discussed within the framework of stochastic transport theory. The transport study confirms the results obtained in the thermal property study. In the end, the total energy confinement time is evaluated within these three sub-states.

4.1 Transport and Thermal Properties of QSH State

Transport study has been carried out on RFP plasmas. An energy transport study on EXTRAP T2R shows that the thermal diffusivity is two orders magnitude lower inside of the dominant magnetic island than outside [83]. This indicates a good confined region is formed inside of the magnetic island. Nevertheless, the thermal diffusivity inside of the magnetic island is still one order magnitude higher than the one evaluated in tokamak configurations. This result implies that transport in QSH state, although improved compared with MH state, is still dominated by stochasticity. Indeed, further study on SHAx$_w$ thermal structures in RFX-mod shows that the minimum thermal diffusivity, being one inside of the magnetic island increases with the increase of the secondary modes [89]. This results confirms that the thermal diffusivity is strongly affected by the stochasticity produced by the overlapping of the secondary modes. Besides the study on the transport aspect, Reference [90] also reported a thermal expansion phenomenon in which the thermal width among these three sub-states shows a sudden jump from narrow to wide thermal structures. Inspired by the transport study mentioned above, this chapter presents the study on the thermal properties, transport and energy confinement behaviors of three sub-states in QSH.

The work is based on a selected database which contains 208 electron temperature profiles obtained in QSH state, with Thomson scattering diagnostic whose signal

path lies in the equatorial plane at the toroidal angle $\phi = 82.5°$. The angle between the Thomson scattering laser path and the line going through the maximum thermal width is between -35° and 35° in order to be sure not to miss the highest temperature region in the plasma. The detailed procedures have been described in Section 6.5, Chapter 3. The database is further selected based on narrow plasma density and current ranges. The plasma density varies between 2.5 and 3.5 $10^{19}m^{-3}$, and the plasma current varies from 1.2 to 1.5MA. The purpose of this further selection is to keep the plasma parameters relatively the same so that the phenomenon observed in the data analysis part is independent from the variation of plasma parameters. This new database contains 53 electron temperature profiles.

TeGrA Code

The thermal properties of the electron temperature profiles, especially in the eITB region, should be studied to understand the evolution of the three sub-states of a QSH state. For this purpose, a code named Thermal Gradient Automatic analysis (TeGrA) has been developed to automatically detect the information of the eITB region in the three sub-states. a typical electron temperature profile, which is shown in Figure 4.1. It is measured in SHAx_w state and it is plotted as a function of the geometric radius r. There is one nearly flat region with high electron temperature in the core and on both sides of the flat region, there are two temperature gradients, marked with the blue shadow which are the eITB regions. The width of the eITB is denoted as $\Delta r_{Foot,R-L}$ with subscript $Foot$ meaning the foot of the gradient and $R-L$ meaning the two regions located in the right and left side of the thermal structure. The width of the flat top is denoted as Δr_{Top}. The corresponding temperature values of the top and foot of the eITB region are denoted as $T_{e,Top}$ and $T_{e,Foot}$, respectively. The TeGrA code, in general, has the same procedure for all the T_e profiles with minor differences between narrow T_e profile and wide ones. TeGrA is based on the principle that the left and right of the eITB foot and top should share the same T_e value, which is equivalent to the assumption that T_e is a function of the helical flux surfaces labeled by ρ. The main steps for TeGrA are:

- Get the original $T_e(r)$ profile.
- Get the mean value of the $T_e(r)$ profile, T_e^M.
- For top analysis, update the $T_e(r)$ profile according to $T_e(r) > (1-x_1)T_e^M$ with $0 < x_1 < 1$, a parameter to be decided based on the profiles.

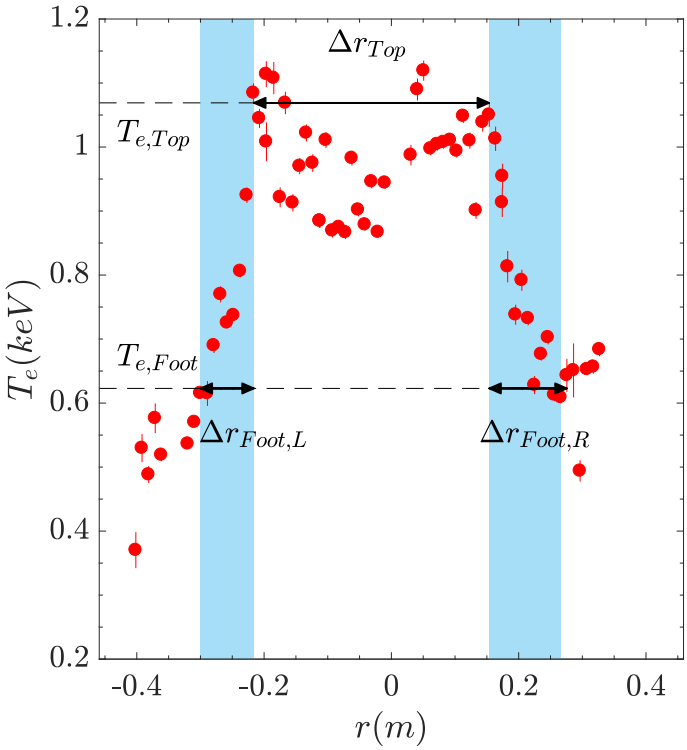

Figure 4.1: A typical electron temperature profile measured in SHAx$_w$ state is plotted as a function of radius r. The blue shadow indicates the eITB region and the black arrows represent the width of the thermal structure top Δr_{Top} and the width of the eITB $\Delta r_{Foot,R-L}$ with $R-L$ indicating the right and left of the eITB. The black dashed line represents the electron temperature value of the eITB for the top T_e^{Top} and foot T_e^{Foot}.

- Repeat step 2 and 3 on the updated $T_e(r)$ profile until the value of T_e^M does not change anymore; the final value of T_e^M is the top electron temperature $T_{e,Top}$ with its corresponding two values of r, $r_{Top,R-L}$ on both sides of eITB, and the width of top is thus calculated:

$$\Delta r_{Top} = |r_{Top,R} - r_{Top,L}| \tag{4.1}$$

For foot analysis, similar steps are applied with a difference in step 2 which is $Te < (1+x_2)T_e^M$, where $0 < x_2 < 1$. The outcomes from the foot analysis are: the foot temperature T_{Foot} and the corresponding two locations $r_{Foot,R-L}$ on both sides of the eITB. The left and right width of eITB foot, being $\Delta r_{Foot,L}$ and $\Delta r_{Foot,R}$,

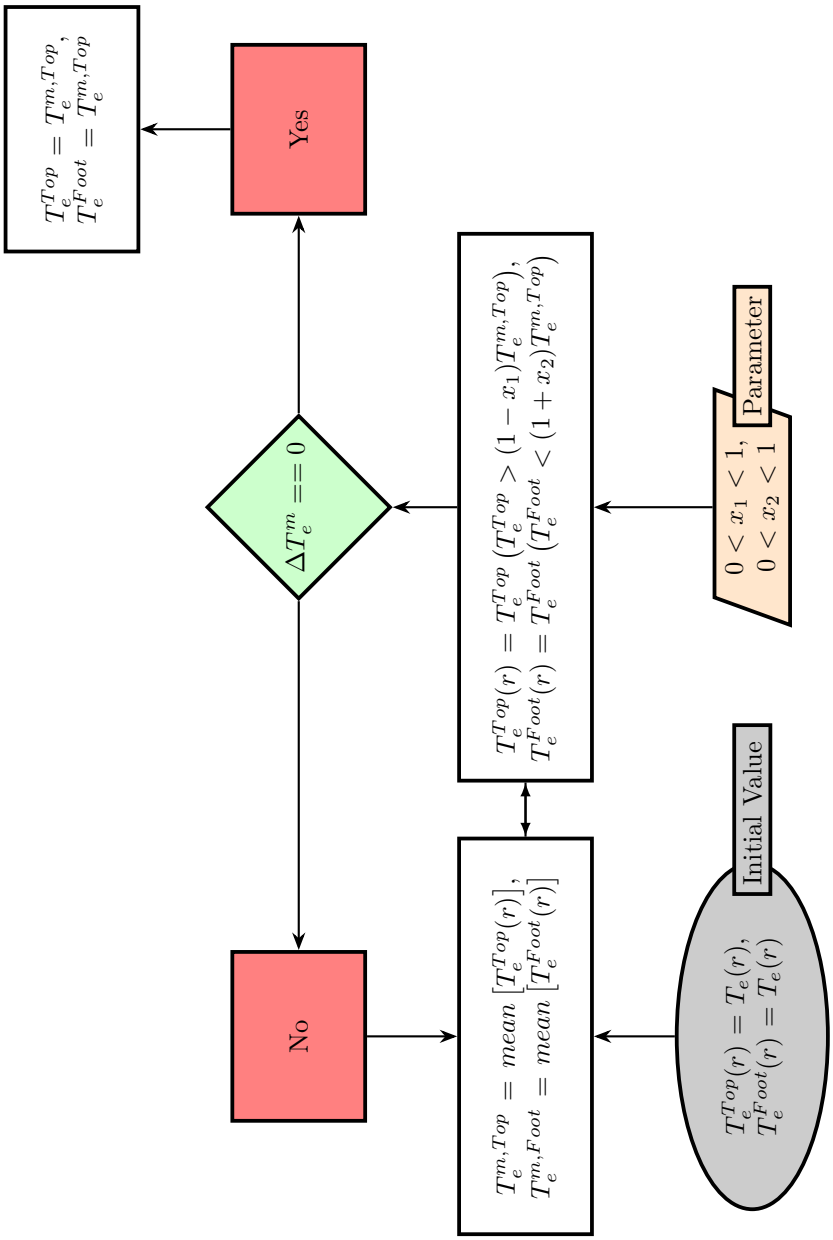

Figure 4.2: The main steps for code TeGrA. $T_e(r)$ is the raw experimental electron temperature profile, as a function of the radius r.

respectively, are thus obtained:

$$\Delta r_{Foot,L} = |r_{Top,L} - r_{Foot,L}| \qquad \Delta r_{Foot,R} = |r_{Top,R} - r_{Foot,R}| \tag{4.2}$$

The choices of parameters x_1 and x_2 should be adjusted in order to get reliable fitting results for all the profiles. The main steps of TeGrA are shown in Figure 4.2.

Thermal Gradient and Transport Study

Applying TeGrA on the selected database, the *absolute value* for left and right thermal gradients of the electron temperature could be easily obtained, denoted as ∇T_e^L and ∇T_e^R. The minimum values of the two gradients are shown in Figure 4.3, as a function of the toroidal component of the dominant mode $b_\phi^{1,-7}$ normalized to the edge magnetic field $B(a)$. The error bar is estimated as follows:

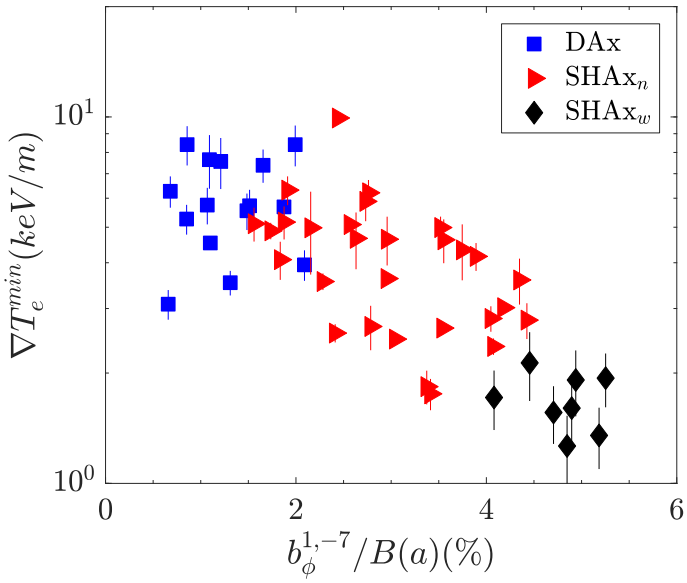

Figure 4.3: The minimum temperature ∇T_e^{min} between ∇T_e^L and ∇T_e^R is presented as a function of the dominant mode normalized by the edge magnetic field.

$$\delta\nabla T_e/\nabla T_e = \sqrt{\sum(\delta T_e/T_e)^2 + \sum(\delta r/r)^2} \tag{4.3}$$

Where δT_e and δr are the experimental error bars of the electron temperature and the corresponding radial locations. The symbol $\sum$ means the sum over the total

points which are included in the calculations of the top or foot temperatures in the last step in code TeGrA. The error on the radius $\delta r/r$ is much smaller than the error of temperature $\delta T_e/T_e$, so here the error is only calculated based on the error of the electron temperatures.

The thermal gradients shown in Figure 4.3 reveal two clear separations among those three sub-states, with respect to the normalized dominant mode. The first separation is between DAx and SHAx$_n$ states when the normalized dominant mode $b_\phi^{1,-7}/B(a) \approx 2\%$, and the second separation is between SHAx$_n$ and SHAx$_w$ where $b_\phi^{1,-7}/B(a) \approx 4\%$. Furthermore, with the increase of the normalized dominant mode, the minimum temperature gradient shows an overall clear decreasing trend, with a wide spread in DAx case. This result might give us a hint of a local increase of energy transport in the eITB region and this might play a role in the energy confinement behavior. To check this point, a transport study using MAxS has been performed. The simulation has been performed on a small database containing these three sub-states of QSH state. Typical thermal diffusivity profiles obtained from one DAx case and from one SHAx$_n$ case are presented in Figure 4.4. The black lines are the results of 'good' χ profiles, i.e., CI's generated by the GA. The panel a, b, c are the χ profiles obtained from one DAx case and they represents the core, island and outer regions, respectively. The eITB region contains two points and they are characterized by lowest thermal diffusivity, which is marked with blue shadow. Panel d is the χ profiles from one SHAx$_n$ case and the eITB region is also marked with the blue shadow. It is clear to see that outside the eITB region, the thermal diffusivity is around two orders magnitude higher, which is consistent with the results reported in Reference [83]. Here the mean value of the thermal diffusivity in eITB region, $\langle \chi_{th} \rangle$, is used to characterize the overall thermal diffusivity in the eITB region and the error is evaluated as:

$$\delta\chi / \langle \chi_{th} \rangle = \sqrt{\left(\sigma\chi_{th}^1 / \langle \chi_{th}^1 \rangle\right)^2 + \left(\sigma\chi_{th}^2 / \langle \chi_{th}^2 \rangle\right)^2} \tag{4.4}$$

Here $\sigma\chi_{th}$ indicates the standard deviation of the thermal diffusivity and the superscript 1 and 2 indicate the two points in the eITB region. The two quantities $\langle \chi_{th}^{1,2} \rangle$ indicate the mean values of thermal diffusivity in each point. The simulation result is shown in Figure 4.4e. Note that the GA has not applied to all the cases since the time consuming is very high. Here only 10 cases (4 DAx, 3 SHAx$_n$ and 3 SHAx$_w$) are performed with GA to get the general idea of the error bar. The rest of the points are using MAxS only. It shows a clear increase trend from DAx to SHAx$_n$ and SHAx$_w$. This trend suggests that the energy transport in eITB region indeed increases within these three sub-states. This result confirms the guess made before in Figure 4.3. Another point which should be clarified is that the value of thermal

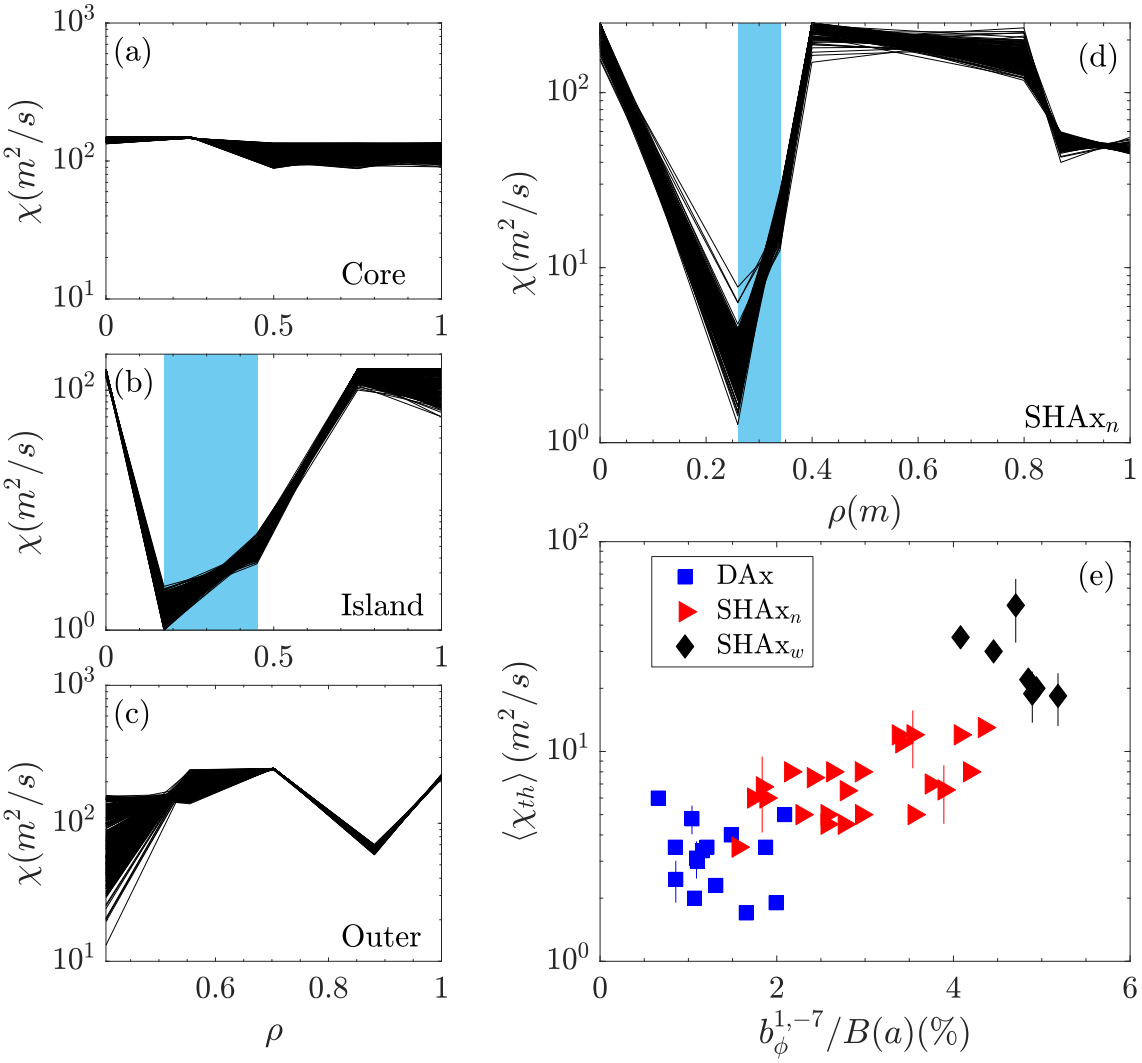

Figure 4.4: Panel (a), (b) and (c) are the χ profiles obtained from one DAx case and they represent the core, island and outer regions, respectively. Panel (d) is the χ profiles obtained from one SHAx$_n$ case. The black lines represent the χ profiles obtained from GA and the minimum value of χ appears in the eITB region, which is marked with blue shadow. Panel (e) is the results of the transport study on s small database containing three sub-states of QSH. The mean value of the thermal diffusivity in the eITB region, $\langle\chi_{th}\rangle$ increases from DAx to SHAx$_n$ and SHAx$_w$, suggesting a local increase of the energy transport in eITB region.

diffusivity presented here is the average value while the value presented in Reference [89] is the minimum one. This explains the reason why in Reference [89], the best case of χ was found to be around value $5m^2/s$ while here the value is above $15m^2/s$. This behavior of thermal gradients with respect to the normalized dominant mode is peculiar since they show a trend with the dominant mode which is opposite to that of the amplitude of the thermal width. In order to understand this phenomenon, further investigation on the secondary modes, which are the source of stochasticity in RFP plasmas, has been carried out and it is presented in the following section.

4.2 Thermal Gradient Influenced by Stochasticity within Three Sub-states

The thermal gradient behaves in a peculiar and unexpected way with respect to the dominant mode and this result encourages us to further study the role of secondary modes in setting thermal gradients in eITB regions. The amplitude of the secondary modes used here is investigated using the cumulative amplitude, defined as: $b_{sec} = \left(\sum_{n=-8}^{-17} b_{1,n}^2\right)^{1/2}$. Figure 4.5a shows the minimum gradient versus the secondary modes normalized to the edge field. The plot shows a clear separation between two groups: group 1, with narrow thermal structures (SHAx$_n$ and DAx); group 2 with wide thermal structures (SHAx$_w$). This separation between these two groups occurs when the normalized secondary modes are around 0.85%.

The discussion on this two different behaviors needs the help of Reference [90]. To be more specific, in that paper, two physical changes have been identified:

- First of all, among the secondary modes, the sub-dominant one, being m=1, n=-8, shows a significant decrease in the wide thermal structure group (SHAx$_w$ sate).
- Secondly, the location of the thermal gradients shows a difference between narrow (DAx and SHAx$_n$) and wide (SHAx$_w$) thermal structure groups. To be more specific, in narrow thermal structure group, the location of thermal gradients is within the sub-dominant mode m=1, n=-8 resonance radius. However, in wide thermal structure group, the location of thermal structures 'migrates' to a new one, being between mode m=1, n=-8 and mode m=1, n=-9 resonance radii.

The above mentioned two observations indicate that the source of stochasticity between narrow and wide thermal structure groups modifies. For the narrow thermal

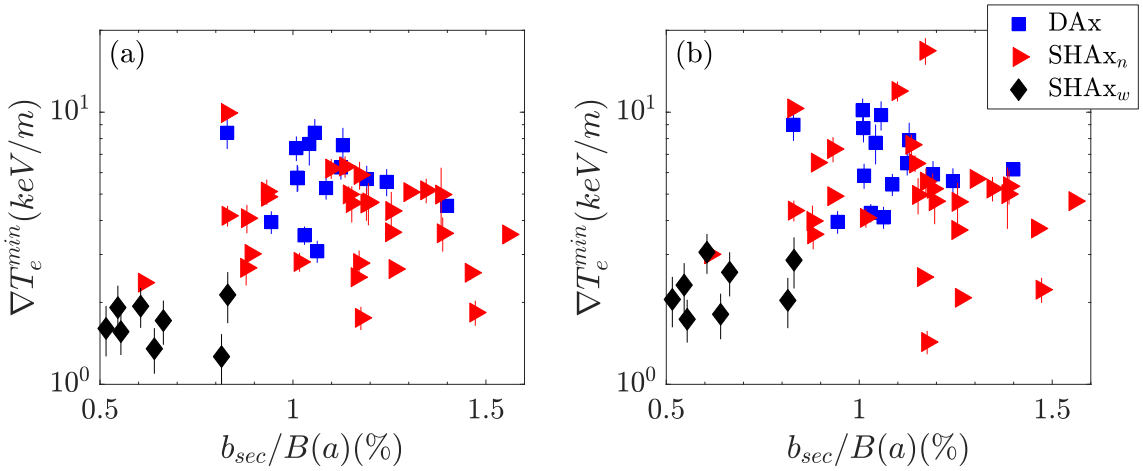

Figure 4.5: The minimum gradient is plotted versus the normalized secondary modes. (a). The data is obtained at the TS angle. (b). The data is obtained in a new toroidal angle at which the O-point (for DAx) or the magnetic axis (for SHAx$_n$ and SHAx$_w$) lies on the mid plane. In both DAx and SHAx$_n$ states, the secondary modes are in the same range while their amplitude is reduced to a lower level in SHAx$_w$.

structure group, since the thermal gradients are located within the m=1, n=-8 mode, the thermal gradients are strongly influenced by the stochasticity produced by the secondary modes m=1, n=-8, -9, -10, -11, $\cdots$. However, in the wide thermal structure group, the thermal gradients 'relocate' in the position between m=1, n=-8 and m=1, n=-9. Consequently, the thermal gradients now are more sensitive to the stochasticity produced by higher n modes, being m=1, n=-9, -10, -11, $\cdots$. What is more, the reason for the 'relocation' phenomenon of the thermal gradients is that the significant reduction of the sub-dominant mode m=1, n=-8. Now, based on these discussions, the interpretation of Figure 4.5a is presented.

First of all, for narrow thermal structure group (DAx and SHAx$_n$), the thermal gradient tends to weakly increase with a wide spread, with the decrease of the secondary modes and the highest thermal gradients exist only for lower secondary modes. The spread in the data may be caused by the range of the selection angle of the helical axis used to build the database. In order to check if the poloidal alignment of the thermal structure with the Thomson Scattering is responsible for the observed data spread, the thermal gradient has been computed remapping the T_e profile over the flux surfaces and rotating the poloidal cross-section along the toroidal angle so that the O-point (for DAx) or the magnetic axis (for SHAx$_n$ and SHAx$_w$) lies on the

equatorial plane. With such operations, the thermal gradients now can be computed along the line with the maximum steepness. This result is shown in Figure 4.5b. The detailed technique of this rotation process is presented in Section 4.4 later in this chapter. The new thermal gradients have higher values because now we are looking in the direction perpendicular to the flux surfaces. Figure 4.5b shows a clearer trend and this negative correlation between the thermal gradients and the secondary modes suggests that in DAx and SHAx$_n$ groups, the heat transport is mainly driven by the stochasticity since the stochastic transport in QSH is produced by overlapping of secondary modes.

Secondly, for SHAx$_w$ group, the steepness of the gradient suddenly decreases. The possible explanation for this behavior is that, during the widening process from narrow to wide thermal structures, the thermal gradient is moving outward, as mentioned above. Thus, in SHAx$_w$ states, the thermal gradient 'relocates' in more outer regions and it is more sensitive to the stochasticity produced by higher n modes. This also indicates that in wide thermal structures, the source producing the stochasticity modifies. Thus, the thermal gradients in SHAx$_w$ suffer higher stochasticity level and that justifies the sudden drop observed in the plot. Figure 4.6 gives a more intuitive understanding of the relative position of eITBs and mode resonances. The black solid curve represents the helical safety factor q profile of a typical SHAx$_n$ state and the red dashed curve represents the one in SHAx$_w$ state. The two shadows represent the range of eITB foot location in narrow (gray) and wide (red) thermal structure groups in agreement with results shown in [90]. It is evident that the foot of the eITB is located internally to the resonance radius of n=-8 mode in narrow thermal structure group. Conversely, in the case of SHAx$_w$, it 'migrates' to an outer location beyond the n=-8 mode resonance. Hence, the thermal gradients in wide thermal structure groups are nearer and likely more sensitive to the high stochastization produced by high n modes.

To confirm the conclusions made above, now we look at the behavior of the thermal diffusivity in the eITB region, respect to the secondary mode and the result is shown in Figure 4.7. It is clear to see that the same separation, shown in Figure 4.5, appears between narrow and wide thermal structure groups. The averaged thermal diffusivity in the eITB region is above $10m^2/s$ while for all the narrow thermal structure group, the value is below $10m^2/s$. In narrow thermal structure group, the averaged thermal diffusivity tends to decrease as the decrease of the secondary modes, indicating that the secondary modes play a stabilization role in the energy transport properties in the eITB region, as their amplitudes decrease. This trend is consistent with the observation made in Figure 4.5. Moreover, between narrow and wide thermal structure groups, a sudden increase on the thermal diffusivity appears,

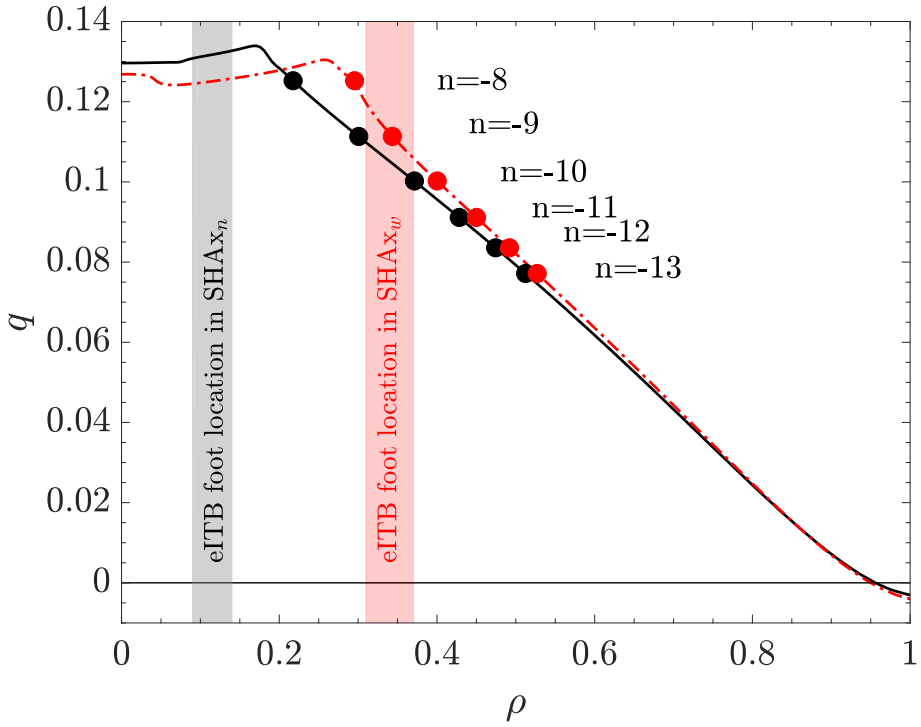

Figure 4.6: Two typical safety factor q profiles in both SHAx$_n$ (black solid curve) and SHAx$_w$ (red dashed curve) states are plotted as a function of the normalized radial coordinate. The two shadows represent the range of eITB foot locations in narrow (gray) and wide (red) thermal structure.

at the point where $b_{sec}/B(a) \approx 0.8$. This behavior confirms the discussions presented before. The eITB region in wide thermal structure groups is influenced by higher stochasticity produced by higher n modes, due to the migration of the foot of the thermal gradients. From the discussions above we know that both dominant mode and secondary modes play a role in setting thermal gradient in eITB region. In both DAx and SHAx$_n$ states, the thermal gradients are, on certain levels, negatively correlated with both the dominant mode and the secondary modes. While in SHAx$_w$ state, the thermal gradient does not share the same behavior.

Now we investigate the weight of setting thermal gradients due to the dominant mode and the secondary modes. The result is shown in Figure 4.8a. The data show a wide spread and the same technique used in Figure 4.5 is applied here too, whose outcome is shown in Figure 4.8b. In DAx state, thermal gradients show an increasing trend with the decrease of the ratio $b_{sec}/b_{\phi}^{1,-7}$ while in both SHAx$_n$ and SHAx$_w$, the ther-

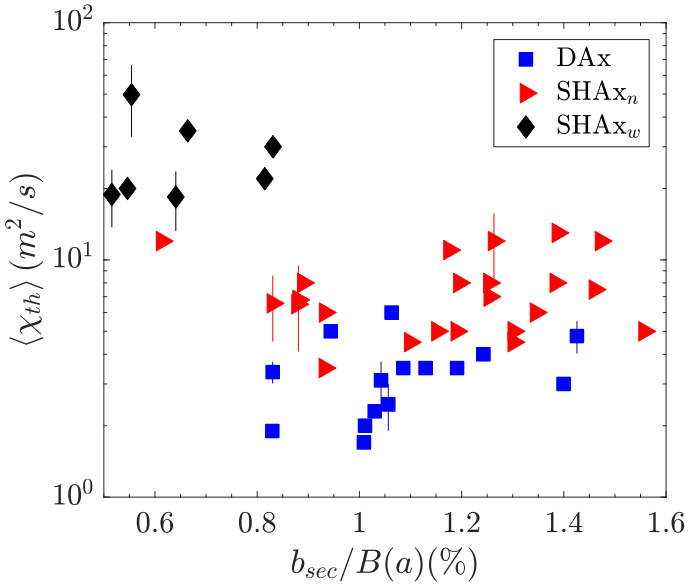

Figure 4.7: The averaged thermal diffusivity $\langle\chi_{th}\rangle$ in the eITB region is plotted as a function of the secondary modes.The same separation appears, as the one shown in Figure 4.5 between narrow and wide thermal structure groups.

mal gradients are positively correlated with the value of $b_{sec}/b_{\phi}^{1,-7}$. Here a possible explanation is presented. This result could be explained by the stochastic reduction due to the presence of the separatrix, which only exists in DAx state. In DAx state, the thermal gradients are maintained by the reduction of stochastic transport due to the separatrix as well as the stabilization effect from the secondary modes. After the disappearance of the separatrix, being in SHAx$_n$, the thermal gradients, still benefiting from the stabilization of secondary modes, suffers more from the increases of stochastic transport due to the expulsion of the separatrix. This explanation offers a possible interpretation of different thermal gradient behaviors between DAx and SHAx$_n$, with respect to the quantity $b_{sec}/b_{\phi}^{1,-7}$. However, to confirm this statement, further investigations should be performed.

Up to now, the transport study in the three sub-states of the QSH state has been presented. The results show an increase of local energy transport in eITB region with the increase of the dominant mode. However, this local increase of energy transport is induced by different sources of stochasticity. In both DAx and SHAx$_n$ states, thermal gradient behaviors are influenced by the stochasticity produced mainly by sub-dominant modes $m = 1, n = -8$ and $m = 1, n = -9$. However, in SHAx$_w$ state,

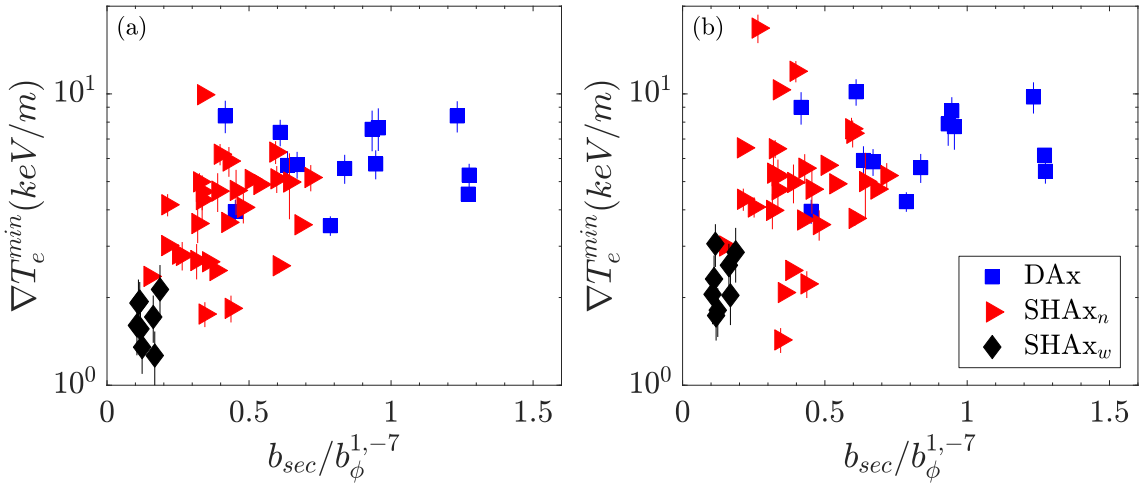

Figure 4.8: Graph (a): The minimum thermal gradient is plotted as a function of $b_{sec}/b_\phi^{1,-7}$. Graph (b), The same quantities obtained in a new toroidal angle at which the maximum thermal gradients laying on the equatorial plane. In DAx group, the thermal gradients shows a negative correlation with respect to the value of $b_{sec}/b_\phi^{1,-7}$ while in both SHAx$_n$ and SHAx$_w$ groups, the thermal gradients show a positive correlation, instead.

the thermal behavior is affected by the stochasticity produced by higher n modes because in such states, the thermal gradients form in the outer region compared with narrow thermal structure states. And finally, between DAx and SHAx$_n$ states, the expulsion of separatrix might also play a role in changing the level of stochasticity in eITB regions.

Thermal Expansion Within Three Sub-states.

In Reference [90], a thermal expansion phenomenon, i.e., the enlargement of the thermal structure, is reported in these three sub-states. Following the reported results, here a detailed study on the process of thermal expansion process is presented. The width of the thermal structure is defined as:

$$W_{Te} = \Delta r_{Top} + \Delta r_{Foot,R} + \Delta r_{Foot,L} \tag{4.5}$$

This quantity is reported that it shows a sudden jump when moving from the narrow to the wide structures [90]. Since the total thermal width contains both the top width and the foot width, here we look into the evolution of Δr_{Foot} and Δr_{top} separately

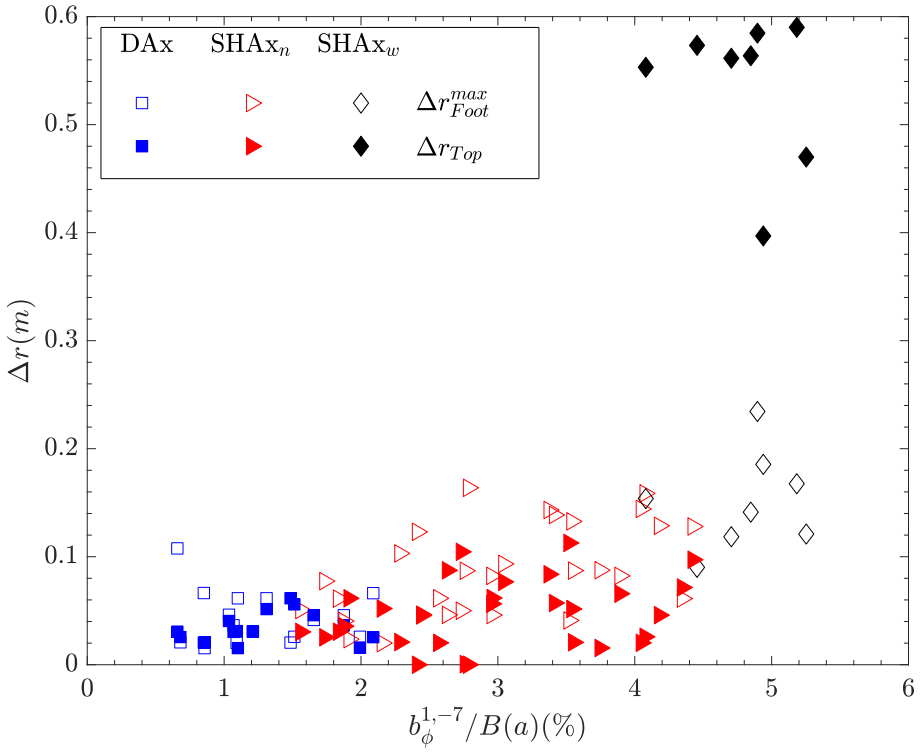

Figure 4.9: The maximum value of the gradient width Δr_{Foot}^{max} (empty symbols) and Δr_{Top} (solid symbols) plotted as a function of the normalized dominant mode. The foot shows a continuous growth while there is a sudden jump between SHAx$_n$ and SHAx$_w$.

and the results are shown in Figure 4.9. The maximum value between $\Delta r_{Foot,L}$ and $\Delta r_{Foot,R}$, Δr_{Foot}^{max} (empty symbols), shows a continuous increase from DAx to SHAx$_{n,w}$ as a function of the normalized dominant mode. Δr_{Top} (solid symbols), on the other hand, shows a sudden jump in its amplitude from SHAx$_n$ to SHAx$_w$. This result indicates that the sudden jump in the thermal width W_{T_e} reported in Reference [90] is due to the growth of the top width in T_e profile rather than the gradient width Δr_{Foot}. The sudden expansion of the top width is induced by the 'relocation' process of the thermal structures which has been discussed already. The continuous thermal expansion from DAx to SHAx$_n$ is sustained by the so-called Quasi-Separatrix Layer (QSL) [90]. The QSL concept is proposed in this way: the distorted magnetic flux surfaces play a role similar to the separatrix which separates the good and bad confinement regions. So from DAx to SHAx$_n$, even with the sudden

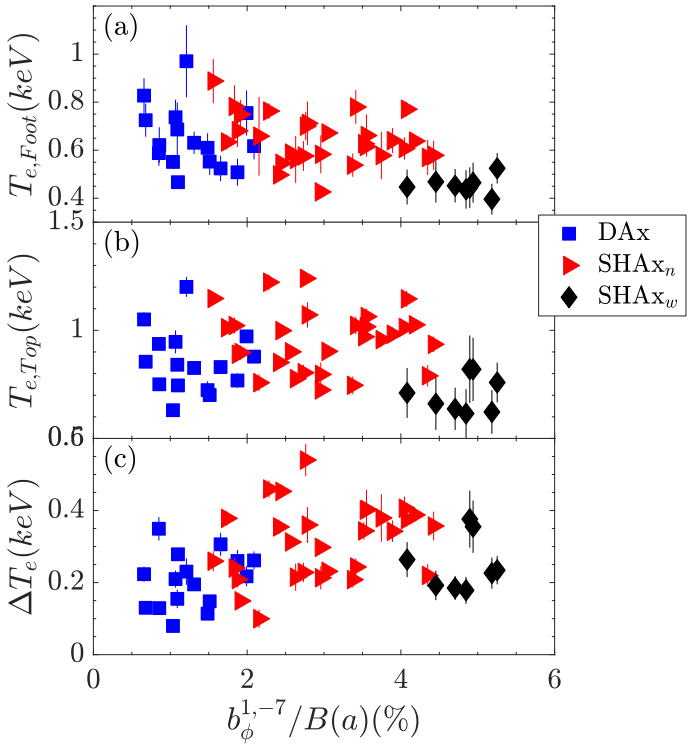

Figure 4.10: The foot (a) and top (b) value of T_e and the difference ΔT_e (c) are shown as a function of the normalized dominant mode. The foot electron temperature slightly decreases from DAx to SHAx$_n$ and to SHAx$_w$ while the top value shows a slightly increase trend from DAx to SHAx$_n$ and then decreases to SHAx$_w$. The corresponding value of ΔT_e shows a increase trend from DAx to SHAx$_n$ and then slightly decreases to SHAx$_w$.

magnetic topology change (i.e., the expulsion of the separatrix), the thermal width exhibits a moderate and smooth growth. However, the behavior of the foot width between SHAx$_n$ and SHAx$_w$ needs to be clarified in the future.

Besides the evolution of the thermal width, the value of $T_{e,Top}$, $T_{e,Foot}$ and $\Delta T_e = T_{e,top} - T_{e,Foot}$ have been calculated and the results are shown in Figure 4.10. The upper graph is the evolution of electron temperature on the foot ($T_{e,Foot}$) of the eITB regions. The middle graph is the evolution of the one on the top ($T_{e,Top}$) of the eITB regions and the third graph is the difference between the top value and the foot value ($\Delta T_e = T_{e,Top} - T_{e,Foot}$). From the plots we see that the value of $T_{e,Foot}$ slightly decreases within these three states. An explanation is that the foot of the eITB is

expanding towards outer regions where the electron temperature is lower. The top value, however, shows an increasing trend from DAx to SHAx$_n$ and afterwards, it decreases in SHAx$_w$. Consequently, the value ΔT_e slightly increases from DAx to SHAx$_n$ and then decreases in SHAx$_w$.

4.3 Energy confinement time

The peculiar behavior of the thermal gradients presented in the previous shows an increased local energy transport properties in the eITB region. This result encourages us to check if this local increase could bring effects to the global energy confinement properties. Following this idea, the total energy confinement time is investigated in this section. The definition of the energy confinement time is:

$$\tau = \frac{3}{2} \int_V K_B n (T_e + T_i) dV \big/ (P_{in}) \tag{4.6}$$

Where K_B is the Boltzmann constant, n is the electron density, T_i is the ion temperature and P_{in} is the input power. Concerning the volume information, a more precise approach, considering the real shape of the non-axisymmetric flux surfaces is adopted with the helical reconstruction of the magnetic field using SHEq. Also, all the profiles used here (T_e, T_i and n) are remapped over the helical flux surfaces based on the same reconstruction. In this way, a more precise energy confinement time is obtained. The density profiles are assumed to have this shape:

$$n = 0.8 n_0 \left[1 - (r/a)^{10}\right] + 0.2 n_0 \tag{4.7}$$

Where n_0 is the plasma density in the core. This is due to the fact that in RFX-mod, the shape of the density profile is mainly ruled by the interplay of stochastic transport, electrostatic transport and source effects [91, 59].
Also the ion temperature is assumed to be the same as electron temperature. Note that this assumption only affects the absolute value of the energy confinement time. The confinement time, plotted as a function of the normalized dominant mode, is shown in Figure 4.11a. In DAx states, the average confinement time is around 1.4ms. It increases to 1.7ms in SHAx$_n$ and eventually in SHAx$_w$, confinement time arrives at around 2ms. The increase of the confinement time indicates a less chaotic plasma in SHAx$_w$ than in DAx. This is confirmed by looking at the global dynamo parameter: $(1 - F)/\Theta$. From Figure 4.11b it can be seen that the dynamo parameter decreases with the increase of the normalized dominant mode, which means that from DAx to SHAx$_w$, the plasma goes into more ordered states.

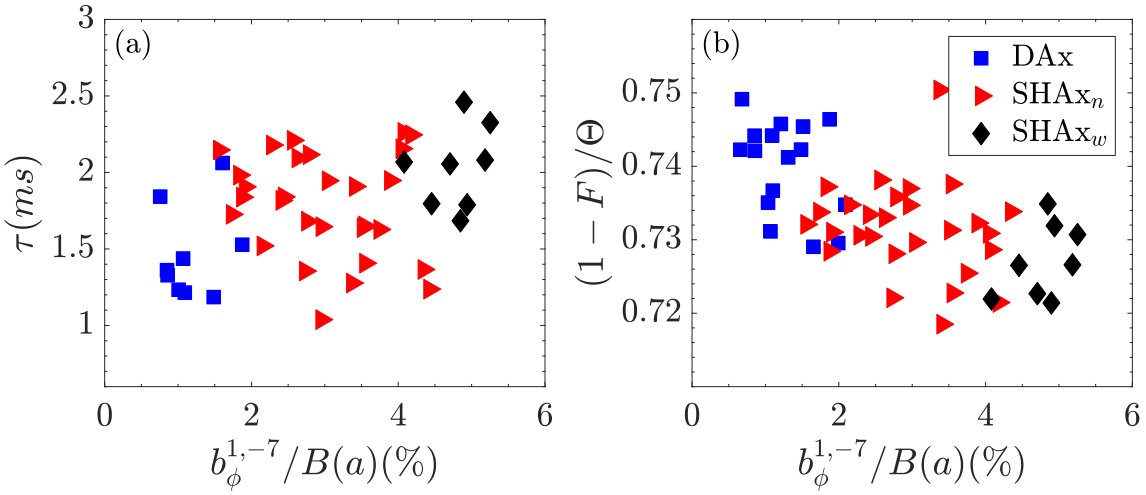

Figure 4.11: (a): Total energy confinement time as a function of normalized dominant mode. The mean value increases from around 1.4ms in DAx up to around 2ms in SHAx$_w$. (b): The dynamo effect $(1-F)/\Theta$ decreases with the increase of the normalized dominant mode.

4.4 Thermal Gradient in new Toroidal Angle

As mentioned above, the database was selected based on the helical axis angle range of -35° and 35°, at the toroidal location of the Thomson scattering. The above mentioned results are based on the experimental data. Here we briefly present the results after rotating the helical axis lies on the equatorial plane. This corresponds to the face that the point with minimum helical flux lies on the equatorial plane. The rotation is based on the principle that after the rotation, the minimum helical flux lies on the equatorial plane. The definition of the helical flux function Φ, containing both the equilibrium flux and the dominant mode flux:

$$\Phi = \Phi_0 + \tilde{\Phi}\sin(m\theta - n\phi + \phi_0) \tag{4.8}$$

Where Φ_0 is the equilibrium flux function, $\tilde{\Phi}$ is the amplitude of the m=1, n=-7 mode flux and ϕ_0 is the phase of the dominant mode. The minimum helical flux laying on the equatorial plane indicates the helical flux should reach the minimum value and consequently we have:

$$m\theta - n\phi + \phi_0 = -\pi/2 \tag{4.9}$$

If the minimum helical flux lies on the high field side, then $\theta = \pi$. If the minimum helical flux lies on the low field side, then $\theta = 0$. Depending on these two differ-

ent situations, the correct toroidal angle which should be used for rotation is thus obtained. The rotation proceeds as follows:

- Get the information of eITB gradients, i.e., four critical locations of the eITB: r^R_{Foot}, r^L_{Foot}, r^R_{Top}, r^L_{Top} and two critical temperatures: T_e^{Top} and T_e^{Foot}.
- Get the helical flux function Φ_{TS} on the Thomson Scattering toroidal angle $\phi_{TS} = 82.5°$.
- Interpolate the helical flux values on the four radial positions of the eITB mentioned in step 1, being $\Phi^{TS}_{Foot,R}$, $\Phi^{TS}_{Toot,L}$, $\Phi^{TS}_{Top,R}$ and $\Phi^{TS}_{Top,L}$.
- Obtain the new helical flux function Φ_{new} at a new toroidal angle calculated based on the rotation principle mentioned above.
- Find the new four radial locations via the four helical flux values obtained in the previous step.
- Using the new radial locations, together with the temperature values obtained in step 1, the new thermal gradients, after rotation are thus calculated.

An example of rotation, performed in a DAx state, is presented in Figure 4.12. Graph (a) and (b) are the contour plots of the helical fluxes before and after rotation, respectively. The red line represents the separatrix. Graph (c) shows the normalized helical flux ρ, which is defined in Equation 3.6, on the equatorial plane versus the geometrical radius. The red lines indicate before rotation and the blue lines indicate after rotation. The vertical lines are the locations of the thermal gradients obtained from TeGrA. Note that in DAx cases, one needs to pay attention that the remapping should perform within the island region because for the same ρ value, there might be another point in the core region. Also one may notice that the ρ_{min} does not reach 0, this should be the reason that the grid to obtain the value of ρ is not dense enough.

The reason why we apply code TeGrA on the Thomson scattering angle rather than on the actual line of maximum thermal width is to reduce the errors induced by the remapping process. As we mentioned in Chapter 3, The remapping suffers some lack of accuracy in DAx cases. Moreover, in single axis situations, even if the remapping results are acceptable, the extra error induced by remapping is hard to evaluate. Nevertheless, here we neglect the errors induced by the remapping process, only considering the error induced by TeGrA, and perform the calculations on the remapped grid in machine coordinates. The results show good agreement with the results shown above in the sense that they both show the same statistical trend. Besides the rotation results shown in both Figure 4.5b and 4.8b, here we present the

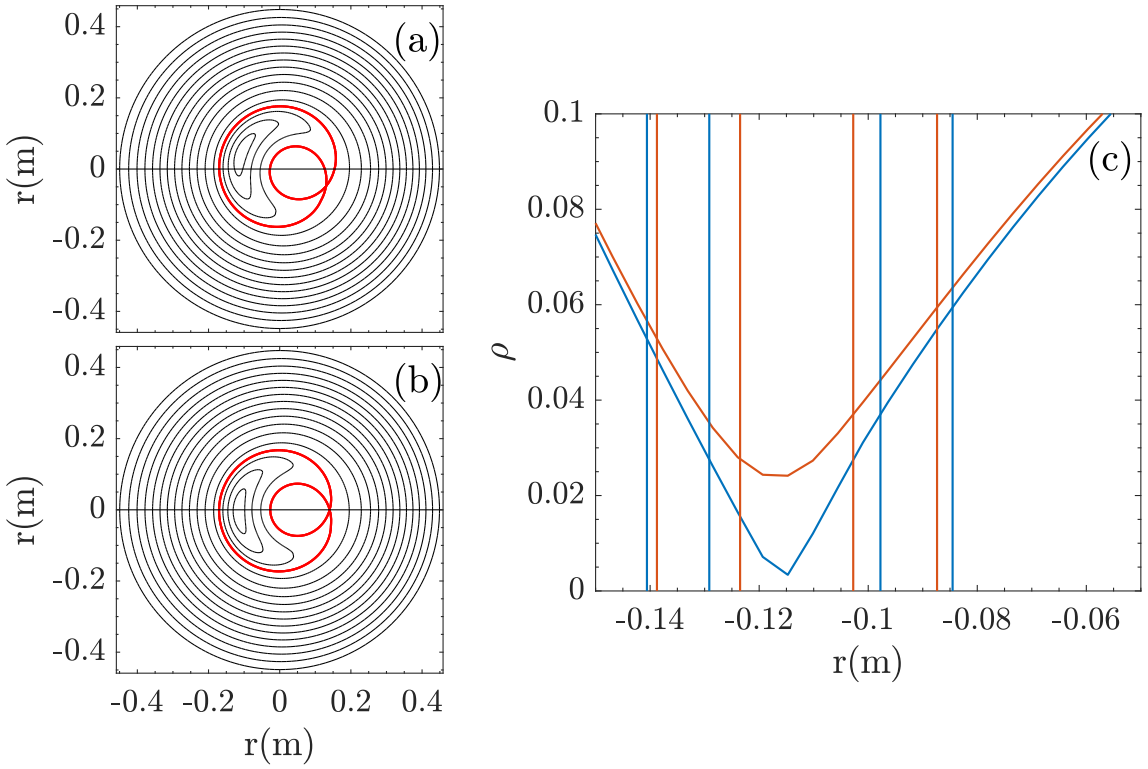

Figure 4.12: An example of rotation is presented. (a), The contour of helical flux at Thomson scattering angle. (b), the contour of helical flux after rotation. (c), The corresponding helical flux along equatorial plane before (red) and after (blue) rotation. The vertical lines represent the location of the thermal gradients obtained from TeGrA.

rest of the quantities discussed above, obtained after the rotation process and this is shown in Figure 4.13. The results presented here show the same trend as before, with increased or reduced spread trend. This is because even the rotation manually moves the thermal structure to the equatorial plane, part of the information of the eITB is missing due to the diagnostic angle in real experiments. Nevertheless, this rotation technique provides us a reference to get better and clearer understanding of the statistic results of the database.

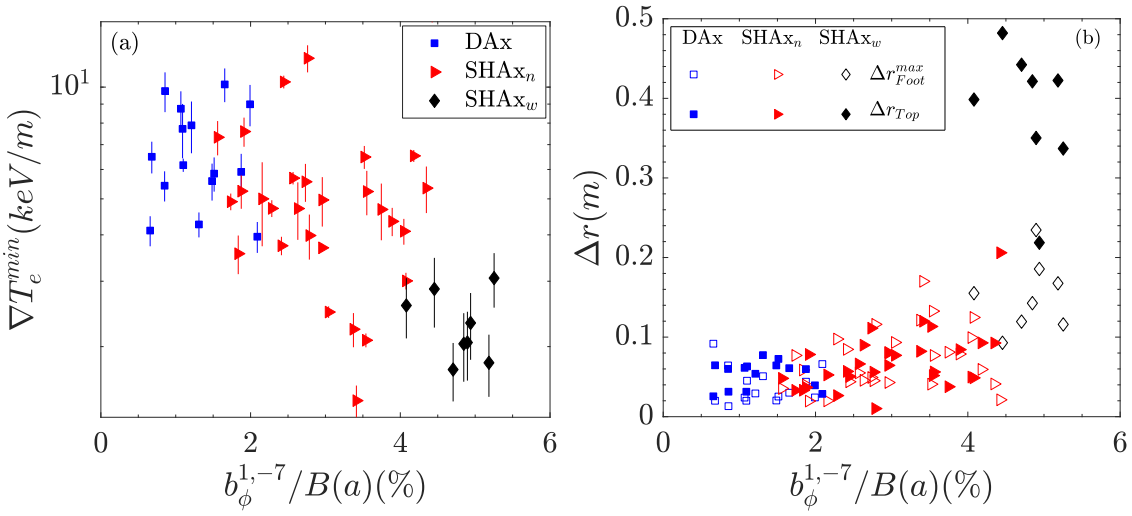

Figure 4.13: Thermal properties after rotation. (a), the minimum thermal gradients versus the normalized dominant mode. (b), The maximum thermal gradient width Δr_{Foot}^{max} (empty symbols) and the top width of the thermal structure Δr_{Top} (solid symbols) versus the normalized dominant mode.

4.5 Summary

This chapter presents the thermal properties, transport and energy confinement behaviors within three sub-states in QSH state, together with the discussions on the behavior of thermal gradients within the framework of stochastic transport, which is believed to be the main transport mechanism in RFP plasmas.

The study on thermal properties begins with the development of the code TeGrA, which could automatically get the eITB information. The outcome of TeGrA, being the thermal gradients, shows a decreasing trend with the increase of the normalized dominant mode. This trend suggests a local increase of energy transport in eITB region and it is confirmed by performing the transport study on the database with the help of the code MAxS. Indeed, the transport study shows that the thermal diffusivity in the eITB region tends to increase as the increase of the dominant mode. This peculiar behavior of thermal gradients encourages us to study the behavior with respect to the secondary modes, which are the source of stochastic transport. The result shows two different behaviors. In both DAx and SHAx$_n$ groups, the thermal gradients weakly increase with the decrease of secondary modes. This can be explained within the framework of stochastic transport: lower secondary modes

indicate less stochastic transport and in turn, this could enhance the confinement properties in eITB region. On the other hand, the thermal gradients show a sudden drop from narrow to wide thermal structure groups. The possible explanation of this result can still be done by the theory of stochastic transport. This different behavior of thermal gradients is due to the modification of the source of stochasticity, which is induced by the 'migration' of their locations. In wide thermal structure states, the location of eITB moves to outer regions compared with the ones in narrow thermal structure states. Consequently, the eITB is more sensitive to the stochasticity produced by higher n modes and the thermal gradients in the wide thermal structure group shows a sudden drop. This discussion has been further proved by checking the behavior of the thermal diffusivity χ with respect to the secondary modes. The result shows that the value of thermal diffusivity indeed jumps from narrow to wide thermal structure groups, indicating the change of stochasticity source. The value of χ tends to decrease as the decrease of the secondary modes, suggesting that the secondary modes play a stabilization role in the eITB region, as their amplitudes decrease. And the very high thermal diffusivity in SHAx_w group indeed shows that in such group, the eITB is more sensitive to the higher level of stochasticity produced by higher n modes due to the migration of the foot of the thermal gradients.
Besides the study on the thermal gradients, the thermal expansion process has also been studied, inspired by the results reported in Reference [90], which is that the thermal width within these three sub-states shows a sudden jump between narrow and wide thermal structure groups. Here a detailed study has been performed on the expansion process. The results show that the sudden jump mentioned above is caused by the top expansion rather than the foot expansion. Moreover, the change on temperatures at the location of top and foot of the eITB is also presented and discussed. The different behavior between top and foot of eITB during this expansion process should be studied in the future.
The above mentioned transport behavior is only localized in eITB region. To get a global view of energy confinement properties, an investigation on the total energy confinement time has been performed, adopting an improved method which provides the more accurate shape of the flux surfaces. The result shows a 40% increase from DAx to SHAx_w, indicating within the evolution of these three sub-states, the plasma enters into more ordered state. This conclusion has been further confirmed by checking the global dynamo parameter, which shows a clear decrease from DAx to SHAx_w.
So far, the work on transport related study on RFX-mod has been presented. The results of this work, though performed and discussed on RFX-mod, should also be valid in other RFP devices. The reason is that the QSH state has been identified in the existing RFP experiments all over the world. The magnetic field in QSH features

the same helical structure spontaneously formed in the RFP discharges, from MH to QSH. On the thermal structure point of view, however, it requires further study. The reason is that RFX-mod is the only RFP device with high spacial resolution T_e measurement so that the thermal structure observed on RFX-mod should be further checked experimentally in other devices. Nevertheless, experiments in MST that has low spacial resolution T_e measurement, showed different thermal structures in the sense that the whole profile is peaked and shifted. The eITB region presented in this chapter seems to be missing in MST T_e profiles. This may due to lack of resolution or it could be caused by much higher neutral particle penetration in MST than in RFX-mod. Hence, detailed study on other RFPs should be carried out to clarify this point.

The following chapters are dedicated to the study of transport modification due to presence of magnetic islands in TJ-II stellarator. Unlike RFPs whose transport process is dominated by stochastic transport, in stellarators and tokamaks, the neoclassical transport plays a role in plasma transport process. Thus, the transport study in the following chapters is based on the study of neoclassical transport. To begin with, a brief description of modification of non-ambipolar fluxes in vicinity of magnetic islands in tokamaks due to the enhanced neoclassical toroidal viscosity is presented. Afterwards, this theory is adopted to TJ-II configuration with a moderate modification to justify the differences between tokamaks and stellarators. And in the end, the modification of radial electric field in TJ-II plasmas is studied.

Part III

Radial Electric Field in Vicinity of Magnetic Island in TJ-II

5

Enhanced Radial Transport due to Magnetic Islands in Tokamaks

A tokamak is a fusion configuration designed to have toroidal symmetry and nested flux surfaces and this is called ideal tokamaks. However, in real tokamak experiments, error fields or MHD activities could break the nested flux surfaces as well as the toroidal symmetry, giving rise to the enhancement of toroidal plasma viscosity. This chapter presents the enhanced radial transport due to the magnetic islands which break the toroidal symmetry and distort the nested flux surfaces in tokamak configurations. More specifically, the enhanced radial transport in vicinity of magnetic islands due to the enhanced toroidal viscosity is presented, following Shaing's theory [63].

5.1 Symmetry Breaking Effect: Enhanced Radial Transport

The tokamak is a toroidal magnetic fusion device featuring toroidal symmetry. Charged particles are bonded on the flux surfaces with small loss via radial transport process across the flux surfaces. This is true within the framework of the neoclassical transport theory, together with the magnetic configuration with possession of perfect toroidal symmetry. In such ideal configurations, particle fluxes Γ_p are intrinsically ambipolar:

$$\Gamma_{p,i} = \Gamma_{p,e} \tag{5.1}$$

The subscribe i and e indicate ions and electrons, respectively. The ambipolar electric field profile is thus constant over time in hydrogen plasmas and the particle fluxes cannot modify it:

$$\partial \boldsymbol{E}/\partial t = \Gamma_{p,e} - \Gamma_{p,i} = 0 \tag{5.2}$$

In such configurations, the guiding center trajectories of particles are closed banana orbits on poloidal cross-section at low collisionality regime [92]. This tokamak configuration with toroidal symmetry is called a *ideal* tokamak. However, in real tokamak operations, the presence of error fields or MHD activities could break the toroidal symmetry, leading to the increase of toroidal viscosity [63]. Consequently, the banana orbits are not closed any more and particles are drifting outwards. An

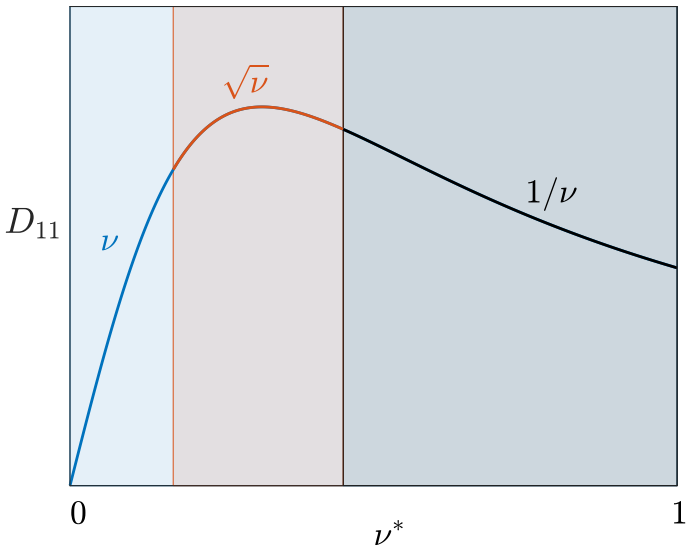

Figure 5.1: A sketch of particle diffusivity D_{11} is presented as a function of the collisionality ν^*. This figure shows only the low collisionality region, i.e., $\nu^* \leqslant 1$. There are three separated regions divided according to different collisionality regions: ν, $\sqrt{\nu}$ and $1/\nu$. This figure is valid for tokamaks with broken toroidal symmetry and stellarators who do not posses the toroidal symmetry.

enhanced radial particle flux is thus induced by the presence of the magnetic islands. This tokamak configuration with broken toroidal symmetry is called a perturbed tokamak.

Recalling the banana region in Figure 2.3, there is a single relation between particle diffusivity D_{11} and collision frequency ν at low collisionality regime in tokamak configurations. The particle orbits in such cases are closed banana orbits. This is true in *ideal* tokamaks with perfect toroidal symmetry. However, when the toroidal symmetry is broken by the presence of magnetic islands, the relationship between D_{11} and ν is modified into three separated regions according to different collision frequencies with higher diffusivity coefficient D_{11} and the particle orbits are no longer closed banana orbits. These three regimes are ν, $\sqrt{\nu}$ and $1/\nu$, respectively and they are exactly the same low collisionality regimes known in stellarators, where no axisymmetry exists by construction. Here ν is the collision frequency. A sketch of particle diffusivity versus collisionality is shown in Figure 5.1, for magnetic configurations with no toroidal symmetry (perturbed tokamaks or stellarators). This will lead to non-intrinsically ambipolar particle fluxes and a local electric field $\boldsymbol{E}$ is thus gener-

ated. This radial electric field could play a role in plasma confinement properties by means of the shear of $\boldsymbol{E} \times \boldsymbol{B}$ flow, which is considered to play an important role in the transition from Low confinement mode (L mode) to High confinement mode (H mode), i.e., the so-called L-H transition by reducing the size of turbulence structure in the plasma edge [93].
The magnetic islands, i.e., MHD tearing modes, exist in resistive plasmas. It modifies the magnetic topology and breaks the toroidal symmetry by distorting and reconnecting the nested magnetic flux surfaces. In vicinity of magnet islands, non-ambipolar flux appears and this leads to the formation of local radial electric field. In the following section, the methodology of Neoclassical Toroidal Viscosity (NTV) theory developed by K. C. Shaing [63] is presented to derive non-ambipolar flux in tokamak configurations with broken toroidal symmetry due to the presence of the magnetic islands. There are two approaches for neoclassical particle fluxes, being moment approach and kinetic approach and it has been shown that the non-ambipolar flux in such configurations is caused by the toroidal viscosity [63] (see Appendix 7.5). In the following sections, the radial electric field induced by the presence of magnetic islands is presented.

5.2 Radial Electric Field in Vicinity of Magnetic Island in Tokamaks

There are at least two mechanisms which can affect the toroidal viscosity. The first one is the electromagnetic torque induced by the interaction between the islands and the wall or error fields [94] and a detailed work has been carried out by A. J. Cole, etc. in Reference [95]. The second one is the plasma viscosity induced by the distortion of the magnetic surface in the vicinity of the magnetic islands. Here we present the theory developed by K. C. Shaing [63], which is focused on the second mechanism. More into detail, the magnetic field perturbation δB, on one side modifies the modulus of the magnetic field and on the other side breaks the nested flux surfaces when it is resonating. The former effect leads to a modification on the neoclassical transport properties and the later one leads to an increase of the non-parallel viscosity [63]. The main contribution to the non-intrinsically ambipolar fluxes comes from the strong modification of the flux surfaces [63] and this is the contribution that we are studying following Shaing's calculations. And finally, Shaing's theory has been developed for the regions both inside and outside of the magnetic island, but we focus only on the particle fluxes outside the separatrix due to the fact that

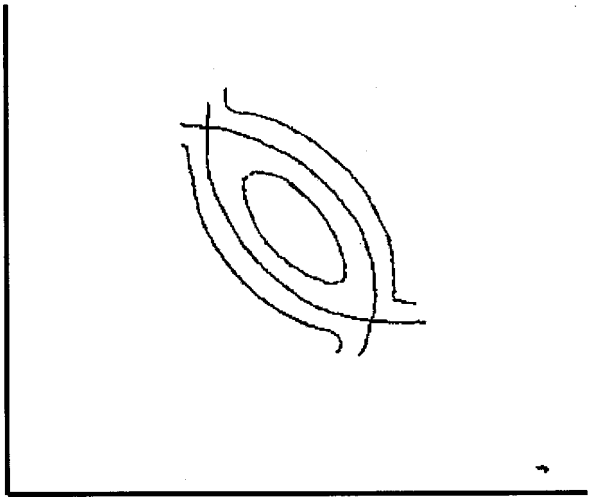

Figure 5.2: A schematic diagram of a magnetic island. The constant Ψ contour is shown.

the size of the magnetic island is small in TJ-II.
To begin with, the proper coordinate system should be introduced. Since we are dealing with regions in vicinity of magnetic islands, a good radial coordinate can be defined with respect to the O-point of the magnetic island. Figure 5.2 shows a contour with constant helical flux function $\Psi = \Psi_P - \Psi_T/q$ with Ψ_P the the unperturbed equilibrium poloidal flux function, q the safety factor and Ψ_T the toroidal flux function. The main idea is to solve the non-ambipolar equation in vicinity of magnetic islands: $\partial \boldsymbol{E}/\partial t = \Gamma_{p,e} - \Gamma_{p,i}$ and for which, we need an explicit formula for the particle fluxes that are functions of the electric field. The particle flux, by definition, is obtained by integration over the whole velocity space:

$$\Gamma_p = \int d\boldsymbol{v} f \boldsymbol{v}_d \cdot \nabla \Psi \tag{5.3}$$

This is an integration over $\boldsymbol{v}$ where $\boldsymbol{v}$ is the velocity, $\boldsymbol{v}_d$ is the particle drift velocity, f is the particle distribution function and $\nabla\Psi$ indicates the radial direction. The theory is to obtain the distribution function f through solving the kinetic equation[1] . The theory focuses on the vicinity of magnetic islands and has the following assumptions:

[1]It is worth mentioning that in the end, it has been found that to get the expression of the particle flux, one does not need the expression of the distribution function. Instead, the expression of $\partial f/\partial k^2$ is enough.

- The tokamak configuration has perfect toroidal symmetry before it is broken by the magnetic islands. In other words, the other factors which could break the toroidal symmetry is neglected, such as the error fields and the discrete toroidal magnetic coils. Under such assumption, the modulus of the equilibrium magnetic field on one flux surface varies only with the poloidal angle θ.

- The theory deals with low collisionality regime, meaning the calculations are carried out on the particle fluxes due to the modification of the banana regime in the three regions: ν, $\sqrt{\nu}$ and $1/\nu$.

- At low collisionality regimes, it is the trapped particles that dominate the transport properties. In order to only consider the perpendicular transport, the bounce averaged kinetic equation is solved with proper transport ordering, to eliminate the parallel transport information. The particle fluxes derived from the bounce averaged drift kinetic equation only contributes to the momentum balance not parallel to the magnetic field [63]. Moreover, the momentum balance depends on the particle drifts that are different for different plasma species. This is the fundamental reason for the appearance of the non-intrinsically ambipolar fluxes.

- The theory only considers the trapped particles in the banana regime, i.e., no *new* class of trapped particles are created by the magnetic perturbations. In particular, the super-banana is not considered here[2]. One of the reason is that it has been proved that including the super-banana does not change the dependence of the particle flux on the radial electric field [96].

- Large aspect ratio devices. With this condition, the $E \times B$ drift velocity is higher than ∇B drift and curvature drift. So the drift velocity could be approximately $V_{E\times B}$. The reason for this approximation is that the size of the drift orbit is $\delta r \sim r V_{dr}/V_{E\times B}$ where r is the minor radius, $V_{E\times B}$ is the $E \times B$ particle drift and V_{dr} is the radial drift speed due to both ∇B and curvature drift. The physical meaning of this condition is to neglect the formation of supper banana orbit [97, 98]. From a mathematical point of view, this assumption is equivalent to the previous one.

- In this chapter, the process of trapping-detrapping process is neglected. Physically this assumption means that the pitch parameter $k^2 < 1$. Allowing the

[2]In the next chapter we will see that we assume this hypothesis true also for stellarators, considering that resonant perturbations have long wavelength, 'seen' by particles trapped in banana regime but not by particles trapped in helical wells (super-banana).

trapping-detrapping process, being $k^2 \sim 1$, brings to the $\sqrt{\nu}$ regime [99]. But this is not reported here.[3]

Solution of the Bounce Averaged Drift Kinetic Equation

The neoclassical toroidal viscosity developed by K. C. Shaing [63] adopts the kinetic description, which starts with the guiding center description of drift kinetic equation. The general kinetic equation for charged particles is:

$$\frac{\partial f}{\partial t} + \boldsymbol{v} \cdot \nabla f + \boldsymbol{a} \cdot \frac{\partial f}{\partial \boldsymbol{v}} = C(f) \tag{5.4}$$

Where $C(f)$ is the Coulomb collision operator and $\boldsymbol{a}$, the acceleration, is given by the Lorentz force:

$$\boldsymbol{a} \equiv \boldsymbol{a}\left(\boldsymbol{x}, \boldsymbol{v}, t\right) = \frac{e}{m}\left[\boldsymbol{E}(\boldsymbol{x}, t) + \frac{1}{c}\boldsymbol{v} \times \boldsymbol{B}(\boldsymbol{x}, t)\right] \tag{5.5}$$

The equation 5.4 could be summarized as:

$$\frac{\partial f}{\partial t} + \frac{dz^i}{dt}\frac{\partial f}{\partial z^i} = C(f) \tag{5.6}$$

Where z^i represents the coordinates in kinetic space. Each guiding center can be specified by its position $\boldsymbol{x}$, magnetic moment μ and energy U: $(\boldsymbol{x}, \mu, U)$. Adopting this guiding center coordinate, equation 5.4 could be reformed as:

$$\frac{\partial f}{\partial t} + \boldsymbol{v}_{gc} \cdot \nabla f + \frac{dU}{dt}\frac{\partial f}{\partial U} + \frac{d\mu}{dt}\frac{\partial f}{\partial \mu} = C(f) \tag{5.7}$$

Where $\boldsymbol{v}_{gc}$ is the guiding center velocity.
Before further discussion on the drift kinetic equation, the gyroradius ordering should be specified. First of all, define the scale length characterizing the plasma L (in toroidal configurations usually L is taken as the minor radius a) and the thermal gyroradius of a charged particle $\rho = v_t/\Omega$, $v_t \equiv \sqrt{2T/M}$ particle thermal velocity and Ω the gyrofrequency, then the plasma is magnetized if:

$$\delta \equiv \rho/L \ll 1 \tag{5.8}$$

[3] In the next chapter, an expression for $\sqrt{\nu}$ is presented.

The quantity δ is the expansion parameter for the purpose of linearizing the drift kinetic equation. For a quantity $\mathcal{A}$ written in form of $\mathcal{A} = \mathcal{A}_0 + \mathcal{A}_1$, the $\mathcal{A}_0$ varies in the scale of L and $\mathcal{A}_1$ varies in the scale of ρ. The collision frequency is in order of

$$\nu/\Omega \sim \delta \tag{5.9}$$

The notation of ordering with expression $\sim \delta$ means the quantity is in the same order of δ and this could also be denoted as $\mathcal{O}(\delta)$. The partial time derivative in Equation 5.6 is assumed to be small:

$$\frac{\partial f}{\partial t} \sim \delta^3 \Omega f \tag{5.10}$$

Note this is a stronger version of ordering and this is called the *transport ordering* [100]. Adopting this ordering, the guiding center velocity $\boldsymbol{v}_{gc}$, who is dominated along the magnetic field $\mathbf{B}$ can be expressed as:

$$\boldsymbol{v}_{gc} = \boldsymbol{b} v_{\parallel} + \mathcal{O}(\delta) \tag{5.11}$$

With $v_{\parallel}$ the velocity component along the field line and $\boldsymbol{b} = \boldsymbol{B}/B$ the unit vector of magnetic fields. The higher order is $\boldsymbol{v}_{gc} = \boldsymbol{b} v_{\parallel} + \boldsymbol{v}_d + \mathcal{O}(\delta^2)$, where $\boldsymbol{v}_d$ is the drift velocity and it is given by [100]:

$$\boldsymbol{v}_d = \boldsymbol{v}_E + \frac{1}{\Omega} \boldsymbol{b} \times \left(\frac{\mu}{m} \nabla B + v_{\parallel}^2 \boldsymbol{\kappa} + v_{\parallel} \frac{\partial \boldsymbol{b}}{\partial t} \right) \tag{5.12}$$

The first part $\boldsymbol{v}_E$ is the $\boldsymbol{E} \times \boldsymbol{B}$ drift velocity, the second and the third part are the field gradient and curvature drift velocity and the last part is the drift velocity caused by field time variation. The curvature is defined as $\boldsymbol{\kappa} = \boldsymbol{b} \cdot \nabla \boldsymbol{b} = -\boldsymbol{b} \times (\nabla \times \boldsymbol{b})$. Since here we neglect the super-banana effect as well as the time variation of the field, the total drift velocity is thus

$$\boldsymbol{v}_d = \boldsymbol{v}_E \tag{5.13}$$

The theory is to solve the linear version of Equation 5.7 by expressing the particle distribution f as

$$f = f_0 + f_1 \tag{5.14}$$

Where f_0 is the zero order distribution function and f_1 is the perturbed distribution function. Thus, we have $C(f) = C(f_1)$. For simplicity reason, the acceleration part in kinetic equation is neglected. Applying the ordering into the drift kinetic equation, the zero order of equation 5.7 would be:

$$v_{\parallel} \boldsymbol{b} \cdot \nabla f_0 = C(f_0) \tag{5.15}$$

The solution is $f_0 = f_M(\Psi)$ for an unperturbed tokamak with f_M Maxwellian distribution function and $f_0 = f_0(\Psi, \alpha)$ for a helically perturbed tokamak and stellarator, where α is the helical angle defined as $\alpha = \theta - \phi/q_s$ with θ the poloidal angle, ϕ the toroidal angle and q_s the safety factor at the resonance.
The first order of the drift kinetic equation is:

$$v_{\parallel}\boldsymbol{b}\cdot\nabla f_1 + \boldsymbol{v}_d\cdot\nabla f_0 = C(f_1) \tag{5.16}$$

The physics in the non-axisymmetric system is governed by the bounce averaged drift kinetic equation in low collisionality regimes, which eliminates the information along the magnetic field. The bounce average is defined as:

$$\langle\cdot\rangle_b = \oint d\theta(\cdot)\boldsymbol{B}_0/|v_{\parallel}| \Big/ \oint d\theta \boldsymbol{B}_0/|v_{\parallel}| \tag{5.17}$$

For the passing particles the integral is performed between 0 and 2π and for the trapped particles the integral is performed between $-\theta_c$ to θ_c instead where θ_c is the angle defining the boundary between trapped and passing particles. Taking the bounce average of Equation 5.16, $v_{\parallel}\boldsymbol{b}\cdot\nabla f_1$ could be annihilated (see Appendix 7.3) and Equation 5.16 becomes:

$$\langle\boldsymbol{v}_d\cdot\nabla\alpha\rangle_b \frac{\partial f_0}{\partial\alpha} + \langle\boldsymbol{v}_d\cdot\nabla\Psi\rangle_b \frac{\partial f_0}{\partial\Psi} = \langle C(f_1)\rangle_b \tag{5.18}$$

In order to solve Equation 5.18, a subsidiary ordering is adopted:
In the case of $\langle\boldsymbol{v}_d\cdot\nabla\alpha\rangle_b \partial f_0/\partial\alpha \sim \langle C(f_1)\rangle_b > \langle\boldsymbol{v}_d\cdot\nabla\Psi\rangle_b \partial f_0/\partial\Psi$, which implies the drift orbit is much smaller than the characteristic length of the plasma, equation 5.18 yields to:

$$\langle\boldsymbol{v}_d\cdot\nabla\alpha\rangle_b \frac{\partial f_{00}}{\partial\alpha} = \langle C(f_{00})\rangle_b \tag{5.19}$$

And the solution is $f_{00} = f_M$ in the perturbed tokamaks and stellarators. The next order equation in the subsidiary ordering is:

$$\langle\boldsymbol{v}_d\cdot\nabla\alpha\rangle_b \frac{\partial f_{01}}{\partial\alpha} + \langle\boldsymbol{v}_d\cdot\nabla\Psi\rangle_b \frac{\partial f_M}{\partial\Psi} = \langle C(f_{01})\rangle_b \tag{5.20}$$

In order to solve Equation 5.20, the relative strength of the helical drift frequency and the collision frequency should be examined and this brings to the definition of the different collisionality regimes.

- The helical drift frequency is much smaller than the collision frequency. Equation 5.20 reduces to:

$$\langle \boldsymbol{v}_d \cdot \nabla\Psi \rangle_b \frac{\partial f_M}{\partial \psi} = \langle C(f_{01}) \rangle_b \tag{5.21}$$

The bounced averaged radial drift velocity is [101]:

$$\langle \boldsymbol{v}_d \cdot \nabla\Psi \rangle = 8\frac{I}{\Omega}\frac{\partial \Psi}{\partial \psi}\sqrt{\frac{\mu B_0}{M\Delta}}\left(\boldsymbol{E} - \frac{\boldsymbol{K}}{2}\right)\frac{\partial \Delta}{\partial \alpha} \tag{5.22}$$

Where M is the mass, $\boldsymbol{K}$ and $\boldsymbol{E}$ are complete elliptic integrals of the first and second kind, respectively, and $\Delta = \epsilon_s \pm \delta_W(\bar{\Psi} + \cos m\alpha)^{1/2}$ with ϵ_s the inverse aspect ratio evaluated at the resonant surface, δ_w is the island width r_W normalized by the major radius R_0 and $\bar{\Psi}$ is the helical flux function normalized by the perturbed poloidal flux function $\tilde{\psi}$ and B_0 is the magnetic field on the magnetic axis. The argument of the complete elliptic integrals is $\kappa^2 = (E - \mu B_0 - e\Phi + \mu B_0\Delta)/2\mu B_0\Delta$, which is the pitch parameter defining the trapped particles [101]. For particles trapped in the toroidal magnetic mirrors, $\kappa^2 < 1$ and for circulating particles $\kappa^2 > 1$.
With a pitch angle scattering Coulomb collision operator, Equation 5.21 can be easily integrated once to obtain [101]:

$$\frac{\partial f_0}{\partial \kappa^2} = \frac{\mu B_0}{\nu}\Delta\frac{\partial f_M}{\partial \Psi}\frac{IB_0 \cdot \nabla\theta}{M\Omega B_0}\frac{\partial \Psi}{\partial \psi}\frac{\partial \Delta}{\partial \alpha}\frac{\int_0^{\kappa^2} d\kappa^2(2\boldsymbol{E} - \boldsymbol{K})}{[\boldsymbol{E} - (1-\kappa^2)\boldsymbol{K}]} \tag{5.23}$$

The flux surface averaged transport fluxes $\Gamma_p =< N\boldsymbol{V} \cdot \nabla\Psi >_f$ is thus obtained [101]:

$$\Gamma_p = -\frac{C_1}{2}\frac{(I\boldsymbol{n}_0 \cdot \nabla\theta)^2}{M^{7/2}\Omega^2}\left(\frac{q_s'}{q_s}r_w\right)^2 m^2\delta_W\epsilon_s^{3/2}\frac{F(\bar{\Psi})\sqrt{1+\bar{\Psi}}}{K(\kappa_f)}\int dW W^{5/2}\frac{1}{\nu}\frac{\partial f_M}{\partial \Psi} \tag{5.24}$$

Where N is the plasma density, $\boldsymbol{V}$ is the flow velocity, $<>_f$ indicates flux surface average, $C_1 = 0.884$, $W = Mv^2/2$, $F(\bar{\Psi}) = \oint d\alpha(\sin m\alpha)^2(\Delta/\epsilon_s)^{3/2}/\sqrt{\bar{\Psi} + \cos m\alpha}$, $I = RB_t$ and $\kappa_f^2 = 2/(1+\bar{\Psi})$. It is clear to see that the particle flux is inverse proportional to the collision frequency.

- When the collision frequency decreases further,$\langle C(f_{01}) \rangle_b < \langle \boldsymbol{v}_d \cdot \nabla\alpha \rangle_b$, Equation 5.20 reduces to:

$$\langle \boldsymbol{v}_d \cdot \nabla\alpha \rangle_b \frac{\partial f_{010}}{\partial \alpha} + \langle \boldsymbol{v}_d \cdot \nabla\Psi \rangle_b \frac{\partial f_M}{\partial \Psi} = 0 \tag{5.25}$$

And

$$\langle \boldsymbol{v}_d \cdot \nabla\alpha \rangle_b \frac{\partial f_{011}}{\partial \alpha} = \langle C(f_{010}) \rangle_b \tag{5.26}$$

The bounce averaged drift speed in the $\nabla\alpha$ direction is [102]:

$$\langle \boldsymbol{v}_d \cdot \nabla\alpha \rangle_b = -(I/M\Omega)(\partial\Psi/\partial\psi)(\boldsymbol{B}_0 \cdot \nabla\theta/B)(\partial J/\partial\Psi)/(\partial J/\partial E) \tag{5.27}$$

Here E is the particle energy and $J = \oint d\theta v_\parallel$ is the second adiabatic invariant [102]:

$$J = 16(\mu B\Delta/M)^{1/2}\left[\boldsymbol{E}(\kappa) - (1-\kappa^2)\boldsymbol{K}(\kappa)\right] \tag{5.28}$$

Applying Equation 5.28, the helical drift velocity after bounce average is thus [102]:

$$\langle \boldsymbol{v}_d \cdot \nabla\alpha \rangle_b = -(I/M\Omega)(\partial\Psi/\partial\psi)(\boldsymbol{B}_0 \cdot \nabla\theta/B)\left[\mu B(2\boldsymbol{E}/\boldsymbol{K} - 1)\partial\Delta/\partial\Psi - e\Phi'\right] \tag{5.29}$$

Where $\Phi' = \partial\Phi/\partial\Psi$. The radial drift speed after bounce average, neglecting the super banana and trapping-detrapping process, is [102]:

$$\langle \boldsymbol{v}_d \cdot \nabla\Psi \rangle_b = -(I/M\Omega)(\partial\Psi/\partial\psi)(\boldsymbol{B}_0 \cdot \nabla\theta/B)\left[\mu B(2\boldsymbol{E}/\boldsymbol{K} - 1)\partial\Delta/\partial\alpha\right] \tag{5.30}$$

Applying these condition, we could obtain the distribution function f_{010} [102]:

$$f_{010} = -(\mu B_0/e\Phi')(1-\kappa^2)\left[(\pm\delta_W)(\bar{\Psi} + \cos m\alpha)^{1/2} \pm C_1\right]\partial f_M/\partial\Psi \tag{5.31}$$

Where $C_1 = -(\pi/2)(1+\bar{\Psi})^{1/2}/\boldsymbol{K}(\kappa_f)$ is the integration constant. The corresponding particle flux is [102]:

$$\Gamma_p = -(\pi/\langle g^{1/2}\rangle)\int d\alpha \int dE(\nu q_s/MB\Delta)[(\partial\Psi/\partial\psi) \times (\boldsymbol{B}_0 \cdot \nabla\theta/B)\partial f_M/\partial\Psi]^{-1}\int_0^1 d\kappa^2 J(\partial f_0/\partial\kappa^2)^2 \tag{5.32}$$

With $\langle g^{1/2}\rangle = \int d\theta \int d\alpha/\nabla\Psi \times \nabla\alpha \cdot \nabla\theta$. The particle flux now is proportional to the collision frequency.

5.3 Summary

At this point, we have already obtained the formula of particle fluxes in tokamak configurations, considering the presence of magnetic islands under the main assumptions of neglecting super banana effect. The Equation 5.24 and 5.32 are the particle

flux functions obtained in $1/\nu$ and ν regimes, respectively. These two equations contain complex integrals, which bring difficulties to perform further study. In Chapter 6, the simplified equations, based on the cylindrical approximation are presented. In such a way, the particle fluxes are expressed with a monotonic radial coordinate so that further transport study on 1.5 dimensions could be carried out. The justification of applying these equations originally developed for tokamaks on stellarators is discussed. An combined equation which could well reproduce the three low collision regimes is presented and the transport study with this model, using the TJ-II stellarator parameters is presented.

6

Modification on Radial Electric Field due to Magnetic Islands in TJ-II Stellarator

TJ-II stellarator is capable of reaching high confinement mode, through the L-H transition process. It is believed that the L-H transition is motivated by the shear of $\boldsymbol{E} \times \boldsymbol{B}$ flow. Hence, the radial electric field rises an important role in toroidal confinement research. In chapter 5, non-intrinsically ambipolar particle fluxes in the vicinity of a magnetic island have been written, following Shaing's analytical theory. In particular, the calculations for both the ν and $1/\nu$ low collisionality regimes have been shown. In this chapter we use these results, adding also the $\sqrt{\nu}$ regime, to study how small magnetic islands can modify the TJ-II stellarator ambipolar electric field, in the framework of neoclassical theory. Shaing's analytical calculations have been developed for the simplified tokamak configuration. We use almost the same equations to model the dependence of the fluxes to the radial electric field, but using the TJ-II stellarator parameters. A justification for this will be given in the text.

6.1 Radial Electric Field and Magnetic Islands in TJ-II

TJ-II stellarator is capable of reaching high confinement mode (H-mode), in which the plasma confinement properties are highly enhanced. The first H-mode was discovered in ASDEX tokamak [103] and afterwards it was identified that the shear of $\boldsymbol{E} \times \boldsymbol{B}$ flow is the key component for reducing the turbulence that produces large confinement losses and the formation of transport barriers [93]. In TJ-II configuration, it has also been identified that this sheared flow plays an important role in L-H transition [104]. This rises the importance of radial electric field in stellarators within the framework of neoclassical transport, which is the physical mechanism responsible for the radial electric field due to the non-ambipolar particle fluxes [105]. Several studies on radial electric field have been performed in TJ-II stellarator. The Monte-Carlo simulations in Electron Cyclotron Heating (ECRH) plasmas show that positive radial electric fields appear in the plasma core and negative radial electric

fields appear in the plasma edge [106]. Further experimental study reveals that the magnetic resonances plays an important role in modifying the local radial electric field [65]. From the theoretical point of view, however, the neoclassical transport simulations in TJ-II have not included the effect induced by the magnetic islands. Hence, this chapter presents the study of the modification effect on the radial electric field in TJ-II plasmas induced by the presence of the magnetic islands.
The study on the modification effect of the radial electric field induced by the presence of the magnetic islands is based on the NTV theory developed by K. C. Shaing [63], originally devoted to tokamak configurations. A brief description of this theory is presented in Chapter 5. The main idea is that the existence of magnetic islands distorts the nested flux surfaces, leading to a modification of the toroidal plasma viscosity, which in turn, modifies the local particle fluxes, giving rise to the local electric field. This effect shares the same physics for all toroidal magnetic configurations with the possession of nested flux surfaces, both in tokamaks and stellarators and consequently, the same effects can be introduced in stellarator plasmas by the presence of magnetic islands.
To begin the study, firstly a brief description of magnetic configurations as well as the magnetic islands in TJ-II is presented. Two typical ι profiles, characterized by two different resonant locations of the two resonance n/m=8/5 and n/m=5/3 (with n=toroidal mode number and m=poloidal mode number), are shown in Figure 6.1. The ι profile in TJ-II is nearly flat. Secondly, there are three points which should be clarified in order to justify the validation of Shaing's theory in stellarators:

- First of all, we assume that the contribution to the non-intrinsically ambipolar particle fluxes in stellarators is due to a mechanism similar to tokamaks: there is an added symmetry breaking effect that alters collisional fluxes from their background in the absence of the islands.

- Secondly, the neoclassical transport particle flux in stellarators is much higher than in tokamaks. This is true for stellarators with no transport optimization [107]. The reason for this phenomenon is that in stellarators, transport related to the trapped particles is much higher than ones in tokamaks because there is no toroidal symmetry. Nevertheless, it is also worth mentioning that the optimized stellarators can have lower neoclassical transport level than ones in tokamaks [107]. TJ-II is a stellarator with no transport optimization so that the particle diffusivity is much higher than one in tokamaks. Tokamak diffusivity due to the islands are very small compared with the neoclassical stellarator background. As we will see later, tokamak diffusivity from Shaing's theory have been multiplied by a geometrical factor $\mathscr{G} = 1000$. This factor is

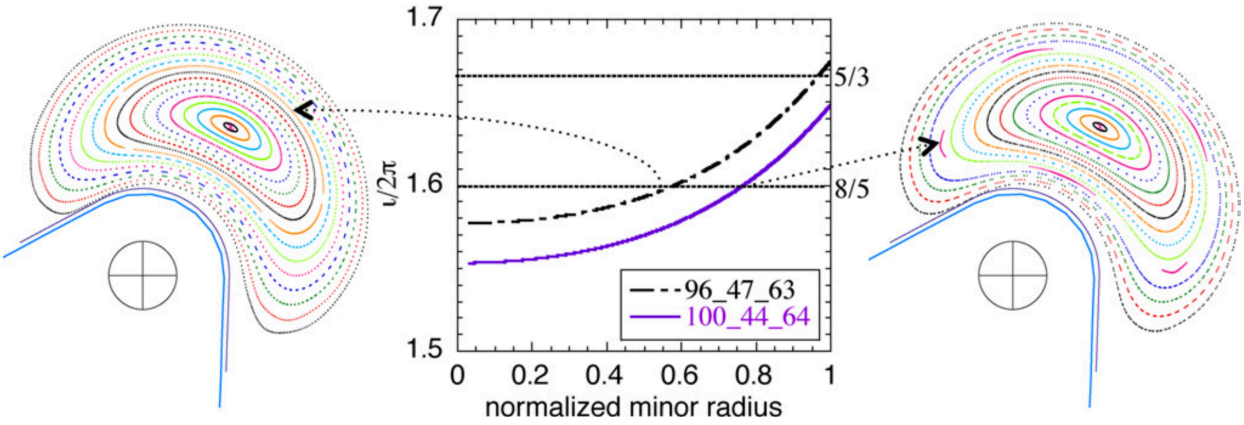

Figure 6.1: Cross section of the vacuum flux surfaces in two magnetic configurations of the TJ-II Heliac and corresponding ι profiles. The resonance $\iota = 8/5$ is located in $\rho = 0.56$ in configuration labeled 96_47_63 (left), while it shifts to $\rho = 0.76$ in configuration 100_44_64 (right). The circled crosses indicate the section of the central conductors, which are protected from the plasma by the hard core. This figure is from Reference [65].

chosen to have comparable contributions to the diffusivity from the background and the island. Another point should be made is that this factor $\mathscr{G} = 1000$ used in this dissertation is the same for both electron and ion particle fluxes, which is a rough assumption. A more detailed work should be performed to find different factors for electron and ion particle fluxes.

- And finally, Shaing's theory, developed for tokamaks, refers to particles trapped in banana orbits, excluding the formation of other trapped orbits, such as super-bananas. The super-banana is caused by local trapped particles due local magnetic mirrors. Particles trapped in the super-banana cannot explore the whole magnetic field. Instead, they are trapped either on the high field surfaces (upper surfaces) or on the low field surfaces (lower surfaces). Such situation will let them directly drift out. In stellarators, local magnetic mirrors commonly exists, which is shown in Figure 6.2. Nevertheless, here we still use Shaing's equations considering that the modification of the fluxes involves particles that can explore the modification of the magnetic field due to the perturbation δB. Resonant perturbations are long wave length perturbations so that they are 'difficult' to be 'seen' by locally trapped particles, and because of this we are

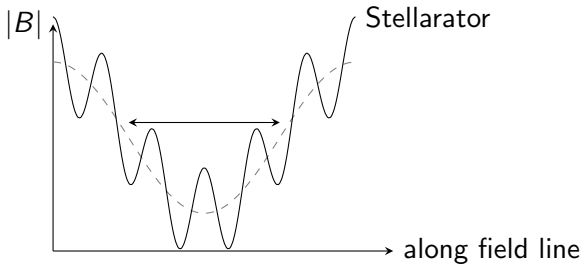

Figure 6.2: Magnetic field strength $|B|$ in tokamaks (dashed line) and stellarators (solid line) along field line is presented. There are many local magnetic mirrors in stellarators.

confident with Shaing's model, at least for a first study. Nevertheless, it should be checked in the future.

With these three assumptions, the detailed study of modification on radial electric field induced by magnetic islands in TJ-II is presented in the following sections. In Section 6.2 and Section 6.3, the complete particle flux equation who can describe the three low collisionality regimes is presented and the validation of this equation is discussed. In Section 6.4, a detailed study on the complete flux equation under equilibria condition is presented, focused on the radial electric field. The modification on the radial electric field due to different plasma parameters has been studied and discussed. And finally, the study of modification on radial electric field due to the presence of magnetic islands in both 'tokamak'[1] and TJ-II configurations is presented, using the code ASTRA.

6.2 Particle Fluxes in Low Collisionality Regimes: ν and $1/\nu$

From here on, we discuss the particle flux equations derived by Shaing, in cylindrical geometry. As mentioned in Chapter 2, there are mainly three sub-regimes in the low collisionality regime: ν, $\sqrt{\nu}$ and $1/\nu$. For ν and $1/\nu$ regimes, the particle flux

[1]This is not really a tokamak case because the experimental plasma parameters used here is from TJ-II experiments. Nevertheless, the use of Shaing's formula can be considered to be a tokamak case since the formula only considers the magnetic field in tokamaks.

equations have been presented in Chapter 5, being Equation 5.32 for ν regime and Equation 5.24 for $1/\nu$ regime. The corresponding simplified two equations have also been presented by Shaing which could well describe the particle flux Γ_p in those two collisionality regimes [108] :

$$\Gamma_p^{\nu} = -D_{11}C = -C(0.22N\nu)\left(\frac{eT}{eBr}\right)^2\left(\frac{\delta_W}{\omega_E}\right)^2\epsilon^{-1/2}G(\bar{\Psi}) \tag{6.1}$$

$$\Gamma_p^{1/\nu} = -D_{11}C = -C0.5\left(\frac{N}{\nu}\right)\left(\frac{eT}{eBr}\right)^2(R_0B_P)^2\left(\frac{q_s'r_W}{q_s}\right)^2(m\delta_W)^2\epsilon^{3/2}H(\bar{\Psi}) \tag{6.2}$$

With the common factor C, related to the density gradient, is defined as $C = (P'/P + e\Phi'/T)$, assuming $T'/T = 0$ because here we only consider the convertinal particle flux, i.e., $\Gamma_p = -D_{11}\nabla N$. The superscript ν and $1/\nu$ indicate the different collision regimes. The basic quantities are: N is the electron density, ν is the collision frequency, c is the speed of light, T is the electron temperature, $P = NT$ is the plasma pressure, Φ is the electric potential and e is the electron charge. $\Phi' = d\Phi/d\Psi$ where Ψ the helical flux function functional as the radial coordinate. B is the magnetic field, B_P is the poloidal component of the magnetic field, a is the minor radius, R_0 is the major radius, m is the poloidal mode number. $r_W = \sqrt{2q_s^2\tilde{\psi}/(q_s'Br_s)}$ is the island width with q_s the safety factor at the resonance, $\tilde{\psi}$ the perturbed equilibrium poloidal flux function, $q_s' = dq/dr|_{r=r_s}$ evaluated at the resonance position r_s with r the effective radius centered in the magnetic axis, $\delta_W = r_W/R_0$, $\omega_E = cE_\Psi/(Br)$ is the $E \times B$ angular speed with $E_\Psi = -d\Phi/d\Psi$, $\epsilon = a/R_0$ is the reversed aspect ratio and $P' = dP/d\Psi$. The function $G(\bar{\Psi})$ is related to the first and second elliptical integrals and essentially it is a function that defines the location of the island region. Hence, for simplicity reason, we use a Gaussian distribution function to replace it. The same technique is applied for the $H(\bar{\Psi})$ function and $X(\bar{\Psi})$ functions which is introduced later.
Equation 6.1 and Equation 6.2 can be unified into a 'combined' equation [108] :

$$\Gamma_p = -D_{11}C = -C\frac{N\,(cT/eBr)^2\,(\nu/\epsilon)(R_0B_P)^2(q_s'r_W/q_s)^2(m\delta_W)^2\epsilon^{1/2}}{\omega_E^2(RB_P)^2(q_s'r_W/q_s)^2m^2/[0.22G(\bar{\Psi})] + (\nu/\epsilon)^2/[0.5H(\bar{\Psi})]} \tag{6.3}$$

Equation 6.3 can well reproduce Equation 6.1 and 6.2 in the limit $\nu \to 0$ and $\nu \to \infty$, respectively. Applying Equation 6.3 with typical TJ-II plasma parameters shown in Table 6.1, one could see the result of reproduction from Figure 6.3. The two graphs are the log-log scale plots of particle diffusivity $D_{11}^{i(e)}$ versus the collisionality ν^*. The

Quantity	Value
N(m^{-3})	0.36×10^{19}
$T_e(eV)$	350
$T_i(eV)$	$T_e/3$
$B_T(T)$	0.995
B(T)	1
R_0(m)	1.5
a(m)	0.2
m	5
n	8
q	$1/[1.551 + 0.05238r/a - 0.07569(r/a)^2 + 0.12862(r/a)^3]$

Table 6.1: Typical TJ-II plasma parameters.

superscript i and e represent ions and electrons. The black and blue dashed lines are for ν and $1/\nu$ regimes obtained from Equation 6.1 and Equation 6.2, respectively . The black gray vertical lines represents the boundary between ν and $1/\nu$ regimes. The thine vertical red and blue lines represent the collisionality ν^* of ions and electrons in such plasma parameters, respectively. The red curves are produced by Equation 6.3. The results show a good agreement between Equation 6.1, 6.2 and Equation 6.3.
The boundary between ν and $1/\nu$ (gray vertical line in Figure 6.3) is defined as [102]:

$$\nu_{\text{eff}} < \omega_E(R_0 B_P)(q_s' r_W/q_s) \tag{6.4}$$

Where $\nu_{\text{eff}} = \nu/\epsilon$ is the effective collision frequency defined as the ration between the collision frequency ν and the inverse aspect ratio ϵ.

6.3 Particle Flux in $\sqrt{\nu}$ Regime and the Complete Particle Flux Equation

The Equation 6.3 presented above only covers two low collision regimes. In order to get a complete equation for the particle flux including all three low collision regimes, the study on the the $\sqrt{\nu}$ regime is presented. Applying the equation from Reference [109], we could get the particle flux equation for $\sqrt{\nu}$ regime:

$$\Gamma_p^{\sqrt{\nu}} = -D_{11}C = -C0.1\sqrt{\nu}\,(cT/eBr)^2\,\delta_W^2\sqrt{B_P R_0 m}\,(-q_s' r_W/q_s)^{0.5}\,|\omega_E|^{-1.5}\,X(\bar{\Psi}) \tag{6.5}$$

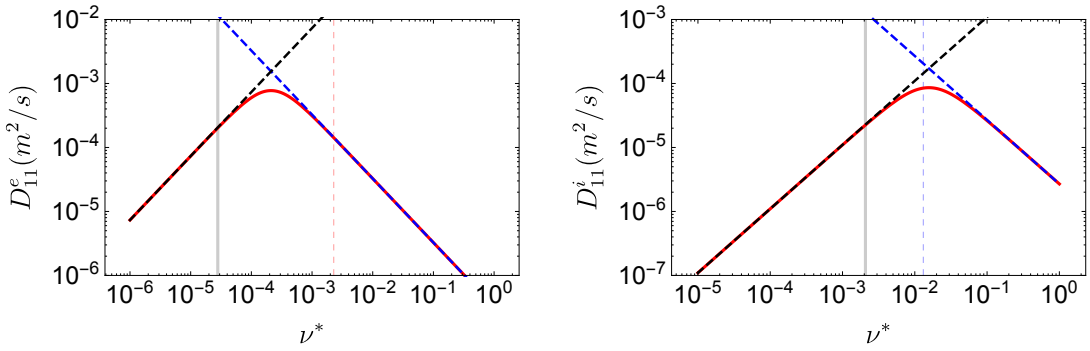

Figure 6.3: Using TJ-II parameters, the combined function(in red) could well reproduce the two separated functions in ν(dashed black line) and $1/\nu$(dashed blue line) regimes. The thick gray vertical line represents the critical ν^* which indicates the end of ν regime. The red vertical dashed line is the electron collisionality and the blue dashed one is the ion collisionality.

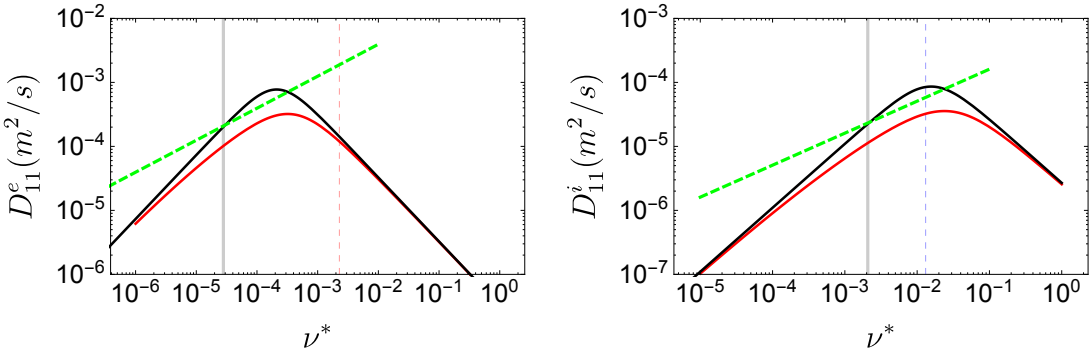

Figure 6.4: Comparison between equation 6.3(black, solid) and equation 6.6(red, solid). The dashed green line represents the $\sqrt{\nu}$. It is clear to see that the green line and black line has a common point which also belongs to the gray vertical line which is the end of ν regime. The vertical red and blue dashed lines are the collisionality for electrons and ions, respectively.

The superscript $\sqrt{\nu}$ indicates that the particle flux is in $\sqrt{\nu}$ regime. In order to write a combined complete equation for the three low collisionality regimes, for simplicity reason, we simplify the three separate particle flux functions as:

$$\Gamma_p^{\nu} = -D_{11}C = -CK_{\nu}\nu$$
$$\Gamma_p^{\sqrt{\nu}} = -D_{11}C = -CK_{\sqrt{\nu}}\sqrt{\nu}$$
$$\Gamma_p^{1/\nu} = -D_{11}C = -CK_{1/\nu}1/\nu$$

And the corresponding coefficient K_{ν}, $K_{\sqrt{\nu}}$, $K_{1/\nu}$ are defined as:

$$K_{\nu} = 0.22N(cT/eBr)^2(\delta_W/\omega_E)^2\epsilon^{-1/2}G(\bar{\Psi})$$
$$K_{\sqrt{\nu}} = 0.1\,(cT/eBr)^2\,\delta_W^2\sqrt{R_0B_Pm}\,(q_s'r_W/q)^{0.5}\,|\omega_E|^{-1.5}\,X(\bar{\Psi})$$
$$K_{1/\nu} = 0.5N(cT/eBr)^2(R_0B_P)^2(q_s'r_W/q_s)^2(m\delta_W)^2\epsilon^{3/2}H(\bar{\Psi})$$

Using these notations, we present the complete particle flux equation for $\nu^* < 1$ regime, including ν, $\sqrt{\nu}$ and $1/\nu$ regimes:

$$\Gamma_p = -C\frac{K_{\nu}K_{\sqrt{\nu}}K_{1/\nu}\cdot\nu}{(K_{\sqrt{\nu}} + K_{\nu}\cdot\sqrt{\nu})(K_{1/\nu} + K_{\sqrt{\nu}}\cdot\nu^{1.5})} \tag{6.6}$$

Before putting this new equation into practice, one need to justify that it could well reproduce Equation 6.3 from literature and also it could well describe the 'new' regime, being the $\sqrt{\nu}$ regime introduced here. The comparison between Equation 6.3 and 6.6 is shown in Figure 6.4. The green dashed line represents the $\sqrt{\nu}$ regime and it shares one common point with the black solid line from Equation 6.3 and the gray vertical line from Equation 6.4. This common point shared by the three curves indicates that the $\sqrt{\nu}$ regime starts from the point where ν regime stops. The red solid line is from Equation 6.6. The results show that the three low collisionality regimes are well described by Equation 6.6. Note Equation 6.6 is derived from tokamak configurations and the proper application of this equation in stellarator configurations needs to be justified.

Unit Analysis

The complete flux equation mentioned above is derived from the general definition of particle fluxes: $\Gamma_p = \langle NV\cdot\nabla\Psi\rangle$ with $\langle\cdots\rangle$ represents the flux surface average and V is the flow speed. This definition leads to a different flux unit $[B]/(lt)$ since $\nabla\Psi$ has a unit of $[B]l$ which is different from 1. Here l is the unit of length, t is the unit of time

and $[B]$ indicates the unit of magnetic field. Secondly, the three partial differentials $P' = dP/d\Psi$, $\Phi' = d\Phi/d\Psi$ and $E_\Psi = -d\Phi/d\Psi$ have units which do not have the conventional physical meaning. So here one coordinate transformation is needed to convert the equations in order to use the physical quantities with international units. To overcome this issue, one may assume a cylindrical model for the island, where the angular part is neglected:

$$\nabla\Psi = \partial\Psi/\partial r\nabla r + \partial\Psi/\partial\theta\nabla\theta + \partial\Psi/\partial\phi\nabla\phi \sim \partial\Psi/\partial r\nabla r \tag{6.7}$$

Using the equilibrium poloidal flux $\Psi_P(r)$, this can be written in the form:

$$dr/d\Psi = (dr/d\Psi_P)(d\Psi_P/d\Psi) = [(2\pi B_P R_0)(q_s' r_W/q_s)]^{-1} \tag{6.8}$$

Note that this 'extra' step is due to the choice of coordinate [101]. Applying this technique, the following quantities are obtained:

$$\omega_{E_\Psi} = (dr/d\Psi)\omega_{E_r} \tag{6.9}$$
$$\Gamma_{p,\Psi} = (dr/d\Psi)\Gamma_{p,r} \tag{6.10}$$
$$\Phi' = d\Phi/d\Psi = (dr/d\Psi)d\Phi/dr \tag{6.11}$$
$$C = (dr/d\Psi_P)(1/P \cdot dP/dr + 1/T \cdot d\Phi/dr) \tag{6.12}$$

Where $\omega_{E_r} = cE_r/Br = -(c/Br)(d\Phi/dr)$, $\Gamma_{p,\Psi}$ is the particle flux with unit of $[B]/(lt)$ and $\Gamma_{p,r}$ is the particle flux with unit of $1/(l^2 t)$. Therefore, the three coefficients K_ν, $K_{\sqrt{\nu}}$ and $K_{1/\nu}$ are:

$$K_\nu = 0.22(dr/d\Psi)^{-2} N (cT/eBr)^2 (\delta_W/\omega_{E_r})^2 \epsilon^{-1/2} G(\bar{\Psi}) \tag{6.13}$$
$$K_{\sqrt{\nu}} = 0.1(dr/d\Psi)^{-1.5} (cT/eBr)^2 \delta_W^2 \sqrt{R_0 B_P m} (q_s' r_W/q)^{0.5} |\omega_{E_r}|^{-1.5} X(\bar{\Psi}) \tag{6.14}$$
$$K_{1/\nu} = 0.5N(cT/eBr)^2 (R_0 B_P)^2 (q_s' r_W/q_s)^2 (m\delta_W)^2 \epsilon^{3/2} H(\bar{\Psi}) \tag{6.15}$$

Applying those new expression into Equation 6.6, the part $(q_s' r_W/q)$ disappears in those three coefficient. The complete equation, with the correct physical unit is thus obtained.

Validation of The Complete Particle Flux Equation

Remind that differently from axi-symmetric tokamaks, in stellarator equilibrium configurations the ambipolar electric field is not necessarily zero. The idea is to add an 'extra' contribution to non-ambipolar fluxes induced by the magnetic islands. Equation 6.6 is the corresponding one to describe this extra contribution. Before

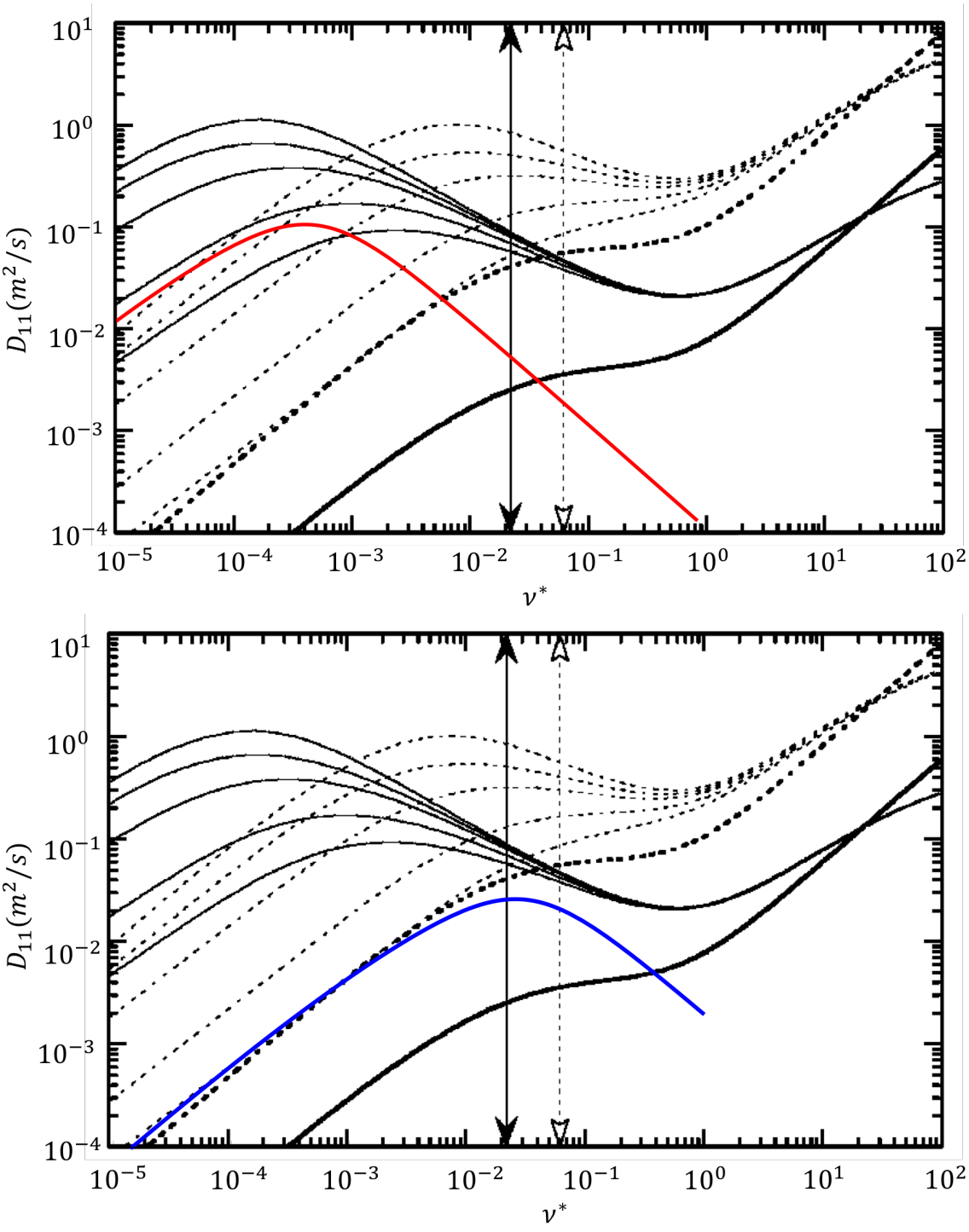

Figure 6.5: Comparison between Equation 6.6 multiplied by the geometry factor $\mathscr{G} = 1000$ (colored lines with $|E_r| = 2300V/m$) and the TJ-II data, which is the black background figure from Ref [106]. The solid black lines are for electrons and the dashed ones are for ions. From top to bottom the lines are generated with the conditions $e\Phi/T = 0, 1, 2, 5, 10$. The thick solid and dashed black lines are corresponding curves to the equivalent tokamak. The red and blue lines represents electrons and ions, respectively.

applying this equation to TJ-II work, it is important to compare the typical particle diffusivity in TJ-II with the magnetic island one described by Equation 6.6. Using the Figure in Reference [106] as the standard TJ-II $D_{11} - \nu^*$ diagram and applying the same plasma parameters in Equation 6.6, the comparison is obtained and shown in Figure 6.5. The black 'background' figure is from Reference [106]. The red line represents electrons and the blue line represents ions. Note that the geometry factor $\mathscr{G} = 1000$ has been multiplied to Equation 6.6 to include a rough estimation on the contribution of the stellarator geometry in Shaing's theory. The result shows that a factor of 1000 to tokamak equations allows particle diffusivity due to the magnetic island to be comparable to the TJ-II equilibrium non-ambipolar particle fluxes. We believe that this justifies the usage of Equation 6.6 for further study on TJ-II plasmas.
Note that this factor $\mathscr{G}$ used here has the same value for both electron and ion particle fluxes. This is a rough assumption because it fits both ions and electrons well in the comparison results presented above. Analytical solutions should be developed in further study to justify this point. Nevertheless, here we assume this factor is the same for both ions and electrons.

6.4 Discussions on the Complete Particle Flux Equation

The complete particle flux in low collisionality regime has been presented and the justification on the validation in TJ-II configuration is made, adopting a geometry factor $\mathscr{G}$. With finalization of these analytical work, now we move to the study on the non-ambipolar particle fluxes, varying some plasma parameters. This section presents the study of ambipolar electric field in different plasma parameters.

Validation of the collision frequency regime

The NTV theory is derived to describe the "low" collision frequency regime, meaning the $\nu^*_{i,e} = \nu_{i,e}/\omega_{b,(i,e)} < 1$ with ν the collision frequency, $\omega_b = v_{th}/qR_0$ the bounce frequency and v_{th} the thermal speed of charged particles. This condition leads to temperature limits in both electrons and ions:

$$T_e > 2.22 \times 10^{-9} \sqrt{N_e \ln \Lambda_e} \tag{6.16}$$

$$T_i > 1.86 \times 10^{-9} Z^2 \mu^{-1/4} \sqrt{N_i \ln \Lambda_i} \tag{6.17}$$

With electron collision frequency $\nu_e = 2.91 \times 10^{-12} N_e \ln \Lambda_e T_e^{-3/2}$ and ion collision frequency $\nu_i = 4.80 \times 10^{-14} Z^4 \mu^{-1/2} N_i \ln \Lambda_i T_i^{-3/2}$. Z is the ion charge, $\mu = m_i/m_p$ where m_i is the ion mass expressed in the proton mass m_p. $\ln \Lambda_{e,i}$ is the Coulomb logarithm for electrons (e) and ions (i). Given the Coulomb logarithm does not change much in relatively narrow plasma parameters, it is clear to see that the ion and electron temperature have low limits with respect to a given plasma density. In the following sections, these two limits are always checked when other plasma parameters vary.

Scan of the E_r

The particle flux is a function of the radial electric field E_r. In order to get a better understanding on how the radial electric field affects the particle diffusivity, a scan of the E_r is performed and the results are shown in Figure 6.6 based on a typical TJ-II plasma presented in Table 6.1. The upper graph is the scan on electrons and the lower one is on ions. The different thin vertical lines represents the different values of ν_{eff} with different colors representing the different value of E_r, which is shown in the legend. The thick vertical dashed red line in the upper graph and the thick vertical dashed blue line in the lower graph represents the values of electron collisionality and the ion collisionality. Several results could be interpreted from these two plots. First of all, all the scans share the same $1/\nu$ line. This is true because one could see from Equation 6.2 that the particle flux does not depend on the radial electric field in $1/\nu$ regime. Secondly, as the radial electric field increases, the ν regime moves towards higher collision regions and at some point, the $\sqrt{\nu}$ and $1/\nu$ regimes might vanish, left only the ν regime.

Effect on radial electric field E_r from different plasma parameters

After investigating the effect of radial electric field on the particle fluxes, now we begin to study how different plasma parameters could effect the radial electric field.

$q_s' r_W / q_s$. This parameter is not in the particle flux equation, as one could see from the discussions on the unit analysis. So in principle the variation of this parameter does not affect the particle flux. However, the island width r_W is a function of q_s'. If the magnetic island width r_W is fixed, then particle diffusivity D_{11} does not depend on the parameter $q_s' r_W / q_s$. Therefore, changing this parameter will lead to the same D_{11} and E_r. The reason why this parameter

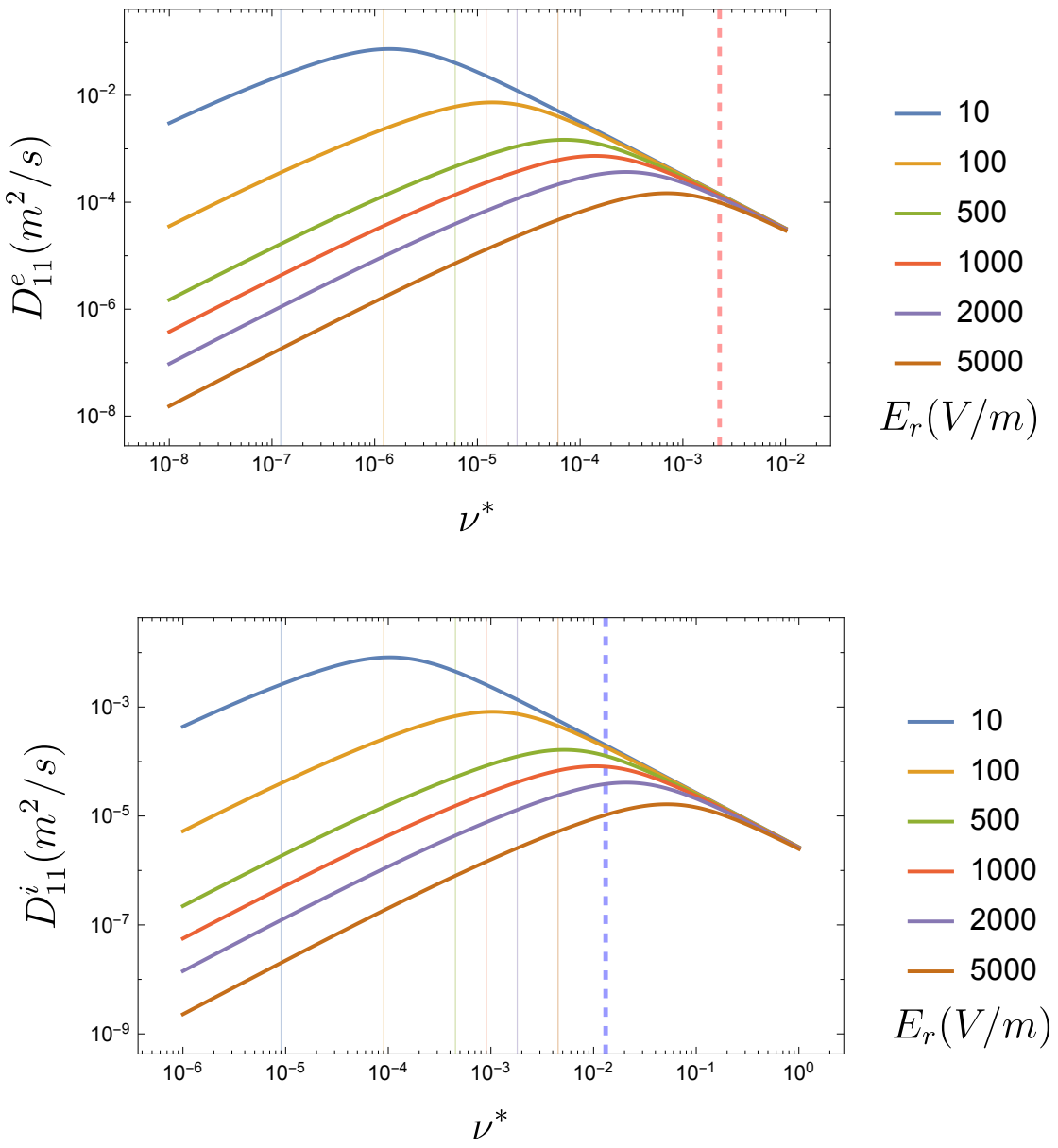

Figure 6.6: Radial electric field E_r scan in a typical TJ-II plasma. The upper graph is the scan on electrons and the lower one is on the ions. The red thick vertical dashed line in the upper graph is the electron collisionality and the blue thick vertical dashed line in the lower graph is the ion collisionality. The thin vertical lines represent the value of $\nu_{\text{eff}}/\omega_b$ with different electric field.

is irrelevant to both D_{11} and E_r is because it comes from the choice of the flux coordinate system and when we calculate the particle fluxes, one should convert back to machine coordinate. By doing so, this factor disappears.

Island Width r_W. As one could see from Equation 6.6, the island width, which is inside of $\delta_W = r_W/R$, is a universal parameter of the particle flux. The three coefficients $K_{\nu,\sqrt{\nu},1/\nu}$ have common dependence on δ_W, which justifies the comment before. Hence, the island width could only affect the absolute value of the separated particle flux in each collisionality regime while as for the radial electric field E_r which is the root of equation of $\Gamma_{p,e} = \Gamma_{p,i}$, it is independent of the island width and this is confirmed by the simulation results.
Nevertheless, it is worth to point out that the width of the island, in principle should affect the function $G(\bar{\Psi})$, $H(\bar{\Psi})$ and $X(\bar{\Psi})$ because these three functions describe the location as well as the width of the island. In the previous section, these three functions are simplified to Gaussian functions to ease the simulation task. So if the width of the island increases, these three functions should be modified accordingly to keep the modification consistent.

Poloidal Mode Number m. The poloidal mode number, especially the low m number, in principle, should have big impact on the radial electric field [102]. Here the impact of poloidal mode number is investigated. The poloidal mode number is functional when the collision frequency is in the $\sqrt{\nu}$ or $1/\nu$ regimes, as one could see from the diffusivity equations. The simulations are performed on the same TJ-II plasma parameters used before and the result is shown in Figure 6.7, where $\Gamma_e - \Gamma_i$ is plotted as a function of the radial electric field E_r. The zero values of this function are the possible values of the ambipolar electric field. One can see that changing the mode number does not change the value of the radial electric field. This peculiar result encouraged us to study further on this point and it is found out that the reason for this phenomenon is that the electric field in these three calculations are around -300 V/m. Using this value to back check in Figure 6.6, we find that roughly both electrons and ions are all in $1/\nu$ regime. In this case, the radial electric field is essentially obtained by $P_e'/P_e + e\Phi'/T_e = P_i'/P_i + Z\Phi'/T_i$. Consequently, the poloidal mode number doesn't play a role in the charge balance equation with the plasma parameters of Table 6.1.

Scan of T_i. This section is dedicated to investigating the effect of ion temperature T_i on the radial electric field. The exercises have been performed based on the same plasma parameters presented in Table 6.1. The value of

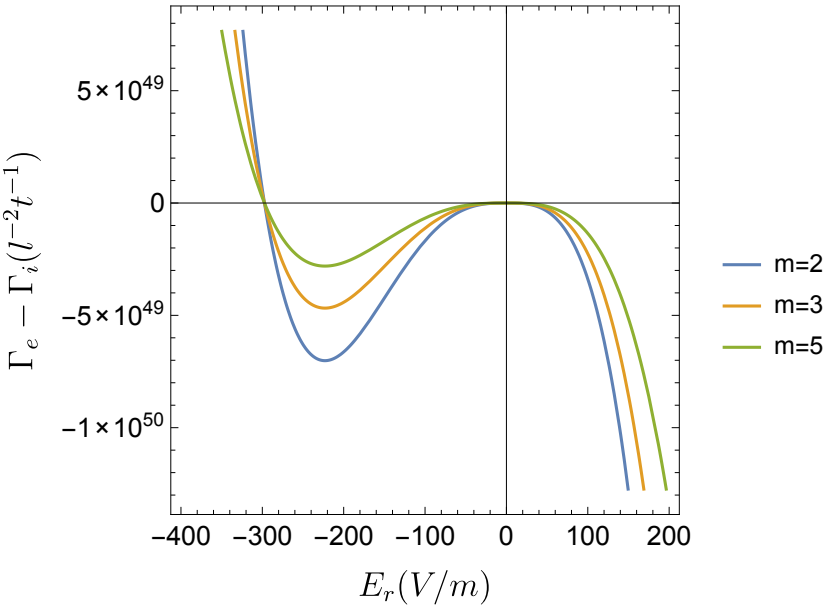

Figure 6.7: The value of function $\Gamma_e - \Gamma_i$ is plotted as a function of the radial electric field E_r, applying three different poloidal mode number, being m=2, 3, 5. The zero value of such function is the possible solution of the radial electric field. This plot is generated using the plasma parameter listed in Table 6.1.

$\Gamma_{p,e} - \Gamma_{p,i}$ is plotted as a function of both E_r and T_i, shown in Figure 6.8. The contour line which has the value of zero is where the root(s) of equation $\Gamma_{p,e} - \Gamma_{p,i} = 0$ lay on, i.e., the solution of ambipolar electric field. At the region $T_i < 105$eV, there is one single, positive ambipolar electric field root. When ion temperature increases between 105eV and 250eV, three ambipolar electric fields appear with the middle one usually the unstable one [105]. And in the region with $T_i > 250$eV, one single, negative ambipolar electric field appears. Moreover, one special point, which is around $T_i = 105$eV should be pointed out. At this point, the electric field is zero, meaning the fluxes $\Gamma_{p,e} = \Gamma_{p,i}$ fulfill the ambipolar condition. This phenomenon is further studied below.

Scan of T_i/T_e. Following the study of ion temperature, now we make scans on both electron and ion temperatures and we calculated the value of ambipolar electric field, by solving the charge balance equation $\Gamma_{p,e} = \Gamma_{p,i}$. The result of these scans are shown in Figure 6.9. There is a vertical contour line with its value $E_r = 0$ around $T_i/T_e \approx 0.3$. This means ambipolar fluxes are generated

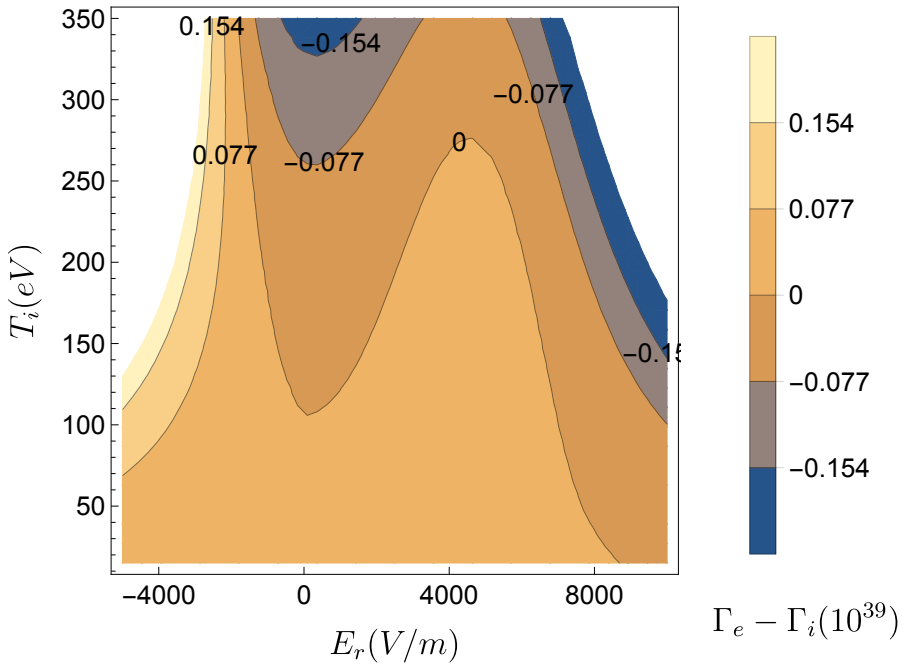

Figure 6.8: The solution for electric field under steady state assumption. The plasma parameters used in this calculation are presented in Table 6.1 with electron temperature modified to 350 eV. The contour line with $E_r = 0$ is the solution for ambipolar conditions. With ion temperature below 105 eV, single positive electric field appears. As the ion temperature increases, three electric field solutions, one negative and two positive, appear. The middle solution is unstable [105]. And finally, when the ion temperature increases above 250 eV, single negative ambipolar electric field appears.

in vicinity of magnetic islands under the condition of $T_i/T_e = 0.3$. This can be easily proved. Let us take the charge balance equation $\Gamma_{p,e} = \Gamma_{p,i}$ with the condition of $E_r = 0$. One could easily get the solution:

$$(T_i/T_e)^{7/2} \approx 60.42\,(\ln\Lambda_e/\ln\Lambda_i) \tag{6.18}$$

where $\ln\Lambda_e$ and $\ln\Lambda_i$ are the Coulomb logarithm for electrons and ions, respectively. The value of $\ln\Lambda_e/\ln\Lambda_i$, despite of depending on the value of electron and ion temperature as well as the plasma density, has tiny change around the value 1.1. So the solution to $\Gamma_{p,e} = \Gamma_{p,i}$ with $E_r = 0$ is $T_i/T_e \approx 0.3$. This confirmed the observation of $E_r = 0$ around $T_i = 105$ eV in Figure 6.8. In that case, the ratio $T_i/T_e = 105/350 \approx 0.3$.

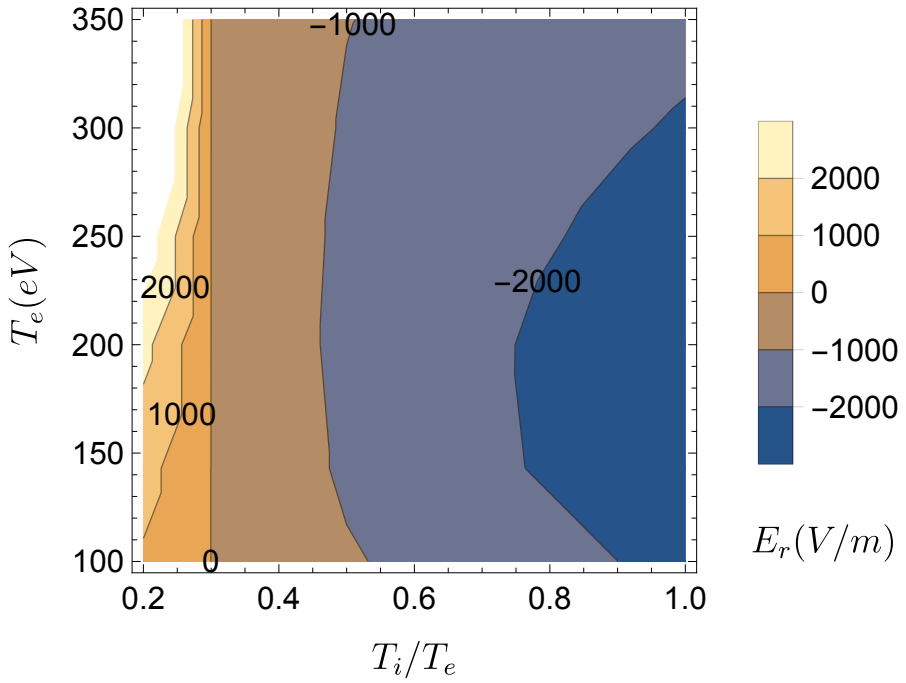

Figure 6.9: The solution for electric field under steady state assumption. The plasma parameters used in this calculation are presented in Table 6.1. With a fixed electron temperature, the solution of ambipolar electric field is positive in low ratio of $T_i/Te < 0.3$ and negative in high ratio of $T_i/T_e > 0.3$. When the ratio between ion and electron temperature equals 0.3, the ambipolar electric field equals zero, which is shown as the vertical line at T_i/T_e.

Plasma Density n. As the plasma density increases a factor of 50%, one root solution appears in all T_i/T_e region, which is shown in Figure 6.10. The same $E_r = 0$ point appears around $T_i/T_e \approx 0.3$, which is the same point as the one in Figure 6.8.

From the discussion above, we know that the ambipolar electric field becomes to zero when $T_i/T_e \approx 0.3$. This results shows that the modification effect due to magnetic islands disappears and the particle fluxes are ambipolar. What is more, if we increase the ratio between ion and electron temperature, the electric field changes its sign from positive to negative and its amplitude also increases (neglecting the unstable ones in the middle). This is true because getting closer to the plasma edge, the ratio between ion temperature and electron temperature becomes bigger. In both

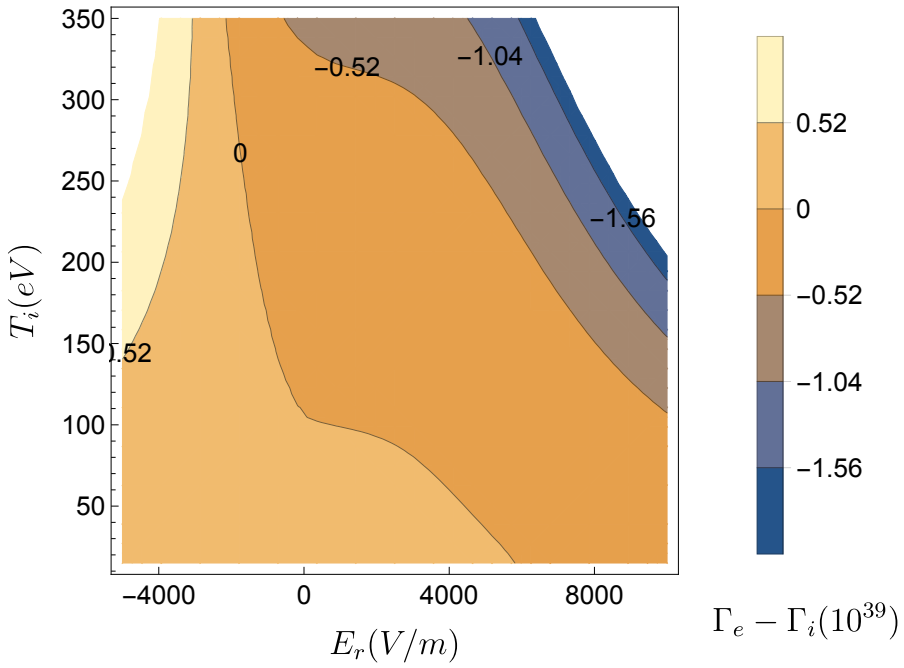

Figure 6.10: The solution for electric field under steady state assumption. The plasma parameters used are presented in Table 6.1 with 150% plasma density. At all ion temperatures, the ambipolar electric field only has one solution, as indicated by the 0 contour line. When the ion temperature is below 100 eV, the ambipolar electric field is positive and above this value, it is negative.

References [65, 106] the positive radial electric field and negative radial electric field have been reported, which confirms the conclusions we obtained. Finally, the plasma density also plays a role of island modification effect. The unstable ambipolar electric field region disappears with an increase of plasma density (in our case, 50% increases on plasma density shows the disappearance of non-stable E_r region). These studies have been performed on an steady state situation $\partial E/\partial t = 0$, which suffers lack of time evolution process. In the next section, this model has been implemented into ASTRA and further calculations on the radial electric field in steady state is performed. The reason to perform steady-state transport simulation is that the time variation of the electric field is much faster than the time variation of the plasma temperature and density. In such conditions, the radial electric field can be calculated in the stead-state plasmas, considering constant plasma parameters like temperature and density.

6.5 Simulation Results Using ASTRA

In order to study the time evolution of radial electric field, the above mentioned theory is implemented in code ASTRA. However, Equation 6.6 only works in vicinity of magnetic islands and far from the magnetic islands, the particle fluxes are ambipolar. This is not true in TJ-II. In order to study the 'extra' modification induced by the magnetic islands, here we applied a 'background' neoclassical particle flux, denoted as Γ_p^{neo}. This background particle fluxes are generated by the conventional neoclassical model and in this section, two models are used separately, being Kovrizhnykh's model [110] and Beidler's model [111, 112].
The Kovrizhnykh's model calculates particle fluxes by dividing them into axisymmetric part $\Gamma_j^S$and an asymmetric part Γ_j^{AS} for both electrons $j = e$ and ions $j = i$, $\Gamma_j = \Gamma_j^S + \Gamma_j^{AS}$. The Beidler's model provides mono-energetic transport coefficients for an idealized stellarator field with a single helical mode and the transport coefficients are obtained by fitting with code DKES [113, 114]. Both Kovrizhnykh's model and Beidler's model have been tested and compared with the experimental data in TJ-II [115]. The main differences between these two conventional models compared with Shaing's model are:

1. Shaing's model has been derived based on the assumption that the toroidal configurations poses toroidal symmetry and only in vicinity of magnetic islands, this symmetry is broken. Hence, particle fluxes far from the vicinity of magnetic islands are intrinsically ambipolar. The radial electric field only appears in the location near the magnetic island.

2. The two conventional neoclassical models, being Kovrizhnykh's model and Beidler's model, on the other hand, deal with configurations with no toroidal symmetry, like stellarators. Hence, the non-ambipolar particle fluxes, in general exist in the whole plasma volume. This has been confirmed by both experimental [65] as well as simulations [104, 106, 115].

Here denote Γ_p^{is} the particle fluxes introduced by the magnetic islands and assume the total particle flux generated by both the background and the magnetic island is $\Gamma_p = \Gamma_p^{neo} + \Gamma_p^{is}$. With this assumption, we can carry out the transport study with ASTRA. The plasma parameters used here is presented in Figure 6.11, as a function of the normalized flux surface label ρ. The plasma is obtained with ECRH. The island width is assumed to be 0.5cm.
First of all, the theory is tested on a scan of different resonant locations in a tokamak case, i.e., $\Gamma_p^{neo} = 0$. The plasma parameters used here is the same as ones in Table 6.1, which is obtained on TJ-II. Note that the plasma parameters like density and

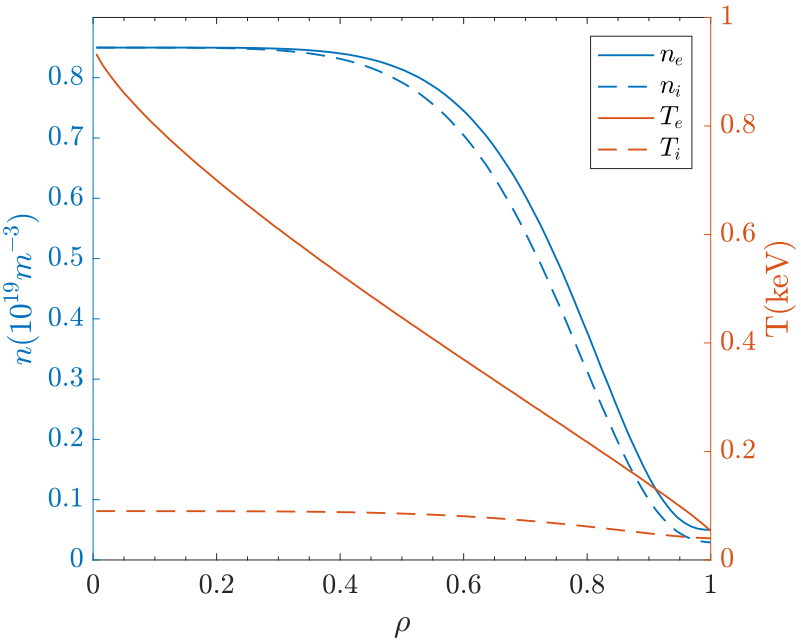

Figure 6.11: The parameters of ECRH plasma in TJ-II plotted as a function of the normalized flux surface label ρ. The blue solid line represents the electron density and the dashed blue line represents the ion density. The red solid line represents the electron temperature and the dashed one represents the ion temperature. This parameters are used in the following calculations in ASTRA.

temperature is irrelevant to different configurations and even a TJ-II plasma is used, the result should be valid in tokamak configurations with the same plasma parameters. The result is shown in Figure 6.12, with four locations highlighted by different colors. From the results, it seems that the radial electric field in tokamaks changes its sign depending on different radial locations of the magnetic island. It is positive in both $\rho = 0.48$ and $\rho = 0.65$ where ρ is the normalized flux label. When the resonant position moves outwards, reaching $\rho = 0.82$, the electric field shows positive on the inner side and negative on the other side. Thus, an electric shear is generated. With further outer moving, arriving at $\rho = 0.94$, the electric field becomes negative. Also it is clear that the electric field only appears around the resonant location. This is true because in tokamaks, regions far away from the resonant surfaces, the electron and ion fluxes are intrinsically ambipolar. However, the real physics behind of the phenomena described above is **not** related to the position of the resonance. It is the ratio between ion temperature and electron temperature that plays the role in

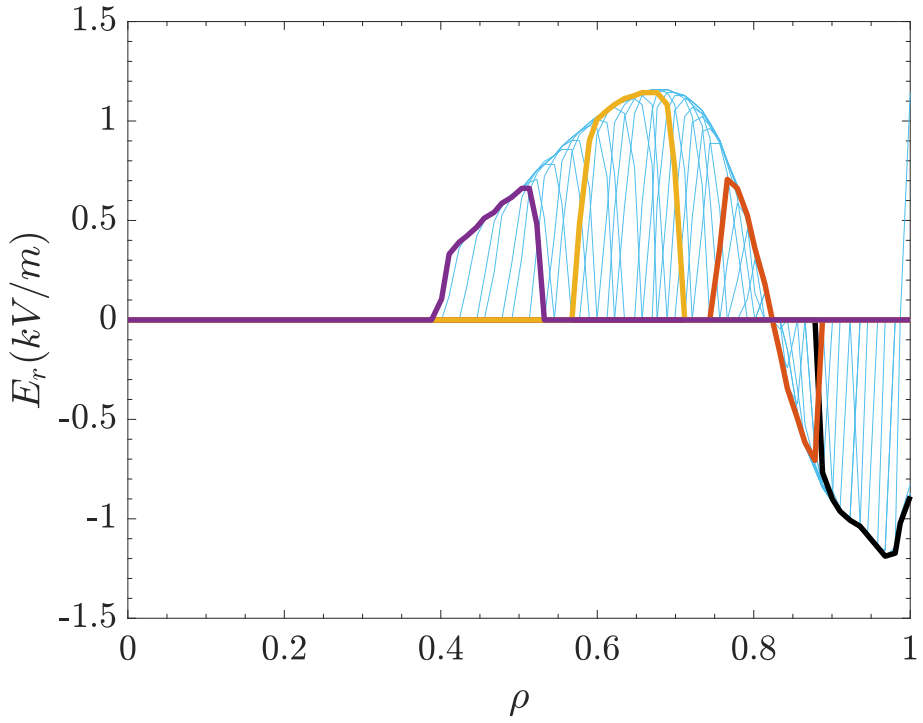

Figure 6.12: Electric field profiles with scan of resonance positions in tokamak parameters. Many different island locations have been applied in ASTRA with Shaing's model, represented by many light blue lines. Four positions are marked at normalized flux surface labels $\rho = 0.48, 0.65, 0.82$ and 0.94, respectively.

changing the sign of radial electric field. One should note that between $\rho = 0.82$ and $\rho = 0.94$, there is a location where the radial electric field is zero. By checking the TJ-II parameters shown in Figure 6.11, one could see that this location is the one with $T_i/T_e = 0.3$. This could be seen more clear in Figure 6.13, which is the value T_i/T_e plotted as a function of the normalized radius ρ. This condition has been proved that the particle fluxes are ambipolar if such condition is fulfilled. What is more, it has been shown in Figure 6.9 that the radial electric field is negative when the value $T_i/T_e > 0.3$ and it is positive when the value $T_i/T_e < 0.3$. By checking the profile of T_i/T_e, one could find that in the outer region, the negative radial electric condition is fulfills and in the inner part, the positive radial electric field condition is fulfilled. The reason for this special point with such temperature condition is that the plasma temperature could significantly change the ion and electron collision frequencies, given a fixed plasma density. So the fundamental explanation for this

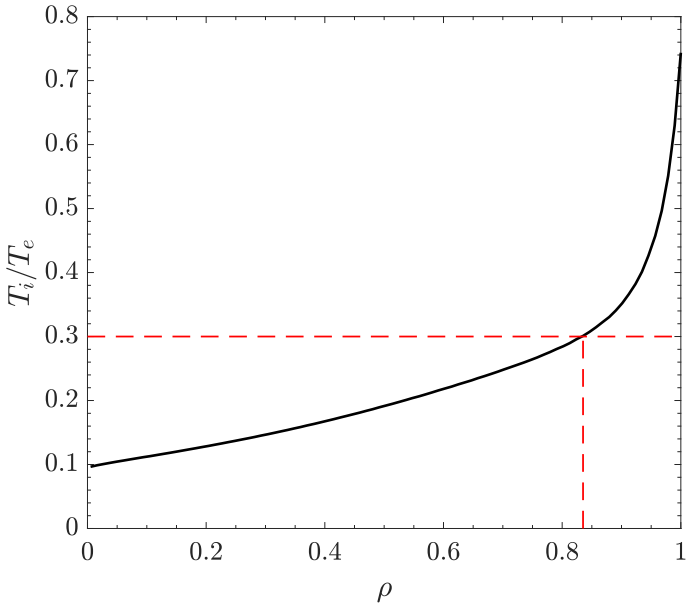

Figure 6.13: The ratio between ion temperature and electron temperature T_i/T_e is plotted as a function of the normalized radius, which is the black line. The two dashed red lines indicates the location of radius where $T_i/T_e = 0.3$.

phenomenon is that at the point with $T_i/T_e = 0.3$, the ion and electron collision frequencies reach a special condition which makes the radial electric field zero. Hence, we could safely draw the conclusion that this change of sign on radial electric field is strongly effected by the value T_i/T_e. And finally, if the island contains the location of $E_r = 0$, the a big electric field shear could appear in the resonance region, which brings the interesting operational proposal for L-H transition study.

Secondly, a neoclassical model developed by Kovrizhnykh [110] is included as the background of the neoclassical transport, together with Shaing's model. The simulation has been carried out on 4 different locations and the result is presented in Figure 6.14. The smooth line represents the background profile, i.e., generated only by Kovrizhnykh's model. The 4 'bumps', located in the inner and outer regions, are ones generated with Shaing's formula. The last bump in the outermost region is very small. The amplitude of the background profile is below 2 KV/m. The innermost one shows a significant decrease effect. The electric field in this position is almost zero. The second one shows a small increase respect to the background profile and the third one shows a decrease effect on the amplitude of the electric field.

And finally, another neoclassical transport model developed by Beidler [111, 112]

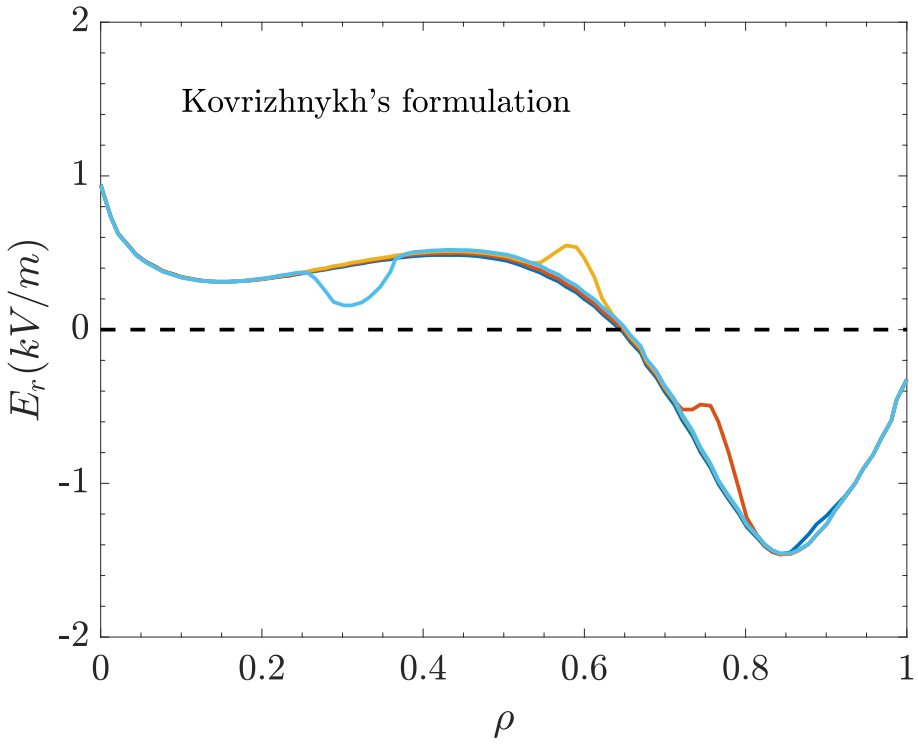

Figure 6.14: Electric field profiles obtained from Kovrizhnykh's model, together with Shaing's model are presented as a function of the normalized flux surface label. The smooth line represents the background of neoclassical transport, i.e., the profile generated only by Kovrizhnykh's model. The three 'bumps' are the results when Shaing's model is applied. In the inner locations, the electric field is positive with enhancement or decrease of the background electric field. In the outer region, however, the electric field is negative and it shows an enhancement of the background electric field.

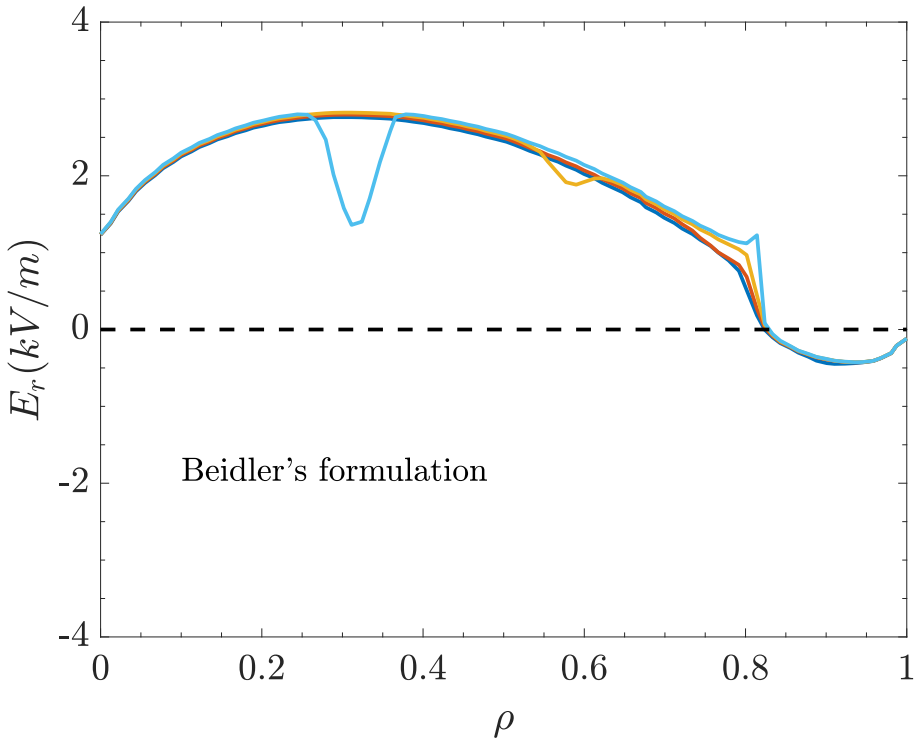

Figure 6.15: Electric field profiles obtained from Beidler's model, together with Shaing's model are presented as a function of the normalized flux surface label. The smooth line represents the background of neoclassical transport. The three 'bumps' are the results with Shaing's model. In this case all three resonant positions shows a positive electric contribution from Shaing's model and only the edge one shows an enhancement respect to the background electric field.

is applied as the background transport, together with Shaing's model. The same four locations have been adopted in these simulations and the result is presented in Figure 6.15. The amplitude of the background profile is below 4 kV/m, which is higher than one obtained with Kovrizhnykh's model. Also the zero point of this profile is in the outer region compared with Kovrizhnykh's model. Unlike the results shown in Figure 6.14, the modification on the electric profile using Beidler's model shows that the amplitude of the radial electric field induced by the magnetic islands is always positive in the first three locations with either decrease effect (first two) or enhancement effect (the third one). The innermost resonant position shows a big decrease effect on the background profile and the amplitude is almost zero, the same

as in Kovrizhnykh's model. The third one also shows a increase effect. However, the middle resonant position, shows a decrease effect which is different from the one in Kovrizhnykh's model. The outermost one is also very small.
Compared with the results from these two models, several things should be pointed

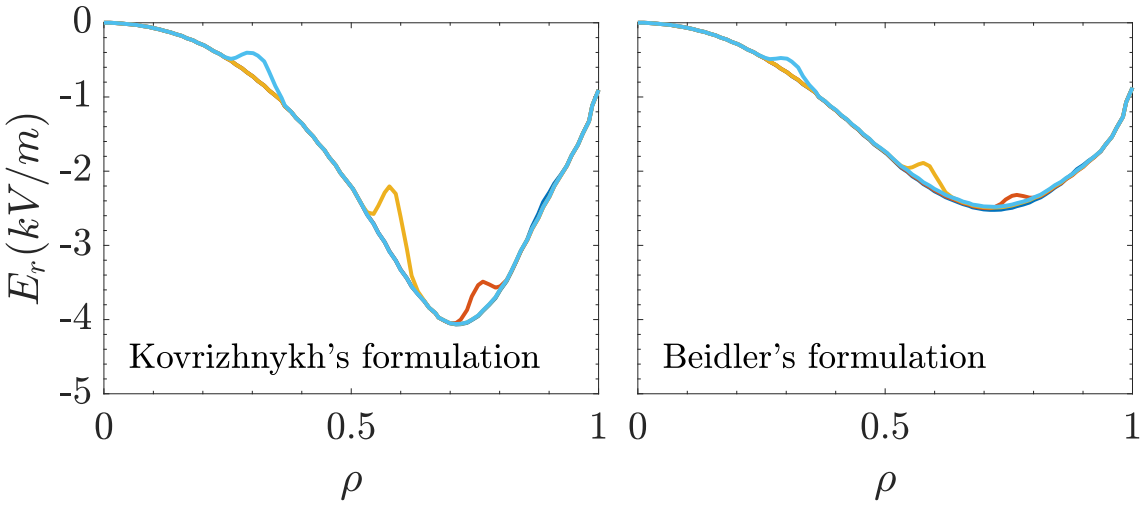

Figure 6.16: Two simulations are performed with different neoclassical models together with Shaing's formula in NBI plasma obtained in TJ-II. The left graph is obtained using both Kovrizhnykh's model and Shaing's formula. The right one is obtained using both Beidler's model and Shaing's formula. The smooth line represents the background radial electric field and the 'bumps' are the extra contribution from Shaing's theory. Clearly, the background radial electric field profile is always negative and the contribution from Shaing's theory is always positive, with respect to the background radial electric field profiles.

out. First of all, the innermost position shows the biggest modification. To be more specific, the amplitude of the electric field is almost zero in such position, with the presence of the magnetic islands. The possible reason is that in such region, the electron collision frequency is high due to high temperature. Hence, the island effect is very strong. The electrons in high collision frequency region seems to be decelerated by the magnetic islands. Secondly, the different behaviors for the second and third positions may related to different background profiles. Nevertheless, this point should be carefully checked in the further.
From the results shown above, we begin to understand the theory proposed by Shaing. The island contribution affects the background electric field, showing either an enhancement or a decrease. Also the sign of the electric field from island contribution

really differs from one model to another. What is more, the contribution from the islands in 'tokamak' case (Figure 6.12) shows higher or comparable amplitude of radial electric field with ones in TJ-II cases (third and fourth bumps in Figure 6.14 and 6.15). Another important thing needs to emphases is that so far, all the exercises are done in ECRH plasmas.

Besides the simulations performed in ECRH plasmas, another work, using an Neutral Beam Injection (NBI) plasma obtained in TJ-II has also been carried out. The main difference between ECRH and NBI plasmas is that the plasma is more collisional in NBI plasmas. Hence, different behaviors are expected in such plasmas. The corresponding plasma parameters in such NBI shot are: the plasma density is around $1.2 \times 10^{19} m^{-3}$, the central electron and ion temperatures are $0.35 keV$ and $0.15 keV$, respectively. The same island width as well as the locations are used here, adopting: 1, Kovrizhnykh' s model together with Shaing's model; 2, Beidler' s model with Shaing's model. The results are shown in Figure 6.16. The left graph is obtained using both Kovrizhnykh's model and Shaing's formula. The left one is obtained using both Beidler's model and Shaing's formula. The smooth line represents the background radial electric field and the 'bumps' are the extra contribution from Shaing's theory. Indeed the NBI plasma shows quite different behaviors compared with ECRH plasmas. First of all, the background radial electric field profiles in both simulations are always negative. Secondly, the contributions from the presence of magnetic islands are always positive in the sense that the contribution from magnetic islands always increases the local radial electric field. The results in such plasmas show consistent result between these two neoclassical models.

6.6 Summary and Discussions

The magnetic islands in TJ-II stellarator have been reported to play a role of modifying the local radial electric field, which in turn, plays a role in L-H transition by modifying the shear of $\boldsymbol{E} \times \boldsymbol{B}$ flow [65]. The main principle of this phenomenon is that the existence of magnetic islands distorts the flux surfaces, leading to an increase of the toroidal viscosity, which in turn, modifies the particle fluxes. A study based on the neoclassical toroidal viscosity thus has been carried out on TJ-II plasmas, with a moderate modification on the original theory.

First of all, in tokamak configurations, it has been shown that the ratio between ion and electron temperature T_i/T_e plays an important role in modifying the radial electric field. When $T_i/T_e = 0.3$, particle fluxes are intrinsically ambipolar. The reason for this phenomenon is that the collision frequency is significantly affected by the temperature. Interesting experimental proposal for the study of L-H transition

rises from this result: a magnetic island exists in the location with $T_i/T_e = 0.3$ could generate big $d\boldsymbol{E}/dr$, which could brings big impact on the plasma confinement properties.

Secondly, the study on ECRH plasma obtained in TJ-II shows that the presence of the magnetic islands indeed modifies the radial electric field. The modification varies with the choice of 'background' neoclassical transport model. For different neoclassical transport model, the modification shows either enhanced or decreased effect on the background electric field profile. Moreover, the study on NBI plasmas has also been performed. The results, however, differ from ones in ECRH plasmas. The background profiles have always negative value and the modification due to magnetic islands is always an enhancement.

What is more, it is worth mentioning that the results presented in this chapter are based on the universal effect induced by the presence of magnetic islands, that is the distortion on the nested flux surface. This distorting effect induced by the presence of magnetic islands is valid in all toroidal magnetic configurations with nested flux surfaces. Hence, the results presented in this chapter should also be valid in other devices. However, one needs to adjust the parameter $\mathscr{G}$ for each machine. The reason is that this parameter is obtained from the comparison between the particle diffusivity obtained from Shaing's original theory and the neoclassical transport in TJ-II. As mentioned in the beginning of this chapter, neoclassical transport in different stellarators differs from each other. Compared with tokamaks, devices like TJ-II have much higher neoclassical transport while in other stellarators like W7-X [116, 117], on the other hand, the neoclassical transport is lower [107]. Consequently, the factor $\mathscr{G}$ should adjust for each configuration.

And finally, the assumption of neglecting the super-banana effect should be carefully checked theoretically in the future. The super-banana effect is induced by the presence of local magnetic mirrors, which commonly exist in stellarators due to lack of toroidal symmetry. This is true even with optimized stellarator configurations. Another point should be made is that the treatment of particle fluxes is a perturbative, i.e., $\Gamma_p = \Gamma_p^{neo} + \Gamma_p^{is}$. Such treatment should be examined in the future work.

Part IV

Conclusion and Future Perspective

7

Summary, Conclusion and Future Perspective

7.1 Summary

The realization of commercial fusion power plants becomes more and more urgent with dramatically increased energy demand nowadays. After 60 years of research on fusion plasmas in toroidal magnetic configurations, we are getting closer and closer. One of the main issues in the fusion community is the low energy as well as particle confinement properties, due to high radial transport losses, which give rise to the importance of transport study for better understanding the plasma confinement properties.

Transport phenomenon in toroidal magnetic configurations contains two components, the parallel transport and the perpendicular transport, with respect to the magnetic field. Between these two components, it is usually the parallel transport that dominants the transport process. In devices with nested flux surfaces like tokamaks and stellarators, particles are strongly constrained on the flux surfaces and the radial losses are mainly caused by the perpendicular transport across the flux surfaces. Many studies show that in these devices transport phenomena can be well described in the framework of neoclassical theory. On the other hand, in devices with no nested flux surfaces like RFPs, the field lines fill the whole plasma volume and the radial losses are mainly caused by the parallel transport along the field lines. The reason is that the RFP configurations are sustained by the dynamo mechanism which is related to the non-linear interactions among many resonating MHD tearing modes. Consequently, the transport process in RFP plasmas is dominated by stochastic transport, especially in Multiple Helicity state, where all the modes have comparable amplitudes. However, when it comes to Quasi-Single Helicity state where a single mode dominates the mode spectrum, a good confinement region where the flux surfaces are nearly conserved has been identified. Indeed, in this region, steep thermal gradients have been reported and the kinetic quantities like temperature and density could be treated as functions of the flux surfaces. Hence, in QSH state, the transport study is focused on this special region, considering that the magnetic field has the equilibrium component and *only* the dominant mode.

The magnetic island, which commonly exists in fusion devices, is the result of resistive tearing modes. It breaks the nested flux surfaces by reconnecting the field lines and this leads to a degradation of the plasma confinement properties. Meanwhile,

the presence of the magnetic island also breaks the symmetry that one device owns and makes the magnetic field intrinsically three dimensional. Facing these issues, this dissertation presents the transport study in toroidal configurations, focused on three dimensional effect induced by the presence of magnetic islands. The methodology is to find certain symmetry so that the transport study could be performed on 1.5 dimensions. Specifically, the transport study has been carried out on two devices, one part on RFX-mod and the other part on TJ-II stellarator.

Work on RFX-mod

The work on RFX-mod has been carried out on the study of three sub-states of the Quasi-Single Helicity state, which is a plasma regime observed in RFP devices. In QSH state, the magnetic field is treated as a pure SH state, meaning that the secondary modes are neglected and only the equilibrium field and the dominant mode are considered. In such a way, the RFP plasmas have helical symmetry which allows us to perform 1.5 dimensional transport study. The three sub-states are: DAx, SHAx_n and SHAx_w. However, obstacles encounter when attempts were made to study transport properties in these three sub-states, especially in the DAx state. The issue is that in DAx state, there are two magnetic axes, one being the original magnetic axis and the other one being the island axis. Consequently, no monotonic coordinate as well as the correct metrics can be defined to describe the whole plasma volume. In order to overcome this problem, a Multiple Domain Scheme (MDS) is proposed, with the main idea of dividing the whole plasma into three separated regions. By doing so, a monotonic radial coordinate as well as the correct metrics can be well defined in each region. The communication among these three separated regions is done by the separatrix, which is a thin layer featuring high transport properties. With the help of MDS, a routine named Multiple Axes Solver (MAxS), capable of dealing with configurations containing either single or multiple magnetic axes has been developed and benchmarked with code ASTRA, which is a well-know transport code in fusion community. The good agreement between MAxS and ASTRA in the benchmark results gives us confidence to proceed the transport study in these three sub-states. The transport study on RFX-mod was firstly carried out on the analysis of the thermal gradients in the electron Internal Transport Barrier (eITB) region. The electron temperature profiles are obtained with Thomson Scattering diagnostic and they are further selected based on a narrower plasma density and current range. The thermal gradients are calculated by a routine named TeGrA, which has been developed and tested on the purpose of automatic analyzing the eITB regions. The outcome of routine TeGrA shows that the thermal gradient tends to decrease with the increase

of the normalized dominant mode, indicating a local increase of energy transport in the eITB region. To confirm this observation, a transport study on a small database has been carried out, with the help of routine MAxS and the results indeed show that the thermal diffusivity in the eITB region tends to increase with the increase of the normalized dominant mode.
This peculiar behavior of thermal gradients encouraged us to study further on the transport mechanism that is responsible for this observation. The investigation was done with both the thermal gradients and the thermal diffusivity in the eITB region, with respect to the secondary modes, that are the source of the stochasticity in RFP plasmas. Two different behaviors were identified, one in narrow thermal structure groups (DAx and SHAx_n) and the other one in wide thermal structure group (SHAx_w). These results can be explained within the framework of the stochastic transport theory:

- In narrow thermal structure group, the thermal gradients tend to increase with the decrease of the secondary modes and consistently, the thermal diffusivity shows the opposite behavior. This is true because the reduction of the secondary modes indicates a lower stochasticity level and this in turn, makes the thermal gradient steeper.

- For for the wide thermal structure group, the thermal gradients show a sudden decrease and for the thermal diffusivity, as expected, shows a sudden jump. This result can still be explained by the stochastic transport. The difference between narrow and wide groups is that the location of the eITB 'migrates' from inner region (narrow group) to outer region (wide group). Consequently, the source of stochasticity also changes between narrow and wide thermal structure groups. The thermal gradients in wide thermal structure group thus suffer higher stochasticity produced by modes with higher toroidal mode number.

Besides the different thermal gradient behaviors mentioned above, the effect induced by the migration of the thermal gradients is also responsible for the sudden jump in the amplitude of the width of the thermal structures, reported in Reference [90]. Inspired by such work, a more detailed work on the thermal expansion process has been carried out. The result reveals the fact that the sudden jump is only due to the top expansion of the thermal structure. The foot of the the eITB shows a smooth growth within these three sub-states. Nevertheless, one question remains unsolved: what is the physical explanation to the different behaviors between the top and foot width. Further study is required to clarify this point.
The final part on RFX-mod dedicates to investigating the energy confinement time.

This study was motivated by the unexpected behavior of the local increased transport properties in the eITB region. Here an improved method, considering the 'real' shape of the distorted flux surfaces has been firstly adopted in such calculations. The result shows that the energy confinement time increases up to 40% from DAx to SHAx_w. This result indicates that with the growth of the dominant mode, the plasma enters into a more ordered state.

Work on TJ-II

The transport study in TJ-II differs from the one carried out in RFX-mod in the sense that the physics governing the transport process is different. In TJ-II plasmas, it is the neoclassical transport who dominates the radial transport in low collisionality regime. In such configuration, the presence of the magnetic islands enhances the toroidal viscosity, giving rise to a non-intrinsically ambipolar particle flux in vicinity of magnetic islands and this effect, in turn, generates a local radial electric field, which could bring an impact to the L-H transition. Based on this idea, a Neoclassical Toroidal Viscosity theory developed by K. C. Shaing [63] is adopted, with a moderate change, being to apply a factor $\mathscr{G} = 1000$ on the original particle flux equations due to the fact that the original theory has been developed for tokamak configurations. The study on the particle transport equations revels some results:

- Increasing the radial electric field to a certain level leads to the disappearance of the $\sqrt{\nu}$ (also possible $1/\nu$) collision regime and only ν regime survives.
- The electron and ion temperatures play a role in the sign and amplitude of radial electric field. By increasing the ion temperature, the radial electric field changes its sign from positive to negative, with its amplitude firstly decreasing and then increasing.
- One special point has been identified, where intrinsically ambipolar fluxes shows up with the condition $T_i/T_e = 0.3$. At this point, the contribution of the magnetic island to radial electric field is zero.

Inspired by these results, further study on the effects induced by the presence of magnetic islands in both tokamak and TJ-II configuration has been further performed, by implementing the particle flux equations into ASTRA:

- For the study of tokamak configurations using a ECRH plasma, results show that the radial electric field only shows up in vicinity of magnetic islands.

Regions far away are with zero radial electric field. This is true because in regions far away from the magnetic islands, due to intrinsically ambipolarity in tokamak configurations the electric fields are intrinsically zero.

- The second result in tokamak configurations is that the sign of radial electric field seems to depend on the location of the magnetic islands. Further study, however, reveals that it is the ratio between ion and electron temperature that determines the sign of radial electric field.

- Further study, applying a neoclassical background on TJ-II stellarator with the same ECRH plasma parameters, shows that the presence of magnetic islands plays a either enhancement or diminution role on the background radial electric field profiles. The amplitude of modification also varies on the choice of the 'background' neoclassical transport model. The fundamental reason for this observation is that the plasma temperature greatly affects the collisionality, which in turn, affects the radial electric field.

- The last part is the study on TJ-II stellarator with NBI plasma parameters. Both the two neoclassical models show negative background radial electric field profiles, with enhancement effects from the presence of magnetic islands, despite of the different island locations.

- One more point should be made is that comparing between 'tokamak' and TJ-II results, the results shows that with a background electric field, the contribution from the magnetic islands are reduced in its amplitude.

7.2 Conclusions and Future Perspective

The study on RFX-mod shows that the presence of the magnetic islands plays an important role in determining the energy confinement properties. First of all, the internal transport barrier weakens its strength with the growth of the dominant tearing mode. This leads to an local increase of the energy transport. However, this enhanced local transport shows no bad influence on the energy confinement properties. Indeed, an upgrade in energy confinement properties in RFX-mod plasmas has been identified with the growth of the dominant tearing mode. This is partially due to the increase of plasma volume with good confinement properties (thermal structure expansion), and reductions on the source of bad confinement (decreasing of the amplitude of the secondary modes). The work presented on RFX-mod, although carried out on one device, should be valid and replicated in other RFP

devices with two most fundamental reasons, being that first of all, the QSH state, with the same magnetic field evolution process, has been observed in all RFP devices under certain proper experimental conditions. The second reason is that the RFP magnetic configurations, independent from different devices, are sustained by the dynamo mechanism, which is an universal behavior of RFP plasmas. Nevertheless, it is worth mentioning that in MST, the preliminary results show that the thermal structure identified in RFX-mod seems missing. This might due to much higher neutral particle penetration in MST. To clarify this point and to get a more solid physical knowledge on this point, further analysis on other experimental devices should be performed.

Several questions still remain in the work on RFX-mod. First of all, during the thermal expansion process, the behavior of the foot width is different from one of the top width. The explanation for the top width is presented while it remains to be clarified for the foot width behavior. Secondly, the reduction of secondary modes seems to reach a saturation state in SHAx_w. The explanation for this phenomenon should be clarified so that the further reduction or even diminution of secondary modes could be realized in future RFP experiments. And finally, the investigation of particle confinement properties within these three sub-states should also be carried out on the purpose of plasma confinement study.

The study on TJ-II stellarator reveals the role of magnetic islands on the modification of the radial electric field. The study in tokamak configurations shows an important result, being that the radial electric field is zero at the location where $T_i/T_e = 0.3$ and in the neighborhood, big $d\boldsymbol{E}_r/dr$ appears. This result shows a good experimental proposal for both validating this theory as well as the L-H transition study. The simulations in TJ-II configurations with ECRH plasmas show the modification effect depends on several things. First of all, different modification effects appear with different choices of the 'background' neoclassical transport models, indicating the applied background theory suffers lack of the whole transport properties. Unlike the inconsistent results obtained with ECRH plasmas, the results with NBI plasmas, on the other hand, show that both two background models behave the same in the sense that negative radial electric field profiles are obtained from these two 'background' models. Moreover, the modification induced by the magnetic islands also shows the same enhancement effect. Nevertheless, these simulation results show a promising way of changing the value of radial electric field, leading to interesting topics on L-H transition in the future. These results obtained in TJ-II stellarators, in principle should also be valid for other stellarators *with some modifications*. The main point is the factor $\mathscr{G}$ we used in TJ-II configuration should be modified. This factor is applied based on the fact that the neoclassical transport is much higher in TJ-II

than in tokamaks due to the fact that TJ-II had not been optimized to reduce the neoclassical transport. Devices with optimizations, on the other hand, have smaller neoclassical transport compared with one in tokamaks. Consequently, the factor $\mathscr{G}$ should be checked before applying on other configurations. And finally the factor $\mathscr{G}$, in principle should be different between electron and ion particle fluxes, which was not taken into account. Further study is needed to include this correction.
There are some remaining work for further studies. First of all, the study on TJ-II plasmas uses a perturbative way, meaning the interactions between the background model and the magnetic island model is $\Gamma_p = \Gamma_p^{neo} + \Gamma_p^{is}$. This assumption should be further checked to carry out solid simulations. Secondly, the effect of super-banana on the radial electric field should be further studied in stellarator configurations and finally, the inconsistency of the results between two background models in ECRH plasmas should be further studied.

Part V

Appendices

7.3 Flux Surface Average

The flux surface average of a function F is defined as follows:

$$\left\langle F \right\rangle_s = \frac{\int F d\theta d\phi \sqrt{g}}{\int d\theta d\phi \sqrt{g}} \tag{7.1}$$

θ is the poloidal angle and ϕ is the toroidal angle. $\sqrt{g}$ is the Jacobian. If we consider the toroidal symmetry and substitute $\sqrt{g} = 1/(\mathbf{B} \cdot \nabla\theta)$we have:

$$\left\langle F \right\rangle_s = \frac{\int F d\theta / \mathbf{B} \cdot \nabla\theta}{\int d\theta / \mathbf{B} \cdot \nabla\theta} \tag{7.2}$$

The orbit average of a function F is defined as follows:

$$\left\langle F \right\rangle_o = \frac{\left\langle FB/|u| \right\rangle_s}{\left\langle B/|u| \right\rangle_s} = \frac{\int FBd\theta/(|u|\mathbf{B} \cdot \nabla\theta)}{\int Bd\theta/(|u|\mathbf{B} \cdot \nabla\theta)} = \frac{\int Fd\theta/(|u|\mathbf{n} \cdot \nabla\theta)}{\int d\theta/(|u|\mathbf{n} \cdot \nabla\theta)} \tag{7.3}$$

With u the parallel velocity component, $\boldsymbol{n} = \boldsymbol{B}/|B|$. So if we take the orbit average in the form of $\left\langle u\nabla F \right\rangle_o$, we have:

$$\left\langle u\nabla F \right\rangle_o = \frac{\int n|u|\nabla F d\theta/(|u|\mathbf{n} \cdot \nabla\theta)}{\int d\theta/(|u|\mathbf{n} \cdot \nabla\theta)} = \frac{\int \mathbf{n} \cdot (\partial F/\partial\theta \nabla\theta) d\theta/(\mathbf{n} \cdot \nabla\theta)}{\int d\theta/(|u|\mathbf{n} \cdot \nabla\theta)} = \frac{\int d\theta \partial F/\partial\theta}{\int d\theta/(|u|\mathbf{n} \cdot \nabla\theta)} \tag{7.4}$$

The **bounce condition** is the distribution function is identical at the critical angle of the banana orbit:

$$f_+(\theta = \pm\theta_b) = f_-(\theta = \pm\theta_b) \tag{7.5}$$

With θ_b the angle at which the bounce takes place. Therefore, the bounce orbit average is:

$$\left\langle u\nabla F \right\rangle_o = 0 \tag{7.6}$$

This result indicates that the bounce orbit average will eliminate the information of the parallel direction.

7.4 Magnetic Field Strength in Tokamaks

This section is to derive a expression of the magnetic field strength in tokamak configurations, which has $1/R$ dependence, with R the radius from the toroidal center. The calculation starts with the Ampère's law:

$$\nabla \times B = \mu_0 \left(J + \epsilon_0 \frac{\partial E}{\partial t} \right) \tag{7.7}$$

Where B is the magnetic field, $\mu)0$ is the magnetic permeability in vacuum, J is the current density in the toroidal coils, ϵ_0 is the electric permittivity in vacuum and E the electric field. With a reasonable assumption: $\partial E/\partial t \approx 0$, we have:

$$\oint_S B dl = \mu_0 J \tag{7.8}$$

Which leads to

$$B = \frac{\mu_0 I}{2\pi R} \tag{7.9}$$

Here I the total current in the toroidal coils. For the magnetic field in the center of the plasma (center of the vacuum vessel), $R = R_0$, where R is the major radius, we have $B_0 = \mu_0 J/2\pi R_0$.
For any position r, here r is the poloidal local radius related to the magnetic axis, we have:

$$B = \frac{\mu_0 J}{2\pi \left| \vec{r} + \vec{R_0} \right|} \tag{7.10}$$

So we have:

$$\frac{B}{B_0} = \frac{r}{\left| \vec{r} + \vec{R_0} \right|} \tag{7.11}$$

Where $\left| \vec{r} + \vec{R} \right| = \sqrt{(r^2 + R_0^2 + 2rR_0 \cos\theta)}$. Define $\epsilon = r/R_0$, we could get:

$$f(\epsilon) = \frac{1}{\sqrt{1 + \epsilon^2 + 2\epsilon \cos\theta}} \tag{7.12}$$

And one could perform Taylor expansion to the 1st order at $\epsilon = 0$:

$$f(\epsilon) = \sum_{n=0}^{\infty} \frac{f(0)^{(n)}}{n!} (\epsilon - 0)^n = f(0) + f(0)' \cdot \epsilon \tag{7.13}$$

$$= 1 - \left[\frac{1}{2} \left(\epsilon^2 + 1 + 2\epsilon \cos\theta \right)^{-3/2} (2\epsilon + 2\cos\theta) \right]_{\epsilon=0} \cdot \epsilon \tag{7.14}$$

$$= 1 - \epsilon \cdot \cos\theta \tag{7.15}$$

So the magnetic field strength $|\boldsymbol{B}| = B_0(1 - \epsilon\cos\theta)$

7.5 Non-Ambipolar FLux and Toroidal Viscosity

Moment Approach

In this part, Hamada coordinate [118] (V, θ, ζ) is adopted with V the volume enclosed inside the magnetic surfaces, θ the poloidal angle and ζ the toroidal angle. The magnetic field can be represented as

$$\boldsymbol{B} = \psi'\nabla V \times \nabla\theta - \chi'\nabla V \times \nabla\zeta \tag{7.16}$$

Where χ is the poloidal flux and ψ is the toroidal flux. The prime denotes d/dV. The Jacobian is:

$$\sqrt{g} = (\nabla V \times \nabla\theta \cdot \nabla\zeta) = 1 \tag{7.17}$$

The particle flux is $\Gamma = n\mathbf{v}$ and its flux surface averaged in the direction of $\nabla\chi$ is:

$$\Gamma^{\chi} = \left\langle n\mathbf{v} \cdot \nabla\chi \right\rangle \tag{7.18}$$

The momentum equation is:

$$nm\frac{\partial \mathbf{v}}{\partial t} = ne\left(\mathbf{E} + \frac{1}{c}\mathbf{v} \times \mathbf{B}\right) - \nabla p - \nabla \cdot \overleftrightarrow{\pi} \tag{7.19}$$

Where $\overleftrightarrow{\pi}$ is the plasma viscosity. Taking the $\mathbf{B} \times \nabla\chi$ component of the steady-state momentum equation and using $(\mathbf{B} \times \nabla\chi)/B^2 = (\mathbf{B}_t \cdot \mathbf{B})\,\mathbf{B}/B^2 - \mathbf{B}_t$, $\mathbf{E} \times \mathbf{B} \cdot \nabla\chi = \mathbf{E} \cdot \mathbf{B} \times \nabla\chi$ and $I_c = \mathbf{B}_t \cdot \mathbf{B}$:, we have:

$$\Gamma^{\chi} = \langle n\mathbf{v} \cdot \nabla\chi \rangle = \left\langle nc\frac{\mathbf{E} \times \mathbf{B} \cdot \nabla\chi}{B^2} \right\rangle + \left\langle \frac{c}{eB^2}\mathbf{B} \times \nabla\chi \cdot \left(\nabla p - \nabla \cdot \overleftrightarrow{\pi}\right) \right\rangle \tag{7.20}$$

Using a vector identity:

$$\mathbf{B}_t = \frac{(\mathbf{B}_t \cdot \mathbf{B})\,\mathbf{B}}{B^2} - \frac{\mathbf{B} \times \nabla\chi}{B^2} \tag{7.21}$$

We could obtain:

$$\begin{aligned}\Gamma^{\chi} &= \left\langle nc\frac{\mathbf{EB}\cdot\nabla\chi}{B^2}\right\rangle + \left\langle \frac{c}{eB^2}\mathbf{B}\times\nabla\chi\cdot\left(\mathbf{F}_1-\nabla p-\nabla\cdot\overleftrightarrow{\pi}\right)\right\rangle \\ &= \left\langle \mathbf{E}\cdot\left[\frac{\mathbf{B}_t\cdot\mathbf{B}}{B^2}-\mathbf{B}_t\right]\right\rangle + \left\langle \frac{c}{e}\left[\frac{(\mathbf{B}_t\cdot\mathbf{B})\,\mathbf{B}}{B^2}-\mathbf{B}_t\right]\cdot\left(\mathbf{F}_1-\nabla p-\nabla\overleftrightarrow{\pi}\right)\right\rangle \\ = \left\langle nc\mathbf{E}\cdot\mathbf{B}\frac{I_c}{B^2}\right\rangle &- \langle nc\mathbf{E}\cdot\mathbf{B}_t\rangle + \frac{c}{e}\left\langle\frac{\mathbf{B}\cdot\mathbf{F}_1 I_c}{B^2}\right\rangle - \frac{c}{e}\left\langle\frac{\mathbf{B}\cdot\nabla p I_c}{B^2}\right\rangle - \frac{c}{e}\left\langle\frac{\mathbf{B}\cdot\nabla\cdot\overleftrightarrow{\pi} I_c}{B^2}\right\rangle \\ &- \frac{c}{e}\langle\mathbf{F}_1\cdot\mathbf{B}_t\rangle + \frac{c}{e}\langle\mathbf{B}_t\cdot\nabla p\rangle + \frac{c}{e}\left\langle\mathbf{B}_t\cdot\nabla\cdot\overleftrightarrow{\pi}\right\rangle \end{aligned} \tag{7.22}$$

The non-axisymmetric flux is

$$\Gamma^{NA} = \frac{e}{c}\left(\langle\mathbf{B}_t\cdot\nabla p\rangle + \left\langle\mathbf{B}_t\cdot\nabla\cdot\overleftrightarrow{\pi}\right\rangle\right) \tag{7.23}$$

In Hamada coordinates, $\langle\mathbf{B}_t\cdot\nabla p\rangle = 0$ for any non-axisymmetric torus and only $\left\langle\mathbf{B}_t\cdot\nabla\cdot\overleftrightarrow{\pi}\right\rangle$ contributes to non-axisymmetric partical flux Γ^{NA}.
The Pfirsch-Schluter flux

$$\Gamma^{PS} \tag{7.24}$$

The banana-plateau flux

$$\Gamma^{BP} = -\frac{c}{e}\left\langle\frac{\mathbf{B}\cdot\nabla\cdot\overleftrightarrow{\pi} I_c}{B^2}\right\rangle \tag{7.25}$$

The classical flux

$$\Gamma^{CL} \tag{7.26}$$

The residual $\mathbf{E}\times\mathbf{B}$ flux

$$\Gamma^{E} = nc\,\langle\mathbf{E}\cdot\mathbf{B}\rangle\,\frac{\langle I_c\rangle}{\langle B^2\rangle}\left(1-\frac{\langle I_c\rangle}{\langle B^2\rangle}\frac{\langle B^2\rangle}{\langle I_c\rangle}\frac{V'}{4\pi^2 q}\right) \tag{7.27}$$

The flux associated with the moving velocity of the toroidal magnetic flux surface

$$\Gamma^{g} = nc\,\langle\mathbf{E}\cdot\mathbf{B}\rangle\left(\frac{V'}{4\pi^2 q}-\langle\mathbf{E}\cdot\mathbf{B}_t\rangle\right) \tag{7.28}$$

Note that the Γ^E, Γ^g are usually ignored and the Γ^{PS} is not in the banana regime. Also the Γ^{BP} is the parallel viscous force part and goes to zero after solving the bounced average of the kinetic equation.

Kinetic approach

The definition for the neoclassical particle flux is:

$$\Gamma^{\chi} = \left\langle \int d\mathbf{v} f \mathbf{v}_d \cdot \nabla\chi \right\rangle + \left\langle nc \frac{\mathbf{E}^{(A)} \times \mathbf{B}}{B^2} \right\rangle \tag{7.29}$$

with $\boldsymbol{v}_d = -v_{\parallel}\boldsymbol{b} \times \nabla(v_{\parallel}/\Omega)$ [119], the $\nabla\chi$ direction component is thus: $\mathbf{v}_d \cdot \nabla\chi = (v_{\parallel}/B)\nabla \cdot \left[\left((v_{\parallel}/\Omega)\right) \mathbf{B} \times \nabla\chi \right]$, we have:

$$\Gamma^{\chi} = \left\langle \int d\mathbf{v} f \mathbf{v}_{\perp} \cdot \nabla\chi \right\rangle = \left\langle \int d\mathbf{v} f \frac{v_{\parallel}}{B} \nabla \cdot \left[B^2 \left(\frac{v_{\parallel}}{\Omega}\right) \left(\frac{\mathbf{B} \times \nabla\chi}{B^2}\right) \right] \right\rangle \tag{7.30}$$

Using a vector identity:

$$\mathbf{B}_t = \frac{(\mathbf{B}_t \cdot \mathbf{B})\,\mathbf{B}}{B^2} - \frac{\mathbf{B} \times \nabla\chi}{B^2} \tag{7.31}$$

$$\begin{aligned} \Gamma^{\chi} = &- \left\langle \int d\mathbf{v} f \left(\frac{v_{\parallel}}{B}\right) \nabla \cdot \left(\frac{v_{\parallel} B^2 \mathbf{B}_t}{\Omega}\right) \right\rangle + \left\langle \int d\mathbf{v} f \left(\frac{v_{\parallel}}{B}\right) \nabla \cdot \left[\left(\frac{v_{\parallel} B^2 \mathbf{B}_t}{\Omega}\right) \left(\frac{I_c}{B^2} - \frac{\langle I_c \rangle}{\langle B^2 \rangle}\right) \right] \right\rangle \\ &+ \left\langle \int d\mathbf{v} f \left(\frac{v_{\parallel}}{B}\right) \nabla \cdot \left[\left(\frac{v_{\parallel} B^2 \mathbf{B}_t}{\Omega}\right) \frac{\langle I_c \rangle}{\langle B^2 \rangle} \right] \right\rangle + \left\langle nc \frac{\mathbf{E}^{(A)} \times \mathbf{B}}{B^2} \right\rangle \end{aligned} \tag{7.32}$$

The non-axisymmetric flux Γ^{NA} is

$$\Gamma^{NA} = - \left\langle \int d\mathbf{v} f \left(\frac{v_{\parallel}}{B}\right) \nabla \cdot \left(\frac{v_{\parallel} B^2 \mathbf{B}_t}{\Omega}\right) \right\rangle \tag{7.33}$$

This is equivalent to Equation 7.23 from the momentum approach, which indicates the non-axisymmetric flux is due to the toroidal viscosity.

Acknowledgement

Acknowledgement

在和世界交手的这许多年，你是否光彩依旧，兴致盎然。

This three-year PhD study in Padova has been an excellent experience for me, not only for academic aspect but also for personal growth. In the end of my doctoral study, I would like to make my acknowledgement to all the people that walked into my life.

First of all, I would like to express my gratitude to the funder of Erasmus Mundus Fusion DC program, Prof. Dr. Guido Van Oost and the former coordinator in RFX, Prof. Piero Martin. It is they who gave me this opportunity that allowed me to study in Padova. Also I would like to thank the current coordinator of Fusion DC, Prof. Dr. Jean-Marie Noterdaeme and current coordinator in RFX, Prof. Paolo Bettini. They offered countless help during my PhD study.

I would like to express my great gratitude to my supervisor, Dr. David Terranova. He gave me constant academic help during my PhD study as well as to complete this dissertation. I also want to thank Dr. Fulvio Auriemma, Dr. Rita Lorenzini, Dr. Barbara and Dr. Fabio Sattin. They offered me great help in the study of RFX-mod. And I also want to thank Dr. Daniel López- Bruna and Prof. José Ramón Martín Solís, who gave me great help when I studied on TJ-II, Madrid. Besides the help I received, the more valuable thing I learned is the cautious attitude towards scientific research.

I want to thank all my colleagues in RFX. They made my life in Italy colorful. This means a lot for me especially because I am far away home. I want to thank Dr. Shichong Guo who offered me great help when I just arrived at Italy. I want to thank Flavia Raggi who helped me when I had problems with my accommodation. And I want to thank Ms. Fiorella who offered many help during my study.

In the end, I want to thank all my family and all my friends. My Father, Hongshuai Zhang and my mother, Kefen Sun, gave me great support for my PhD study.

For all the people who I met during my PhD study, I am deeply grateful for your kindness and hospitality.

References

Bibliography

[1] Francis F. Chen. *Introduction to Plasma Physics and Controlled Fusion*. Springer, 3rd ed. edition, 2015.

[2] John D Lindl, Peter Amendt, Richard L Berger, S Gail Glendinning, Siegfried H Glenzer, Steven W Haan, Robert L Kauffman, Otto L Landen, and Laurence J Suter. The physics basis for ignition using indirect-drive targets on the National Ignition Facility. *Physics of Plasmas (1994-present)*, 11(2):339–491, 2004.

[3] John D Lawson. Some criteria for a power producing thermonuclear reactor. *Proceedings of the Physical Society. Section B*, 70(1):6, 1957.

[4] Joseph Donald Huba. Nrl: Plasma formulary. Technical report, DTIC Document, 2004.

[5] Jagdish K Tuli et al. Nuclear wallet cards, 2005.

[6] John Wesson and David J Campbell. *Tokamaks*, volume 149. Oxford University Press, 2011.

[7] PR Thomas, P Andrew, B Balet, D Bartlett, J Bull, B De Esch, A Gibson, C Gowers, H Guo, G Huysmans, et al. Observation of alpha heating in JET DT plasmas. *Physical review letters*, 80(25):5548, 1998.

[8] Hartmut Zohm. *Magnetohydrodynamic Stability of Tokamaks*. John Wiley & Sons, 2014.

[9] HAB Bodin. The reversed field pinch. *Nuclear Fusion*, 30(9):1717, 1990.

[10] Mitsuru Kikuchi, Karl Lackner, and Minh Quang Tran. Fusion physics. 2012.

[11] Olivier Sauter, Clemente Angioni, and YR Lin-Liu. Neoclassical conductivity and bootstrap current formulas for general axisymmetric equilibria and arbitrary collisionality regime. *Physics of Plasmas (1994-present)*, 6(7):2834–2839, 1999.

[12] WA Houlberg, KC Shaing, SP Hirshman, and MC Zarnstorff. Bootstrap current and neoclassical transport in tokamaks of arbitrary collisionality and aspect ratio. *Physics of Plasmas (1994-present)*, 4(9):3230–3242, 1997.

[13] T. Fujita, S. Ide, Y. Kamada, T. Suzuki, T. Oikawa, S. Takeji, Y. Sakamoto, Y. Koide, A. Isayama, T. Hatae, H. Kubo, S. Higashijima, O. Naito, H. Shirai, and T. Fukuda. Quasisteady high-confinement reversed shear plasma with large bootstrap current fraction under full noninductive current drive condition in JT-60U. *Phys. Rev. Lett.*, 87:085001, Jul 2001.

[14] Kyōji Nishikawa and Masahiro Wakatani. *Plasma Physics: basic theory with fusion applications*, volume 8. Springer Science & Business Media, 2013.

[15] Lyman Spitzer Jr. The stellarator concept. *Physics of Fluids (1958-1988)*, 1(4):253–264, 1958.

[16] VD Shafranov. Equilibrium of a toroidal pinch in a magnetic field. *Soviet Atomic Energy*, 13(6):1149–1158, 1963.

[17] Yuhong Xu. A general comparison between tokamak and stellarator plasmas. *Matter and Radiation at Extremes*, 1(4):192–200, 2016.

[18] Jeffrey P Freidberg. Ideal magnetohydrodynamics. 1987.

[19] Jeffrey P Freidberg. *Plasma physics and fusion energy*. Cambridge university press, 2008.

[20] Roscoe B White. *The theory of toroidally confined plasmas*. Imperial College Press, 2006.

[21] Hannes Alfvén. Existence of electromagnetic-hydrodynamic waves. *Nature*, 150:405–406, 1942.

[22] Thomas James Morrow Boyd and Jeffrey John Sanderson. *The physics of plasmas*. Cambridge University Press, 2003.

[23] Sergio Ortolani and Dalton D Schnack. *Magnetohydrodynamics of plasma relaxation*, volume 156. World Scientific, 1993.

[24] J Brian Taylor. Relaxation of toroidal plasma and generation of reverse magnetic fields. *Physical Review Letters*, 33(19):1139, 1974.

[25] DF Escande, R Paccagnella, S Cappello, C Marchetto, and F D'Angelo. Chaos healing by separatrix disappearance and quasisingle helicity states of the reversed field pinch. *Physical review letters*, 85(15):3169, 2000.

[26] D Merlin, S Ortolani, R Paccagnella, and M Scapin. Linear resistive magnetohydrodynamic stability analysis of reversed field pinch configurations at finite beta. *Nuclear Fusion*, 29(7):1153, 1989.

[27] P Sonato, G Chitarin, P Zaccaria, F Gnesotto, S Ortolani, A Buffa, M Bagatin, WR Baker, S Dal Bello, P Fiorentin, et al. Machine modification for active MHD control in RFX. *Fusion engineering and design*, 66:161–168, 2003.

[28] Carlos Alejaldre, Jose Javier Alonso Gozalo, Jose Botija Perez, Francisco Castejón Magaña, Jose Ramon Cepero Diaz, Jose Guasp Perez, A Lopez-Fraguas, Luis García, Vladimir I Krivenski, R Martin, et al. TJ-II project: a flexible heliac stellarator. *Fusion Science and Technology*, 17(1):131–139, 1990.

[29] Paolo Franz, Lionello Marrelli, Andrea Murari, Gianluca Spizzo, and Piero Martin. Soft X ray tomographic imaging in the RFX reversed field pinch. *Nuclear fusion*, 41(6):695, 2001.

[30] A Alfier and R Pasqualotto. New thomson scattering diagnostic on RFX-mod. *Review of scientific instruments*, 78(1):013505, 2007.

[31] P Innocente and S Martini. A two color multichord infrared interferometer for RFX. *Review of scientific instruments*, 63(10):4996–4998, 1992.

[32] P Innocente, S Martini, A Canton, and L Tasinato. Upgrade of the RFX CO2 interferometer using in-vessel optics for extended edge resolution. *Review of scientific instruments*, 68(1):694–697, 1997.

[33] L Carraro, E Casarotto, R Pasqualotto, ME Puiatti, F Sattin, P Scarin, and M Valisa. Impurity influx studies in the RFX reversed field pinch. *Journal of nuclear materials*, 220:646–649, 1995.

[34] Andrea Murari, Paolo Franz, Luca Zabeo, Rosario Bartiromo, Lorella Carraro, Gianni Gadani, Lionello Marrelli, Piero Martin, Roberto Pasqualotto, and Marco Valisa. An optimized multifoil soft X-ray spectrometer for the determination of the electron temperature with high time resolution. *Review of scientific instruments*, 70(1):581–585, 1999.

[35] G Serianni, T Bolzonella, R Cavazzana, G Marchiori, N Pomaro, L Lotto, M Monari, and C Taliercio. Development, tests, and data acquisition of the integrated system of internal sensors for RFX. *Review of scientific instruments*, 75(10):4338–4340, 2004.

[36] E Ascasíbar, J Qin, A López-Fraguas, JA Jiménez, OI Fedyanin, JM Delgado, T Estrada, E de la Luna, F Castejón, TJ-II Team, et al. Energy content and magnetic configuration scan in TJ-II plasmas. In *Proc. 13th Stellarator Workshop (Canberra, 2002)*, 1999.

[37] R Jiménez-Gómez, E Ascasibar, T Estrada, I García-Cortés, B Van Milligen, A López-Fraguas, I Pastor, and D López-Bruna. Analysis of magnetohydrodynamic instabilities in TJ-II plasmas. *Fusion science and technology*, 51(1):20–30, 2007.

[38] E De la Luna, J Sánchez, V Tribaldos, and T Estrada. Multichannel electron cyclotron emission radiometry in TJ-II stellarator. *Review of Scientific Instruments*, 72(1):379–382, 2001.

[39] F Medina, L Rodrıguez-Rodrigo, J Encabo-Fernández, A López-Sánchez, P Rodrıguez, and C Rueda. X-ray diagnostic systems for the TJ-II flexible heliac. *Review of scientific instruments*, 70(1):642–644, 1999.

[40] F Medina, MA Pedrosa, MA Ochando, L Rodrıguez, C Hidalgo, AL Fraguas, BA Carreras, et al. Filamentary current detection in stellarator plasmas. *Review of Scientific Instruments*, 72(1):471–474, 2001.

[41] F Medina, MA Ochando, A Baciero, and J Guasp. Characterization of ripple-trapped suprathermal electron losses by their bremsstrahlung emission in the soft X-ray range at the TJ-II stellarator. *Plasma Physics and Controlled Fusion*, 49(4):385, 2007.

[42] MA Ochando, F Medina, B Zurro, A Baciero, KJ McCarthy, MA Pedrosa, C Hidalgo, E Sánchez, J Vega, AB Portas, et al. Up-down and in-out asymmetry monitoring based on broadband radiation detectors. *Fusion science and technology*, 50(2):313–319, 2006.

[43] B Zurro, MA Ochando, A Baciero, KJ McCarthy, F Medina, A López-Sánchez, D Rapisarda, D Jimenez, A Fernandez, I Pastor, et al. Method to deduce local impurity transport quantities from the evolution of tomographically reconstructed bolometer signals during tracer injection at TJ-II. *Review of scientific instruments*, 75(10):4231–4233, 2004.

[44] AP Navarro, MA Ochando, and A Weller. Equilibrium-based iterative tomography technique for soft X-ray in stellarators. *IEEE transactions on plasma science*, 19(4):569–579, 1991.

[45] E Barrera, M Ruiz, S López, D Machón, J Vega, and M Ochando. Real-time data acquisition and parallel data processing solution for TJ-II bolometer arrays diagnostic. *Fusion engineering and design*, 81(15):1863–1867, 2006.

[46] Horacio Lamela, Pablo Acedo, James Irby, et al. Laser interferometric experiments for the TJ-II stellarator electron-density measurements. *Review of Scientific Instruments*, 72(1):96–102, 2001.

[47] T Estrada, J Sánchez, B Van Milligen, L Cupido, A Silva, ME Manso, and V Zhuravlev. Density profile measurements by am reflectometry in TJ-II. *Plasma physics and controlled fusion*, 43(11):1535, 2001.

[48] L Cupido, J Sánchez, and T Estrada. Frequency hopping millimeter wave reflectometer. *Review of scientific instruments*, 75(10):3865–3867, 2004.

[49] T Happel, T Estrada, E Blanco, V Tribaldos, A Cappa, and A Bustos. Doppler reflectometer system in the stellarator TJ-II. *Review of Scientific Instruments*, 80(7):073502, 2009.

[50] IS Bondarenko, AA Chmuga, NB Dreval, SM Khrebtov, AD Komarov, AS Kozachok, LI Krupnik, P Coelho, M Cunha, B Gonçalves, et al. Installation of an advanced heavy ion beam diagnostic on the TJ-II stellarator. *Review of Scientific Instruments*, 72(1):583–585, 2001.

[51] MA Pedrosa, A López-Sánchez, C Hidalgo, A Montoro, A Gabriel, J Encabo, J De La Gama, LM Martınez, E Sánchez, R Pérez, et al. Fast movable remotely controlled Langmuir probe system. *Review of scientific instruments*, 70(1):415–418, 1999.

[52] CJ Barth, FJ Pijper, HJ vd Meiden, J Herranz, and I Pastor. High-resolution multiposition thomson scattering for the TJ-II stellarator. *Review of scientific instruments*, 70(1):763–767, 1999.

[53] SI Braginskii. Reviews of plasma physics. 1965.

[54] AA Galeev and RZ Sagdeev. Nonlinear plasma theory. In *Reviews of Plasma Physics, Volume 7*, volume 7, page 1, 1979.

[55] AA Galeev, RZ Sagdeev, HP Furth, and MN Rosenbluth. Plasma diffusion in a toroidal stellarator. *Physical Review Letters*, 22(11):511, 1969.

[56] AA Galeev and RZ Sagdeev. Transport phenomena in a collisionless plasma in a toroidal magnetic system. *Soviet Journal of Experimental and Theoretical Physics*, 26:233, 1968.

[57] MN Rosenbluth, RD Hazeltine, and Fl L Hinton. Plasma transport in toroidal confinement systems. *Physics of Fluids (1958-1988)*, 15(1):116–140, 1972.

[58] AB Rechester and MN Rosenbluth. Electron heat transport in a tokamak with destroyed magnetic surfaces. *Physical Review Letters*, 40(1):38, 1978.

[59] D Terranova, F Auriemma, A Canton, L Carraro, R Lorenzini, and P Innocente. Experimental particle transport studies by pellet injection in helical equilibria. *Nuclear Fusion*, 50(3):035006, 2010.

[60] Rita Lorenzini, E Martines, P Piovesan, D Terranova, P Zanca, M Zuin, A Alfier, D Bonfiglio, F Bonomo, A Canton, et al. Self-organized helical equilibria as a new paradigm for ohmically heated fusion plasmas. *Nature Physics*, 5(8):570–574, 2009.

[61] Francesco Porcelli, E Rossi, G Cima, and A Wootton. Macroscopic magnetic islands and plasma energy transport. *Physical review letters*, 82(7):1458, 1999.

[62] Piero Martin, L Marrelli, A Alfier, F Bonomo, DF Escande, P Franz, Lorenzo Frassinetti, M Gobbin, R Pasqualotto, P Piovesan, et al. A new paradigm for RFP magnetic self-organization: results and challenges. *Plasma Physics and Controlled Fusion*, 49(5A):A177, 2007.

[63] KC Shaing, K Ida, and SA Sabbagh. Neoclassical plasma viscosity and transport processes in non-axisymmetric tori. *Nuclear Fusion*, 55(12):125001, 2015.

[64] D. López-Bruna, M.A. Ochando, A. López-Fraguas, F. Medina, and E. Ascasíbar. Relationship between mhd events, magnetic resonances and transport barriers in TJ-II plasmas. *Nuclear Fusion*, 53(7):073051, 2013.

[65] D López-Bruna, M A Pedrosa, M A Ochando, T Estrada, B Ph van Milligen, A López-Fraguas, J A Romero, D Baião, F Medina, C Hidalgo, E Ascasíbar, I Pastor, C Rodríguez, D Tafalla, and the TJ-II Team. Magnetic resonances and electric fields in the TJ-II heliac. *Plasma Physics and Controlled Fusion*, 53(12):124022, 2011.

[66] S Cappello and DF Escande. Bifurcation in viscoresistive mhd: The hartmann number and the reversed field pinch. *Physical review letters*, 85(18):3838, 2000.

[67] John M Finn, Rick Nebel, and Charles Bathke. Single and multiple helicity ohmic states in reversed-field pinches. *Physics of Fluids B: Plasma Physics (1989-1993)*, 4(5):1262–1279, 1992.

[68] P Martin, L Marrelli, G Spizzo, P Franz, P Piovesan, I Predebon, T Bolzonella, S Cappello, A Cravotta, DF Escande, et al. Overview of quasi-single helicity experiments in reversed field pinches. *Nuclear fusion*, 43(12):1855, 2003.

[69] DF Escande, P Martin, S Ortolani, A Buffa, P Franz, L Marrelli, E Martines, G Spizzo, S Cappello, A Murari, et al. Quasi-single-helicity reversed-field-pinch plasmas. *Physical review letters*, 85(8):1662, 2000.

[70] PR Brunsell, Henric Bergsåker, Marco Cecconello, James Robert Drake, RM Gravestijn, Anders Hedqvist, and Jenny A Malmberg. Initial results from the rebuilt EXTRAP T2R RFP device. *Plasma physics and controlled fusion*, 43(11):1457, 2001.

[71] RN Dexter, DW Kerst, TW Lovell, SC Prager, and JC Sprott. The madison symmetric torus. *Fusion Science and Technology*, 19(1):131–139, 1991.

[72] S Masamune et al. Research plans for low-aspect ratio reversed field pinch. *Fusion science and technology*, 51(2T):197–199, 2007.

[73] Y Yagi, S Sekine, H Sakakita, H Koguchi, K Hayase, Y Hirano, I Hirota, S Kiyama, Y Maejima, Y Sato, et al. Design concept and confinement prediction of tpe-rx reversed-field pinch device. *Fusion engineering and design*, 45(4):409–419, 1999.

[74] Wandong Liu, Wenzhe Mao, Hong Li, Jinlin Xie, Tao Lan, Ahdi Liu, Shude Wan, Hai Wang, Jian Zheng, Xiaohui Wen, et al. Progress of the keda torus experiment project in china: design and mission. *Plasma Physics and Controlled Fusion*, 56(9):094009, 2014.

[75] PR Brunsell, Dimitry Yadikin, D Gregoratto, R Paccagnella, T Bolzonella, M Cavinato, Marco Cecconello, James Robert Drake, A Luchetta, G Manduchi, et al. Feedback stabilization of multiple resistive wall modes. *Physical review letters*, 93(22):225001, 2004.

[76] PR Brunsell, Dmitriy Yadikin, D Gregoratto, R Paccagnella, YQ Liu, T Bolzonella, M Cecconello, JR Drake, M Kuldkepp, G Manduchi, et al. Active control of multiple resistive wall modes. *Plasma physics and controlled fusion*, 47(12B):B25, 2005.

[77] Per R Brunsell, Mattias Kuldkepp, Sheena Menmuir, Marco Cecconello, Anders Hedqvist, Dimitry Yadikin, James Robert Drake, and Elisabeth Rachlew. Reversed field pinch operation with intelligent shell feedback control in extrap t2r. *Nuclear Fusion*, 46(11):904, 2006.

[78] Lorenzo Frassinetti, Per R Brunsell, James R Drake, Sheena Menmuir, and Marco Cecconello. Spontaneous quasi single helicity regimes in extrap t2r reversed-field pinch. *Physics of Plasmas (1994-present)*, 14(11):112510, 2007.

[79] S Masamune, A Sanpei, R Ikezoe, T Onchi, K Oki, T Yamashita, H Shimazu, H Himura, and R Paccagnella. Mhd properties of low-aspect ratio rfp in relax. *Journal of fusion energy*, 28(2):187, 2009.

[80] JS Sarff, AF Almagri, JK Anderson, M Borchardt, D Carmody, K Caspary, BE Chapman, DJ Den Hartog, J Duff, S Eilerman, et al. Overview of results from the mst reversed field pinch experiment. *Nuclear Fusion*, 53(10):104017, 2013.

[81] R Lorenzini, M Agostini, A Alfier, V Antoni, L Apolloni, F Auriemma, O Barana, M Baruzzo, P Bettini, D Bonfiglio, et al. Improvement of the magnetic configuration in the reversed field pinch through successive bifurcationsa). *Physics of Plasmas (1994-present)*, 16(5):056109, 2009.

[82] D Terranova, A Alfier, F Bonomo, P Franz, P Innocente, and R Pasqualotto. Enhanced confinement and quasi-single-helicity regimes induced by poloidal current drive. *Physical review letters*, 99(9):095001, 2007.

[83] Lorenzo Frassinetti, Per R Brunsell, and J Drake. Heat transport in the quasi-single-helicity islands of extrap t2r. *Physics of Plasmas*, 16(3):032503, 2009.

[84] P Franz, L Marrelli, P Piovesan, I Predebon, F Bonomo, Lorenzo Frassinetti, P Martin, G Spizzo, BE Chapman, D Craig, et al. Tomographic imaging of resistive mode dynamics in the madison symmetric torus reversed-field pinch. *Physics of plasmas*, 13(1):012510, 2006.

[85] Emilio Martines, Rita Lorenzini, Barbara Momo, David Terranova, Paolo Zanca, Alberto Alfier, Federica Bonomo, Alessandra Canton, Alessandro Fassina, Paolo Franz, et al. Equilibrium reconstruction for single helical axis reversed field pinch plasmas. *Plasma Physics and Controlled Fusion*, 53(3):035015, 2011.

[86] Paolo Zanca and David Terranova. Reconstruction of the magnetic perturbation in a toroidal reversed field pinch. *Plasma Physics and Controlled Fusion*, 46(7):1115, 2004.

[87] Gregorij V Pereverzev and PN Yushmanov. Astra. automated system for transport analysis in a tokamak. 2002.

[88] G. Urso D. F. Escande F. Auriemma, F. Sattin. Exploiting genetic algorithms in transport modeling in rfx-mod. 2015.

[89] R Lorenzini, A Alfier, F Auriemma, A Fassina, P Franz, P Innocente, D López-Bruna, E Martines, B Momo, G Pereverzev, et al. On the energy transport in internal transport barriers of rfp plasmas. *Nuclear Fusion*, 52(6):062004, 2012.

[90] R. Lorenzini, F. Auriemma, A. Fassina, E. Martines, D. Terranova, and F. Sattin. Internal transport barrier broadening through subdominant mode stabilization in reversed field pinch plasmas. *Phys. Rev. Lett.*, 116:185002, May 2016.

[91] F Auriemma, R Lorenzini, M Agostini, L Carraro, G De Masi, A Fassina, M Gobbin, E Martines, P Innocente, P Scarin, et al. Characterization of particle confinement properties in RFX-mod at a high plasma current. *Nuclear Fusion*, 55(4):043010, 2015.

[92] Radu Balescu. Transport processes in plasmas. 1988.

[93] H Biglari, PH Diamond, and PW Terry. Influence of sheared poloidal rotation on edge turbulence. *Physics of Fluids B: Plasma Physics (1989-1993)*, 2(1):1–4, 1990.

[94] R Fitzpatrick. Interaction of tearing modes with external structures in cylindrical geometry plasma. *Nuclear Fusion*, 33(7):1049, 1993.

[95] AJ Cole, CC Hegna, and JD Callen. Neoclassical toroidal viscosity and error-field penetration in tokamaks. *Physics of Plasmas (1994-present)*, 15(5):056102, 2008.

[96] Kenro Miyamoto. Plasma physics for nuclear fusion. *Cambridge, Mass., MIT Press, 1980. 625 p. Translation*, 1980.

[97] HP Furth and MN Rosenbluth. Low-frequency plasma loss mechanisms in MHD-stabilized toruses. In *Plasma Physics and Controlled Nuclear Fusion*

Research. Proceedings of the Third International Conference on Plasma Physics and Controlled Nuclear Fusion Research. Vol. I, 1969.

[98] A. A. Galeev, R. Z. Sagdeev, H. P. Furth, and M. N. Rosenbluth. Plasma diffusion in a toroidal stellarator. *Phys. Rev. Lett.*, 22:511–514, Mar 1969.

[99] KC Shaing, TH Tsai, MS Chu, and SA Sabbagh. Theory for island induced neoclassical toroidal plasma viscosity in tokamaks. *Nuclear Fusion*, 51(4):043013, 2011.

[100] Richard D Hazeltine and James D Meiss. *Plasma confinement*. Courier Corporation, 2003.

[101] Ker-Chung Shaing. Symmetry-breaking induced transport in the vicinity of a magnetic island. *Physical review letters*, 87(24):245003, 2001.

[102] Ker-Chung Shaing. Radial electric field and plasma confinement in the vicinity of a magnetic island. *Physics of Plasmas (1994-present)*, 9(8):3470–3475, 2002.

[103] F Wagner, G Becker, K Behringer, D Campbell, A Eberhagen, W Engelhardt, G Fussmann, O Gehre, J Gernhardt, G v Gierke, et al. Regime of improved confinement and high beta in neutral-beam-heated divertor discharges of the ASDEX tokamak. *Physical Review Letters*, 49(19):1408, 1982.

[104] T Estrada, T Happel, L Eliseev, E Blanco, L Cupido, JM Fontdecaba, C Hidalgo, L Krupnik, M Liniers, ME Manso, et al. Sheared flows and transition to improved confinement regime in the TJ-II stellarator. *Plasma Physics and Controlled Fusion*, 51(12):124015, 2009.

[105] DE Hastings, WA Houlberg, and Ker-Chung Shaing. The ambipolar electric field in stellarators. *Nuclear Fusion*, 25(4):445, 1985.

[106] V. Tribaldos. Monte Carlo estimation of neoclassical transport for the TJ-II stellarator. *Physics of Plasmas*, 8(4):1229–1239, 2001.

[107] HE Mynick. Transport optimization in stellarators. *Physics of Plasmas (1994-present)*, 13(5):058102, 2006.

[108] K. C. Shaing. Radial electric field and plasma confinement in the vicinity of a magnetic island. *Physics of Plasmas*, 9(8):3470–3475, 2002.

[109] K. C. Shaing, M. S. Chu, C. T. Hsu, S. A. Sabbagh, Jae Chun Seol, and Y. Sun. Theory for island induced neoclassical toroidal plasma viscosity in tokamaks. *Nuclear Fusion*, 51(12):124033, 2011.

[110] LM Kovrizhnykh. Modeling of transport processes in stellarators. *Plasma Physics Reports*, 32(12):988–995, 2006.

[111] CD Beidler. Neoclassical transport properties of HSR. *IPP-Report*, 2(331):194, 1996.

[112] CD Beidler, EE Simmet, et al. Density control problems in large stellarators with neoclassical transport. *Plasma physics and controlled fusion*, 41(9):1135, 1999.

[113] SP Hirshman, KC Shaing, WI Van Rij, CO Beasley Jr, and EC Crume Jr. Plasma transport coefficients for nonsymmetric toroidal confinement systems. *Physics of Fluids (1958-1988)*, 29(9):2951–2959, 1986.

[114] WI Van Rij and SP Hirshman. Variational bounds for transport coefficients in three-dimensional toroidal plasmas. *Physics of Fluids B: Plasma Physics (1989-1993)*, 1(3):563–569, 1989.

[115] C Gutiérrez-Tapia, JJ Martinell, D López-Bruna, AV Melnikov, L Eliseev, C Rodríguez, MA Ochando, F Castejón, J García, BP van Milligen, et al. Analysis of TJ-II experimental data with neoclassical formulations of the radial electric field. *Plasma Physics and Controlled Fusion*, 57(11):115004, 2015.

[116] G Grieger, W Lotz, P Merkel, J Nührenberg, J Sapper, E Strumberger, H Wobig, R Burhenn, V Erckmann, U Gasparino, et al. Physics optimization of stellarators. *Physics of Fluids B: Plasma Physics (1989-1993)*, 4(7):2081–2091, 1992.

[117] T Sunn Pedersen, M Otte, S Lazerson, P Helander, S Bozhenkov, C Biedermann, T Klinger, RC Wolf, H-S Bosch, The Wendelstein, et al. Confirmation of the topology of the wendelstein 7-X magnetic field to better than 1: 100,000. *Nature Communications*, 7, 2016.

[118] Shigeo Hamada. Hydromagnetic equilibria and their proper coordinates. *Nuclear Fusion*, 2(1-2):23, 1962.

[119] FL Hinton and RD Hazeltine. Theory of plasma transport in toroidal confinement systems. *Reviews of Modern Physics*, 48(2):239, 1976.

List of Figures